RADIOMETRIC IMAGE QUALITY IMPROVEMENT OF SCANSAR DATA

by

CATHERINE M. VIGNERON

B. Eng. (High Distinction), Carleton University, 1994.

A THESIS SUBMITTED IN PARTIAL FULFILLMENT OF

THE REQUIREMENTS FOR THE DEGREE OF

MASTER OF APPLIED SCIENCE

in

THE FACULTY OF GRADUATE STUDIES

DEPARTMENT OF ELECTRICAL ENGINEERING

We accept this thesis as conforming

to the required standard

THE UNIVERSITY OF BRITISH COLUMBIA

September 1996

In presenting this thesis in partial fulfilment of the requirements for an advanced degree at the University of British Columbia, I agree that the Library shall make it freely available for reference and study. I further agree that permission for extensive copying of this thesis for scholarly purposes may be granted by the head of my department or by his or her representatives. It is understood that copying or publication of this thesis for financial gain shall not be allowed without my written permission.

Department of Electrical Engineering

The University of British Columbia
Vancouver, Canada

Date SEPT 23 1996

Abstract

Remotely-sensed synthetic aperture radar (SAR) image data are of fundamental importance for the detection and monitoring of characteristics of the Earth's surface such as geophysical parameters, ocean current patterns, and agricultural crop features. In 1998, the European Space Agency will launch the ENVISAT-1 satellite which will carry an Advanced Synthetic Aperture Radar (ASAR) system capable of imaging large portions of the Earth's surface using a Scanning Synthetic Aperture Radar (ScanSAR) mode of operation. However, these images will be of little value to the Earth observation community if the quality of processed images is degraded to such an extent that significant terrain features cannot be identified.

The objective of this thesis was to investigate techniques for maximizing the radiometric image quality of remote sensing images processed using ENVISAT ScanSAR satellite data. These techniques aim to reduce the output radiometric scalloping (which appears in an image as repeated 'bands' of intensity variation) in azimuth to a level below which it is visibly undetectable (0.2 dB). To accomplish this objective, selected methods for antenna pattern correction and Doppler centroid estimation were evaluated and compared in this context. The investigation and results of the comparative analysis of the methods are summarized below.

Ideal-scenario simulations were carried out for the evaluation of the Inverse Beam Pattern Method and the Constant SNR Method for antenna pattern correction, for up to 4 looks per aperture. Both the Inverse Beam Pattern Method (IBP) and the Constant SNR Method (CSNR) for antenna pattern correction were found to be less sensitive to the effects of Doppler centroid estimation errors for an increasing number of looks per aperture. In addition, the IBP method consistently showed a maximization of the equivalent number of looks over azimuth. Conversely,

the CSNR functions derived to minimize the residual scalloping resulted in an equivalent number of looks which was not maximized over azimuth. It is possible that the amount of scalloping was increased using the CSNR method for this reason in practice, when compared to the simulation results for the 2 look implementation. As a result, there appeared to be little distinction between the practical performance of scalloping reduction of the CSNR and IBP methods for the 2 look implementation.

Selected Spectral Distribution Analysis and Phase Increment Methods for Doppler centroid estimation were implemented and evaluated using ERS-1 SAR data to simulate the ENVISAT ScanSAR case. The performance of each of the selected methods for Doppler centroid estimation was found to be sensitive to scene contrast and to the presence of land-sea boundaries in the scene. However, the Doppler centroid estimations derived using the Look Power Balancing Method were found to be more accurate than those measured using other methods over image areas of high scene contrast and for areas containing land-water boundaries. This is largely due to the fact that, contrary to the other methods tested, the accuracy of the Look Power Balancing Method does not rely on the validity of assumptions related to scene reflectivity and/or the distribution of individual scatterers. In addition, the performance of the Look Power Balancing Method for Doppler centroid estimation was found to be sensitive to antenna pattern modelling.

Table of Contents

List of Tables

List of Figures

Acknowledgment

I would like to first acknowledge my parents and family for the consistent support and encouragement that they have provided throughout my period of study.

I am very grateful to my supervisor, Dr. Ian Cumming, for providing effective supervision and academic guidance, as well as an opportunity to work in the field of synthetic aperture radar processing. I am equally indebted to my technical advisor, Dr. Martie Goulding, for the extensive technical guidance, general support, and the many useful discussions provided over the course of this research work. I would also like to acknowledge the technical assistance of Paul Lim with respect to this research.

I am grateful for the financial support provided for this research by the Natural Sciences and Engineering Council of Canada, by MacDonald Dettwiler and Associates, and by the British Columbia Advanced Systems Institute.

Finally, I would like to thank all of the members of the Radar Remote Sensing Group at UBC for providing a pleasant and effective work environment, as well as many interesting lunchtime discussions.

Chapter 1 Introduction

Remote sensing images are of little value if the techniques used for the generation of these images degrade the output image quality such that important terrain features cannot be identified.

This thesis presents an analysis of methods for the maximization of the radiometric image quality of remote sensing images processed using ENVISAT ScanSAR satellite data. These methods involve an accurate estimation of a parameter known as the Doppler centroid.

This chapter begins with an introduction to the use of synthetic aperture radar (SAR) systems for remote sensing purposes. Following this, a description of fundamental SAR concepts is provided, followed by a discussion of imaging and processing methods central to this research. The section following presents a more detailed description of the motivation for this research based on the background information contained in earlier sections. The final section defines the research objectives and presents an outline of the remaining chapters of this thesis.

1.1 Introduction to Synthetic Aperture Radar in Remote Sensing

A radar (RAdio Detection And Ranging) is an active system that transmits and receives a beam of radiation in the microwave region of the electromagnetic spectrum by providing its own illumination. The radar system operation is independent of light from the sun, and is largely unaffected by clouds, fog, and precipitation. Microwave signals are not subject to significant degradation due to atmospheric interference, and thus are well suited for transmissions over long distances. Imaging radars have been used quite successfully for a variety of remote sensing applications, including high-resolution earth surface mapping.

Since imaging radars transmit and receive a beam of electromagnetic radiation, their

application extends our ability to observe properties of the earth's surface (e.g. electrical and geometric properties) that are not available with alternate types of imaging sensors such as optical or thermal systems. Optical imaging sensors can provide images of comparable or higher resolution than those produced with a SAR system. This is because the wavelength of an optical signal is much smaller than that of a radar signal. However, a major constraint on any optical approach for imaging the Earth's surface is the existence of clouds in the Earth's atmosphere. Some areas of the globe are cloud covered most of the time, and have rarely been photographed from space.

A **synthetic aperture radar** (SAR) is an imaging radar sensor which is capable of observing and monitoring geophysical parameters of the Earth's surface, such as ocean surface patterns, sea-ice cover, and agricultural features, regardless of the time of day or weather conditions, and is thus a desirable instrument for remote sensing purposes [1]. SAR systems are also extensively used for military applications such as in the detection and tracking of moving targets. A SAR transmits radar signals from an airborne or spaceborne antenna which is oriented perpendicular to the direction of flight of the platform which travels at a constant velocity. The remotely-sensed data is collected by the antenna and stored in an unfocused (raw) format, and extensive signal processing is required to produce the output radar image.

Spaceborne radar remote sensing technology has developed rapidly since the first high-resolution spaceborne imaging SAR was flown on the SEASAT-A Earth-orbiting satellite, launched by NASA in 1978. Since then, several spaceborne SAR sensors have been used to observe and monitor the Earth's surface. This includes other orbiting radars such as those included in the European Space Agency's Earth Resources Satellite (ERS) missions 1 and 2, launched in 1991 and 1995, respectively, the Japanese Earth Resources Satellite (JERS-1),

Canada's RADARSAT (launched in 1995), and the upcoming ENVISAT-1 mission (scheduled for launch in 1998 by ESA). Shuttle-borne imaging radars have included NASA's Shuttle Imaging Radar (SIR) missions A, B, and C, launched in 1981, 1984, and 1994, respectively, and Germany's XSAR sensor, included in the SIR-C mission in 1994.

1.2 Background of SAR and Imaging Methods

1.2.1 Fundamental SAR Concepts

A SAR uses a pulsed transmitter, an antenna, a phase coherent receiver, and a signal processor to produce an image [2]. Microwaves illuminate the terrain below the platform, and the echoes scattered from the surface are collected. Subsequent signal processing performed on the echoes produces a SAR image which looks similar to a black and white photograph.

Figure 1.1 presents a simplified illustration of the geometry of a SAR system. Referring to Figure 1.1, the ground surface is specified by the along-track (azimuth) and across-track (range) coordinates. The slant range represents the absolute distance from an antenna to a target. It is a primary imaging parameter from which the ground range parameter is derived. The azimuth width of the radar beam "footprint" is inversely proportional to the antenna size, and is also a direct function of the slant range and the transmitted wavelength.

The SAR image plane is defined by the radar platform velocity, $\hat{v}$, and the radar antenna beam axis, $\hat{R}$, corresponding to azimuth and slant range dimensions, respectively. The position in slant range is determined by the time delay of the received pulse. As the target passes through the radar beam, the slant range distance, and therefore the phase of the received signal from the target, changes. This change in phase with respect to time constitutes the Doppler frequency.

Figure 1.1 Synthetic Aperture Radar Geometry

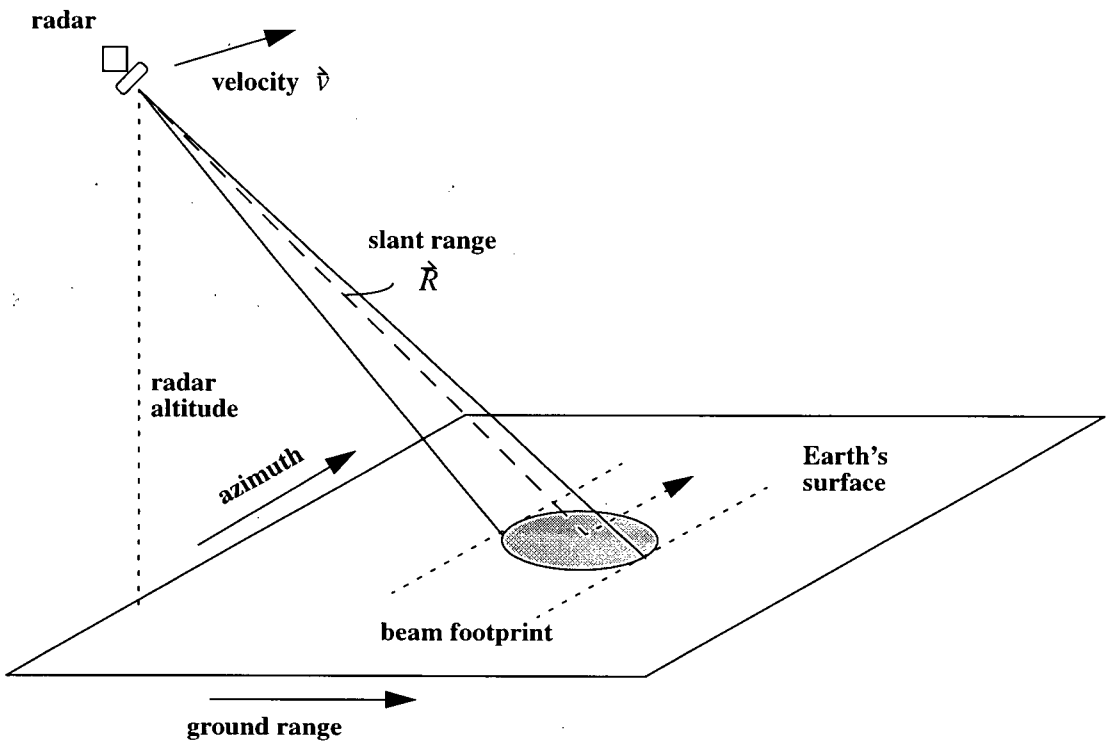

The interaction of the radiated electromagnetic wave and the surface is generally referred to as "scattering" and can occur at both surface and subsurface levels. The backscatter return signal depends predominately on (1) the electrical properties of the surface, (2) the surface roughness, and (3) the local slope. For instance, if a radar wavelength is long relative to the surface roughness, the surface will appear smooth, resulting in very little backscattered energy. However, for radar wavelengths on the scale of the root mean square (RMS) surface height deviation, the scattering characteristics will more accurately reflect the variations in surface smoothness [1].

As explained in Cumming et. al [4], a single point in signal memory contains contributions from a large collection of ground reflections, and conversely, the received signal from a single point target on the ground will be spread through a large area of signal memory. Compensa-

tion is thus required in both range and azimuth dimensions to ensure that only those returns from a specific point target on the ground are constructively added (signal energy "compression" is thus achieved). Despite the two-dimensional nature of the transmitted signal, range and azimuth digital compression operations are usually performed separately in SAR processing.

The effective duration and energy of the transmitted pulse determines the range resolution and maximum range of a radar system [5]. Reducing the duration of a radar pulse improves a system's resolution of closely spaced objects in range. However, pulses of shorter duration may not be powerful enough to accurately image the Earth from spacecraft altitudes. In order to avoid the difficult and expensive development of hardware to generate short duration pulses of high energy (for maximum distinction and amplification of imaged targets), larger pulses of high bandwidth are coded in range for transmission, then compressed at reception. Using this technique, the range resolution is inversely proportional to the bandwidth of the coded pulse. The form of range coding can be selected by the designer. In azimuth, the coding is determined by the geometry of the reflected signal's trajectory from target to antenna and has the form of a linear FM chirp. The frequency of a signal coded using a linear FM chip format is not kept constant for the duration of the pulse, but rather linearly changes from a frequency value of f_o to $f_o + \Delta f$. Range signals are commonly coded by the radar transmitter using a linear FM chirp format to optimize on applying the same type of compression equations for signal processing in both dimensions [6]. A correlation receiver employing a matched filter technique is used for the compression of the received signal.

The azimuth footprint increases as the distance between the target and the antenna increases. In **real aperture radars**, azimuth resolution is thus a function of the radar wavelength

and range of a target, and is inversely proportional to the antenna width. At high altitudes, azimuth resolution is optimized by increasing the width of the antenna. In spaceborne systems, fine resolutions would necessitate the use of very wide antennas, considering the typical range distances from the antenna to the Earth's surface.

In **synthetic aperture radars**, high azimuth resolution is achieved by using a short antenna which results in a signal of larger bandwidth. Then, a signal processing technique is used to synthesize an extremely long antenna from a coherent phase history, and thus integrate the energies of many transmitted pulses. The received signal energy is focussed by correcting for the azimuth phase shift history of each signal reflected from a specific point on the ground during the radar platform motion. This requires an accurate knowledge of the signal phase history, which is described in more detail in Section 2.1 of this thesis.

If the full length of the synthetic aperture is processed to form a single focussed image, a 'one-look' image is produced. Another option is that the total synthetic aperture length can be divided into shorter lengths corresponding to that size required for the coarser resolution. These shorter length images can be added noncoherently to reduce noise, resulting in a 'multi-look' image. Geometric correction can then be applied to the range and azimuth processed image using resampling techniques to map the radar imaging coordinate (slant range, azimuth) to ground coordinates (ground range, azimuth) to achieve square pixels in the final output image.

1.2.2 The ScanSAR Imaging Mode

A radar system can be operated in **burst-mode** such that the sensor is on for a period of time, then off, then on again, and so on, effectively imaging the region of interest in a series of 'bursts', where each burst consists of a certain number of pulses. In comparison with conventional

strip-mode imaging methods, burst-mode operation enables a reduced power consumption and data rate at the expense of the resolution and image quality achieved. An example of one of the first spaceborne burst-mode imaging radars is the Magellan system, launched by NASA in 1990. The Magellan radar imager is a planetary radar system which was designed for the surface mapping of Venus at approximately 150 m resolution [7].

Additionally, the swath width of a SAR system can be increased by steering the beam over adjacent range swaths (subswaths) to realize a **ScanSAR** configuration ([2],[8]) which is suitable for imaging applications requiring wide-range coverage of moderate to low resolution. In a ScanSAR system, the radar operates in burst-mode over a series of range subswaths. An ordered number of range subswaths (beams) constitutes a scan cycle [1], [9]. Figure 1.2 depicts the relative coverage in azimuth of a scan cycle consisting of 5 range subswaths (beams).

Figure 1.2 ScanSAR Configuration

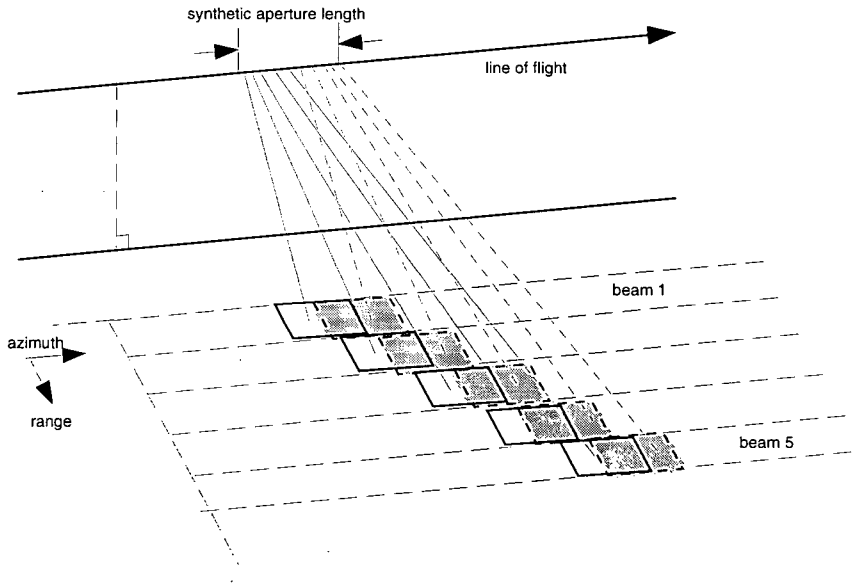

Because the potential length of a synthetic aperture radar must be shared among beam positions over azimuth, the along-track resolution and image quality is poorer since the burst size

limits the bandwidth usage. Thus, a direct trade-off exists between resolution and swath width [8].

Several spaceborne remote sensing missions (either currently in progress or under development) employ the ScanSAR mode in addition to other operational modes for radar imaging. Canada's RADARSAT satellite, which was successfully launched in 1995, is a sophisticated Earth observation system developed to monitor environmental change and support resource sustainability. The imaging platform supports various SAR operating modes, including a ScanSAR mode for the low-resolution (approximately 100 m) imaging of ground regions of width 500 km [10].

An Advanced SAR (ASAR) system will be flown on the ENVISAT-1 satellite Polar Platform [11], to be launched in 1998 by the European Space Agency. This system will be able to collect raw data covering a portion of the Earth's surface which is 400 km in width using a ScanSAR imaging mode. This *wide swath* mode on the ASAR will provide a larger spatial coverage, thus shorter revisit times, for global coverage. The trade-off for a wider swath with a fixed data rate is a reduced spatial resolution (ranging from 100 m to 1 km) due to sampling requirements.

An image of a homogeneous surface with a constant backscatter cross section will show brightness variations from one resolution element to the next. This variation is known as speckle, (speckle will be described in more detail in Section 2.2) and its effect of degrading the radiometry of an image can be reduced by employing a process known as multilooking [1]. Multilooking can be achieved by noncoherently summing processed regions which overlap in time. In ScanSAR, adjacent subswaths (beams) in azimuth time can be overlapped to achieve multilooking by effectively designing the inter-burst period to be of a much shorter duration than the synthetic

aperture integration time [12]. Figure 1.2 (above) illustrates the overlapping of scan cycles to achieve two looks per aperture, assuming that only one look is extracted per burst.

ScanSAR data is received in 'bursts', which comprise the set of echoes received from each subswath during a given scan cycle. Azimuth compression in ScanSAR systems is also carried out over bursts, which, when individually processed, constitute image sections of corresponding beams. This compression is most often done using the Spectral Analysis (SPECAN) processing algorithm, which is described in the next section.

1.2.3 The SPECAN Processing Algorithm

The Spectral Analysis (SPECAN) processing algorithm ([6], [13], [14]) is an alternative to conventional SAR precision processing algorithms that provide output images of finer resolutions, yet are computationally more expensive. In SPECAN, short-length forward Discrete Fourier Transforms (DFTs) are used in the extraction phase of processing. In contrast, a precision processing algorithm such as the Range Doppler method requires both forward and inverse DFT operations involving a relatively large number of samples, and is thus less computationally efficient. However, images produced using the SPECAN algorithm have coarser resolution than the finest that can be produced using the Range-Doppler method because short-length DFTs are used to maximize processing efficiencies.

The SPECAN algorithm employs three basic computation steps: **deramping, DFT compression**, and **data extraction. Deramping** is the operation of multiplying a linear FM signal with a complex conjugate reference signal with the same FM rate but opposite FM slope. The result is that the original FM signal is converted into a sinusoid (constant frequency) where

frequency depends upon the imaged target's position. The deramping in azimuth of a signal containing multiple targets is illustrated in Figure 1.3, where the horizontal axis of each plot represents azimuth time. The lower plot presents a frequency-time mapping of the deramp function which is used to produce the deramped signal (upper plot) when multiplied by the received signal (middle plot).

Figure 1.3 Illustration of Target Signal Deramping

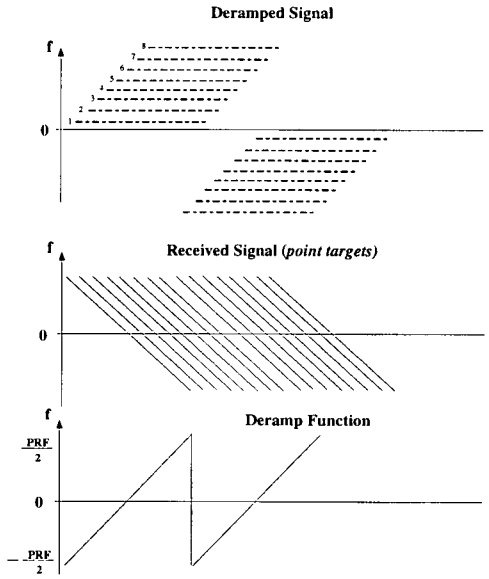

After deramping, targets will have frequencies spanning over -PRF/2 to +PRF/2, where PRF is the pulse repetition frequency. The frequency-time history of the deramped signal forms a parallelogram processing region, illustrated in Figure 1.4, which can be used to graphically illustrate the SPECAN operations. The width of the parallelogram is the length of the reference function which is a little longer than the azimuth extent of the radar antenna pattern. The frequency-time guard-band marks the unusable extent of the antenna pattern. Within the guard band and beyond, the signal energy drops off quickly and there exists a low signal to noise ratio. The total guard band length in azimuth it is typically on the order of 0.15 of the PRF.

Each deramped target in the parallelogram has a unique frequency which defines its position with respect to other targets in the same processing region. DFTs are then used to compress most of each target's energy into a single frequency bin which is proportional to its time position.

Figure 1.4 The Parallelogram Processing Region [15]

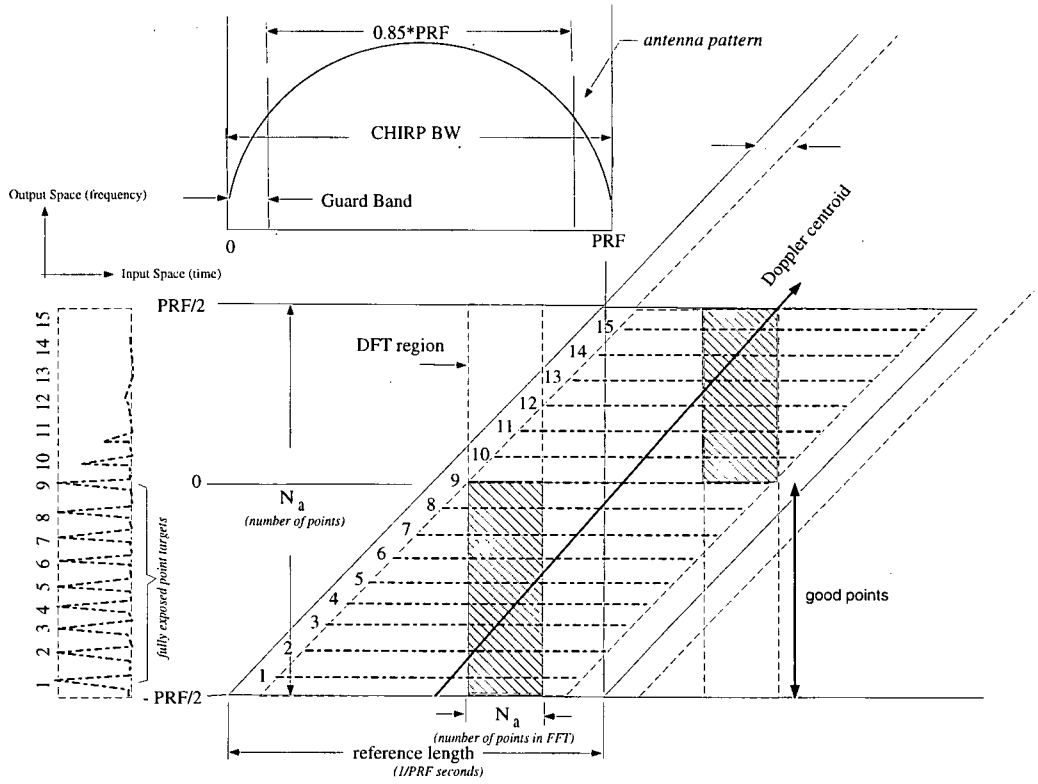

The **DFT** compression produces as many output points as there are input points. However, only a portion of these are usable since the output points contain a low ratio of signal to noise energy and those beyond the edge of the deramped signal contain no energy at all. The usable points are termed 'good points' and reside where the DFT fully covers the exposure in the unambiguous region termed the 'processing region'. For the SPECAN processing algorithm, the **Doppler centroid frequency** represents that frequency value defining the midpoint of the

frequency samples defined as 'good points'. The region consisting of the guard band and the regions beyond is termed the 'discard region'. DFT output points within the discard region are thrown away. The **data extraction** operation thus requires accurate knowledge of the Doppler centroid frequency value is thus necessary to ensure that proper extraction of the valid energy region of the processed signal.

Additionally, the location of each extraction DFT with respect to the previous DFT must be chosen carefully so as to ensure that usable energy is extracted from each target. As not all targets are fully exposed in a single DFT, multiple DFTs are required to extract all targets within a range or azimuth line, as shown in Figure 1.4. The final image is formed by the concatenation of the good output points of each successive DFT (minus any discard region) employed in the range or azimuth line [15].

1.2.4 Improving the Radiometric Image Quality of ENVISAT ScanSAR Data

The quality of images processed using SPECAN is known to suffer from radiometric scalloping across output blocks in both range and azimuth. In [16], H. Hobooti has proposed a scheme in which a range-dependent gain correction is successfully applied for the reduction of range scalloping in SAR images processed using SPECAN. Note that SPECAN is rarely used for range compression because the algorithm is less efficient in processing the entire range bandwidth when compared to a precision processor algorithm such as the Range-Doppler algorithm.

Errors in the estimation of a Doppler centroid model used for azimuth processing using SPECAN will introduce radiometric scalloping in the azimuth direction. This may dramatically degrade the quality of the output SAR image, and severely limit its usefulness for the application

at hand. In azimuth, SPECAN radiometric scalloping can be reduced if the Doppler centroid is known to a reasonable accuracy, and an appropriate model for the azimuth antenna gain pattern is known or can be accurately estimated.

The majority of research in the area of Doppler centroid estimation in SAR has focussed on the case of strip-mode (continuous) SAR data, with few widely-known contributions to the investigation of this problem for the ScanSAR case ([9],[34],[35]). Most continuous-mode data Doppler centroid estimation algorithms are not substantially affected by burst-mode data. This is because when averaging is performed over a finite number of azimuth samples, many, if not all, targets will be partially exposed. However, when many randomly located targets are in the averaged area, the parts of the targets exposed will tend to average out, so an unbiased estimate can be obtained. Yet, processing burst-mode data (or processing continuous-mode data using SPECAN) requires a more accurate Doppler centroid estimate to produce an image of acceptable radiometric image quality (one with a minimal amount of azimuth radiometric scalloping). This concept will be presented in more detail in Section 2.3.

The focus of this research is the investigation of a radiometric image quality improvement scheme based on an accurate estimation of the Doppler centroid for ENVISAT ScanSAR data which reduces the output radiometric scalloping in azimuth to a level below which it is visibly undetectable. To illustrate the determination of this tolerance level for azimuth radiometric scalloping, consider the image shown in Figure 1.5. This image demonstrates various degrees of change in the signal intensity (radiometry) over the vertical dimension. The image consists of six horizontal bands of equal size containing noise with a Gaussian distribution (scaled for an 8 bit display to values ranging from 0 to 255). The noise variance of each band is set such that the

change in intensity between each band increases from the bottom (first band) to the top (sixth band) of the image. The following five degrees of intensity change between the six bands are illustrated (from bottom to top): 0.1 dB, 0.2 dB, 0.6 dB, 1.5 dB, 2.5 dB. Note that the intensity changes between bands 5 and 6 (2.5 dB), and bands 4 and 5 (1.5 dB) are fairly visible. The intensity change between bands 3 and 4 (0.6 dB) is still detectable, but to a lesser extent. However, the intensity change between the 2nd and 3rd band (0.2 dB) is very difficult to detect, and the intensity change between the 1st and 2nd (0.1 dB) band is virtually undetectable.

Figure 1.5 Illustration of various degrees of image intensity change.

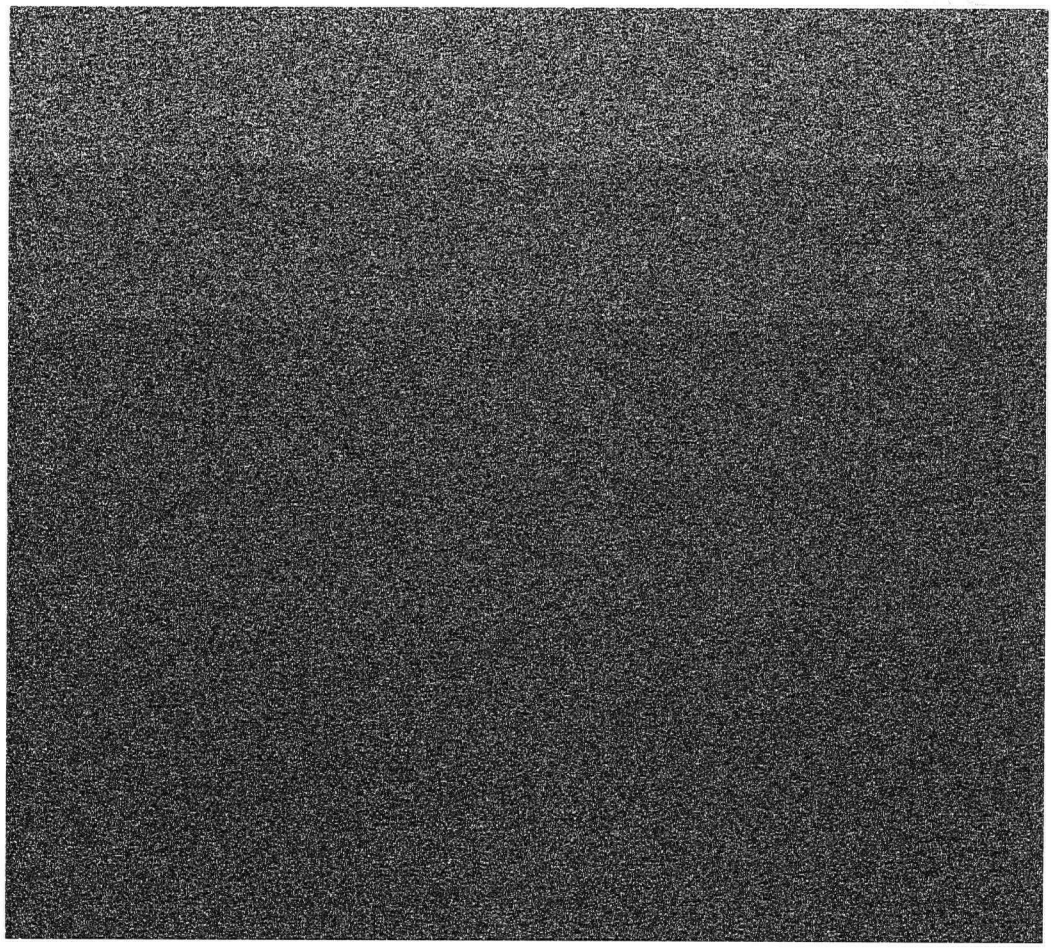

In a typical SAR image, detecting a change in radiometry is generally complicated by the

presence of additional radiometric variations due to scene features. Based on the image shown in Figure 1.5, it is assumed that a radiometric change below 0.2 dB is not visibly detectable in a typical SAR image. This thesis thus presents the work accomplished in investigating strategies to reduce the azimuth radiometric scalloping in an output image to below 0.2 dB.

1.3 Thesis Objectives and Outline

This work was carried out under the MacDonald Dettwiler and Associates (MDA)/ Natural Sciences and Engineering Research Council (NSERC) Industrial Research Chair for Radar Remote Sensing.

The purpose of this research work was to investigate techniques for maximizing the radiometric image quality of azimuth processed ENVISAT ASAR ScanSAR data. Although several authors have investigated Doppler centroid estimation techniques for the case of continuous-mode data processing, there have been relatively few contributions to the problem of Doppler centroid estimation for ScanSAR data. In addition, this thesis presents a novel evaluation of the performance of two selected antenna pattern correction methods for ScanSAR data in the presence of Doppler centroid estimation errors. The set of objectives listed below further define the purpose of this research work.

(i) To quantify the performance results of selected methods for antenna pattern correction in ENVISAT ScanSAR data processing with up to 4 bursts per aperture.

(ii) To investigate the sensitivity of residual scalloping to Doppler centroid estimation error for the selected methods for antenna pattern correction with up to 4 bursts per aperture. Specifically, to determine the minimum Doppler centroid estimation error which results in a residual scalloping error of 0.2 dB for the ENVISAT ScanSAR system.

(iii) To investigate, evaluate, and compare selected methods for Doppler centroid estimation in ENVISAT ScanSAR data in terms of the Doppler centroid estimation error and the resulting radiometric quality of images processed using the set of estimates generated using each estimation method.

The remainder of this thesis describes the approach, rationale, and results of the research work which was carried out for the achievement of these objectives.

Chapter 2 begins with a definition of the Doppler centroid, and describes several factors affecting the accuracy of the estimation of the Doppler centroid value. This is followed by an analysis of the effects of Doppler centroid estimation error on radiometric image quality of ScanSAR data. The performance results of selected methods for antenna pattern correction in ENVISAT ScanSAR data processing (with up to 4 bursts per aperture) are quantified. Results describing the sensitivity of residual scalloping to Doppler centroid estimation error for the selected methods for antenna pattern correction are also presented.

Chapter 3 presents an outline of the selected methods for the Doppler centroid estimation problem in ScanSAR data. The implementation of each method is then described in detail. In addition, certain assumptions that are implicit for the ideal performance of each estimator are presented. A discussion of the sensitivity of each estimator to the validity of the assumed conditions for optimal performance is included, and the relative performance of the estimators is

predicted for certain scenarios as a result.

Chapter 4 presents the results of two measures used to quantify the relative estimation performance (in terms of radiometric image quality) of the selected methods for Doppler centroid estimation in ENVISAT ScanSAR data. The results of simulations are then presented with reference to the predicted performance of the estimators based on the validity of certain assumptions developed in Chapter 3. This is followed by a brief discussion of estimator computational efficiency. The results are then summarized in the final section of the chapter.

Finally, chapter 5 presents a summary of the research finding and significance of this investigation, and suggests possible areas of future work.

Chapter 2 The Doppler Centroid Estimation Problem

This chapter begins with a definition of the Doppler centroid, and then presents factors affecting the accuracy of the estimation of the Doppler centroid value using clutterlock techniques. This is followed by an analysis of the effects of Doppler centroid estimation error on radiometric image quality of ScanSAR data, including the presentation of results drawn from azimuth radiometric correction simulations.

2.1 Definition of the Doppler Centroid

In SAR, the azimuth resolution is achieved by taking advantage of the fact that as a moving coherent radar illuminates a stationary ground target, the phase history of the returns are preserved by the coherent SAR. Azimuth compression thus requires an accurate knowledge of the phase shift history of the ground targets being imaged. The required phase compensation can be derived from the theoretical signal phase shift history such that returns specific to each ground target collected during the exposure time are constructively added [17]. In [18], [19], an expression for Doppler frequency is developed as the time derivative of the phase differences between the transmitted and received waveforms due to the two-way travel over range. This is summarized below.

Let $\vec{R_T}(t)$ and $\vec{R_S}(t)$ denote the positions as a function of time of a ground target and an imaging spacecraft. Then, the motion history of the target can be defined relative to the spacecraft position in the following manner,

$$\vec{R_r}(t) = \vec{R_T}(t) - \vec{R_S}(t) \qquad \text{(EQ 1)}$$

$$\vec{V}_r(t) = \vec{V}_T(t) - \vec{V}_S(t) \quad \text{(EQ 2)}$$

$$\vec{A}_r(t) = \vec{A}_T(t) - \vec{A}_S(t) \quad \text{(EQ 3)}$$

where the vectors $\vec{V}_i(t)$ and $\vec{A}_i(t)$ represent velocity and acceleration functions (with i = r, T, and S), respectively. An expression for $\vec{R}_r(t)$ can be obtained using a Taylor series expansion near time t_o, where t_o represents the time at which the target is in the antenna boresight, and assuming that velocity and acceleration terms are constant during this time interval. Then,

$$\vec{R}_r(t) = \vec{R}_r(t_o) + (t-t_o)\vec{V}_r(t_o) + \frac{1}{2}(t-t_o)^2\vec{A}_r(t_o) . \quad \text{(EQ 4)}$$

The phase history of the target can be defined as a function of range history as follows,

$$\Phi(t) = \frac{4\pi}{\lambda}\left|\vec{R}_r(t)\right| \quad \text{(EQ 5)}$$

where λ is the wavelength of the transmitted radar carrier. The instantaneous Doppler frequency shift is defined as the rate of change of phase with time, or

$$f_{D_i}(t) = \frac{1}{2\pi}\frac{d}{dt}\Phi(t) = f_D(t_o) + (t-t_o)K_a(t_o) \quad \text{(EQ 6)}$$

where

$$f_D(t_o) = -\frac{2\vec{R}_r(t_o)\cdot\vec{V}_r(t_o)}{\lambda\left|\vec{R}_r(t_o)\right|} \quad \text{(EQ 7)}$$

$$K_a(t_o) = -\frac{2\left[\vec{V}_r(t_o)\cdot\vec{V}_r(t_o) + \vec{R}_r(t_o)\cdot\vec{A}_r(t_o)\right]}{\lambda\left|\vec{R}_r(t_o)\right|} \quad \text{(EQ 8)}$$

are defined as the Doppler centroid and the Doppler frequency rate, respectively. Thus, the Doppler centroid represents the azimuth frequency corresponding to the center of the antenna beam profile.

The Doppler frequency quantifies the relative velocity of a target with respect to the antenna. This concept can be illustrated using Figure 2.1, and by defining the Doppler shift as in equation 9, where $v\sin\theta$ is the radial component of the target towards the antenna with wavelength λ.

$$f_D = \frac{2}{\lambda} v \sin\theta \qquad \text{(EQ 9)}$$

Figure 2.1 Doppler Shift of a Point Target with respect to an Antenna

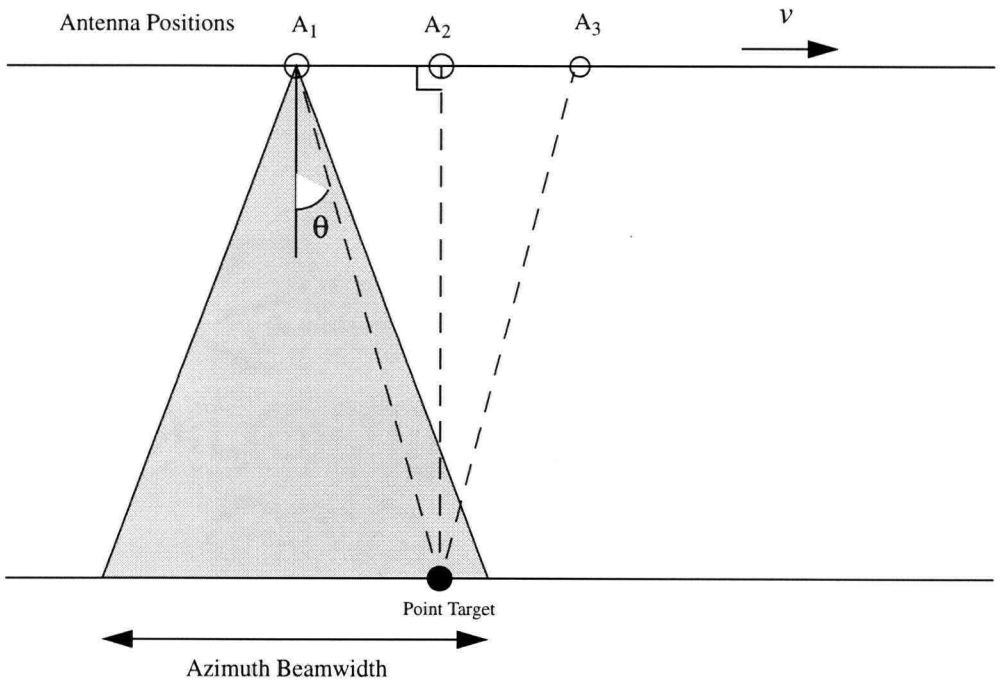

As the antenna position travels in time, the Doppler frequency decreases from a positive quantity

at A1 to zero at A2. The Doppler shift becomes increasingly negative as the antenna position moves right of position A2 [1].

2.1.1 Factors Contributing to Doppler Centroid Shift

A point target on the surface of the earth will travel about the earth's axis of rotation at a speed $V_R = R_R \Omega_R \cos e$, where R_R and Ω_R are the radius and rate of rotation of the earth, respectively, and e is the point target latitude angle, as measured from the equator. The Doppler shift resulting from earth rotation effects is

$$f_R = \frac{2V_R}{\lambda} \sin\theta . \qquad \text{(EQ 10)}$$

This is illustrated in Figure 2.2. The component of Doppler shift is most significant for point targets situated at the Equator.

Figure 2.2 Illustration of earth rotation shift component geometry

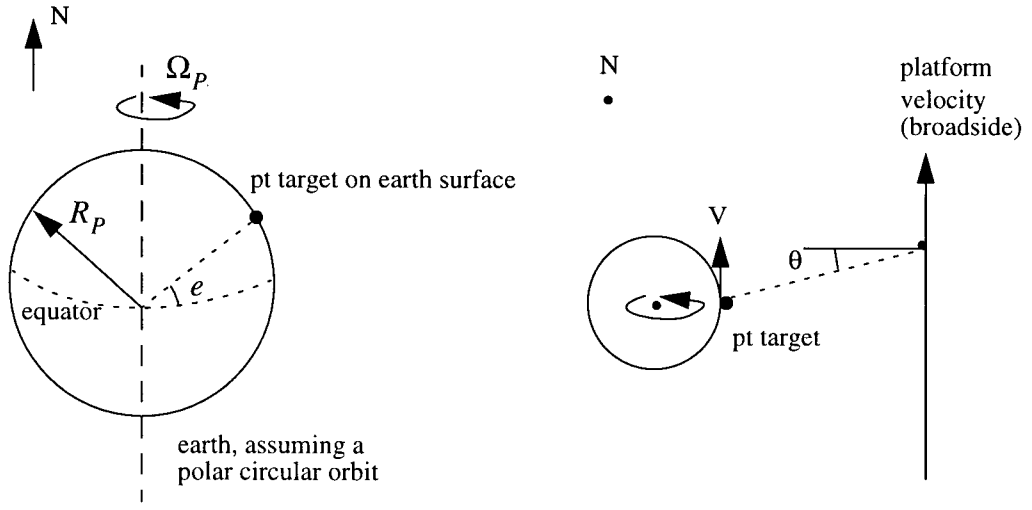

If the spacecraft travels in an elliptical orbit, an additional Doppler shift component, f_E, is introduced. This is given by

$$f_E = \frac{2v_r}{\lambda}\cos\beta. \qquad \text{(EQ 11)}$$

where v_r is the radial velocity of the spacecraft, and β is the angle formed between the major axis and a vector defining the position of the spacecraft (on the elliptical orbit) with respect to the earth (on the major axis, situated at one focal point) [1].

Additional Doppler shift components arise as a result of spacecraft flight positional errors. Whenever the antenna beam pointing angle varies due to platform attitude errors, the Doppler centroid changes accordingly during the platform motion. Roll, yaw, and pitch errors correspond to a spacecraft's rotation about its along-track, vertical, and across-track axes, respectively. In [20], Wong et al presents an expression for the Doppler centroid as a function of orbit parameters. This is given by

$$f_c = \frac{K_a}{B}\left[h\frac{dH}{d\eta} - hV_1\theta_p - gV_1(\theta_y - \psi)\right] \qquad \text{(EQ 12)}$$

where

- η = azimuth time of closest approach — V_1 = satellite speed
- h = local satellite altitude — H = local orbit radius
- θ_p = pitch — θ_y = yaw
- B = square of ($\vec{V}_{target}$ - $\vec{V}_{ant}$) — g = ground range
- ψ = satellite heading deviation from track caused by earth rotation
- K_a = azimuth FM rate

Using typical ERS-1 parameters and assuming no yaw-steering and zero pitch and yaw, Wong

finds that the maximum change in the Doppler centroid frequency within a 100 km scene to be 96 Hz (assuming a K_a of 2000 Hz/s). With an error budget of 50 Hz, he recommends that the Doppler centroid estimate be updated once over a 100 km swath. As the orbit parameters of ENVISAT are similar to those of ERS-1, he predicts that this variation is representative of the ENVISAT case. Thus, the Doppler centroid estimate should be updated 4 times over a range swath of 400 km (as in the ENVISAT case). Yet, for the case of a yaw-steered platform such as ENVISAT, the antenna motion is guided to compensate for earth rotation effects, resulting in a reduced maximum Doppler centroid drift within the 400 km scene. The impact of each of these factors in terms of Doppler shift is further described in [1], [18], [9].

In the above analysis, the radar beam of the SAR was assumed to be aimed perpendicular to the line of flight of the spacecraft (at broadside). For some applications, the radar beam is aimed off-broadside in the azimuth direction by an amount known as the **squint angle**. Positioning the SAR antenna beam in this manner is known as **squint mode SAR imaging**, and is illustrated in Figure 2.3 below.

Figure 2.3 Squint-Mode SAR Imaging

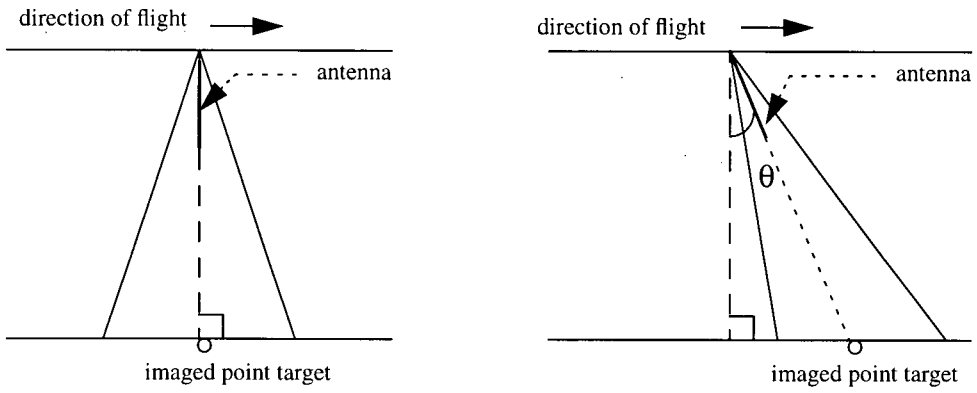

Increasing the squint angle results in the shifting of the SAR signal energy in azimuth frequency. This Doppler shift is given by

$$f_S = \frac{2v}{\lambda}\sin\theta\sin\theta_S \qquad \text{(EQ 13)}$$

where θ_S is the squint angle, as shown in Figure 2.3, and θ was defined in Figure 2.1 [7].

In practice, estimates of the satellite position and antenna angle are not accurate enough to allow sufficiently accurate calculation of the Doppler centroid needed for radiometric image compensation and azimuth compression (for quicklook methods). Thus, the Doppler centroid can be estimated by automatic, or "clutterlock" [18] techniques applied to the SAR data. Selected clutterlock methods (methods which estimate the Doppler centroid from the received SAR data) will be presented in Chapter 3.

2.2 Factors Affecting Doppler Centroid Estimation Accuracy

2.2.1 Variation of Doppler centroid with range

Recalling equation 7 (section 2.1), the Doppler centroid is a function of range. If the signal data was collected using a yaw-steered antenna (as in ERS-1 and ENVISAT), the Doppler centroid variation is typically reduced to under half of one PRF cycle per 100 km. However, if the imaging antenna is not yaw-steered (for example, RADARSAT), the Doppler centroid may vary over a significant extent in frequency, especially in the case of a wide coverage mode, such as ScanSAR. The estimator generally requires a model for this variation over range (whether the satellite is yaw-steered or not), which can be calculated based on individual Doppler centroid estimates measured at discrete positions in range. Since clutterlock techniques for the Doppler centroid estimation of each discrete position in range generally involve the averaging of azimuth samples over some extent in range to improve the signal to noise ratio of the estimation area (this is further described in the following sections), one must use caution so as to limit the extent in range over which the spectra are averaged so as to not include portions of data in the averaging process that show a significant Doppler centroid drift over the range area in question. For reference, Curlander derives a detailed model of Doppler centroid variation with range [7].

2.2.2 Noise

The received SAR signal (the complex scene reflectivity function) of an imaged area of uniform backscatter is often modelled as a complex, Gaussian, zero-mean, stationary processes [7]. This is because the complex number representing the reflection from each resolution cell on the ground is the coherent sum of many reflections (randomly distributed) from each point in the resolution cell. The Central Limit Theorem states that the sum of j statistically independent

random variables approaches a Gaussian distribution as j becomes large [21]. Using the Central Limit Theorem, the mean of the complex reflectivity function approaches zero with the coherent addition of many random scatterers. The accuracy of the automatic Doppler centroid estimation process increases with increasing SNR levels in the signal data. The noise term is mainly comprised of thermal noise, speckle noise (an exponentially distributed process), and azimuth ambiguity noise. Thermal noise (resulting from the SAR signal receiver) can be modeled as additive white Gaussian noise. The latter two noise terms are discussed below.

An image of a homogeneous surface with a constant backscatter cross-section will show brightness variation from one resolution element to the next. This variation is known as **speckle** and its effect is to degrade the radiometry of the image.

Speckle may be modeled by considering that several scattering centers are present in each resolution cell of the radar image. The backscatter cross-section of a resolution cell is then the coherent sum of the individual fields from each scattering center. If the scatterers are randomly positioned within the cell and if the cell dimension is much greater than that of the wavelength then this sum will be characterized by a zero mean, complex Gaussian random number with variance proportional to the average radar cross-section of the surface. This variance results in creating localized destructive and constructive interference which appears in the image as bright and dark speckles.

To reduce the speckle noise for Doppler centroid estimation, the spectrum of data is summed across many samples in range to reduce the random variable effect of ground reflectivity. In this way, the mean of the backscatter cross-section is unchanged while the variance is reduced. This reduces the speckle effect, and the azimuth antenna gain pattern which shapes the Doppler

spectrum emerges as the predominant spectral pattern as more and more azimuth lines are summed across range [1], [22], [5]. This is because the received azimuth signal as a function of time is ideally the convolution of the transmitted azimuth signal and the ground reflectivity. In the frequency domain, this spectrum of the received signal is thus the spectrum of the ground reflectivity multiplied by the transmitted azimuth signal spectrum (which has a magnitude shape similar to the azimuth antenna beam pattern). Thus, by summing many azimuth lines over range, assuming a ground reflectivity of uniform spatial variance, the spectrum of the transmitted signal emerges as the predominant spectral pattern [16].

The gain of an antenna is proportional to its area. The shape of the antenna beam, specifically its sidelobe characteristics, affects the performance of a radar system. **Azimuth ambiguities** contribute to limiting the required area of the antenna [3].

Azimuth ambiguity noise arises from finite sampling of the azimuth frequency at the PRF. Note that the SAR Doppler spectrum is not strictly bandlimited due to the sidelobes of the antenna pattern. Since the spectrum repeats at PRF intervals, the desired signal band may be significantly corrupted by adjacent spectral signal components which alias into the main part of the spectrum (refer to Figure 2.4 below) [7].

Figure 2.4 Azimuth Ambiguity Illustration [7]

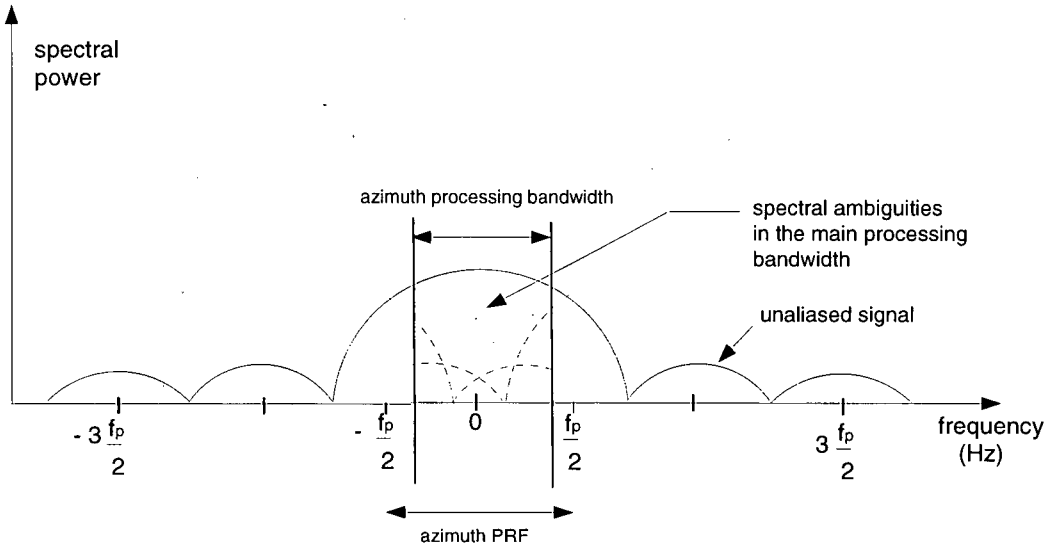

To suppress the azimuth ambiguity noise to signal ratio, the PRF may be increased, but this may introduce significant range ambiguities (radar returns from two successive pulses overlapping at the receiver in time). Alternately, the azimuth ambiguity to signal ratio may be reduced by selecting a processing bandwidth narrower than the PRF, or selecting spectral FFT weighting to adequately lower the antenna gain sidelobes.

2.2.3 Scene content

Section 2.2.2 introduced the concept of summing the raw azimuth spectrum over range to reduce the random variable effect of ground reflectivity. In summary, regions of strong radar backscatter (bright point targets) present in the azimuth spectrum at some range may not be present at a different range, and will therefore be suppressed in the smoothed spectrum, leaving only the antenna gain pattern. However, the utility of this technique is greatly reduced for scenes containing bright targets which occur over more than a few range bins, (for example, a land-water boundary) presenting a bias to the resulting summed spectrum [18]. One way to alleviate this

problem is to include several spectra in the smoothing process which are well separated in range.

For scenes containing areas of high contrast[1], performing azimuth compression on the signal data region of interest before the estimation process may yield a more accurate result. The spectral energy of an imaged target before azimuth compression is smeared over several bins in azimuth such that it is extended over time as it is seen by different sections of the receiver antenna. After azimuth compression, the target energy is effectively compressed to occupy only a few (if not only one) azimuth bins. In this sense, the azimuth processing bandwidth of a section of raw data may only capture a section of an extended target (a surface much larger than a resolution cell with high surface roughness compared to the wavelength [24]) which would wrongly contribute to the overall spectral estimate. Regions of high contrast (containing many bright targets) are more likely to contain improperly exposed extended targets which may corrupt the range-averaged spectrum, especially if these are not fully suppressed after smoothing in range. It is important to note that azimuth compression, while being a favorable method for the suppression of the effects of improperly exposed extended targets, may still introduce residual distortion caused by aliased frequency components (azimuth ambiguities effects) which would reduce the signal to noise ratio and hence, final estimation accuracy [7].

2.2.4 Number of Samples in Estimate

It is important to include a significant number of samples in the Doppler centroid estimate to maximize the SNR over the averaged spectrum. The number of samples included in the estimate is a crucial factor in the determination of the performance of all estimation methods.

---

[1] Contrast can be defined as the degree of difference of apparent brightness over an image area.

2.3 Effects of Doppler Centroid Estimation Error on Radiometric Image Quality for ScanSAR data

Before azimuth compression, the data for each subswath must be adjusted by the proper azimuth gain correction function. This is due to the fact that the return energy from a single scatterer is modulated in azimuth according to its antenna gain pattern, an effect known as **scalloping** [12]. The amount of scalloping corresponds to the energy difference from the beginning to the end of the processing bandwidth, as shown in Figure 2.5, and is generally measured in decibels (dB).

Scalloping is most noticeable in the areas of a scene that do not demonstrate a significant amount of natural radiometric variation (i.e. smooth or featureless scenes). A featureless scene processed without scalloping correction would exhibit periodically repeated areas of lighter and darker intensity in azimuth, or 'banding', as different point targets are illuminated by different positions of the beam, yielding different integrated powers. This variation can be reduced by averaging looks from different bursts.

Figure 2.5 Return Energy from a Single Scatterer (3 bursts shown).

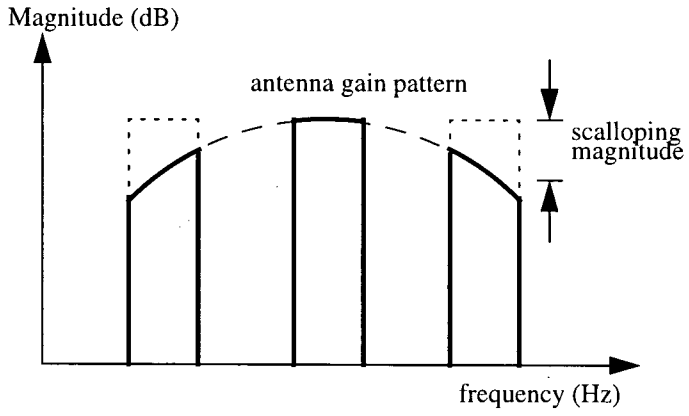

One method to correct for azimuth scalloping across individual beams involves applying

weighting functions which are inversely related to the predicted antenna gain pattern function[2], thus resulting in a constant magnitude in azimuth across the corrected beam. However, an inaccurate estimation of this Doppler shift of the raw data spectrum leads to a misapplication of each of the antenna beam correction pattern functions to its corresponding burst image return signal. As a result, the output signal level is rendered non-constant and thus exhibits **residual scalloping**. The figure below illustrates this concept. Additionally, Appendix E contains two processed, single look images of the same low-contrast region of an ERS-1 scene (Chilcotin). One is processed using an accurate estimate of the Doppler centroid, thus yielding no visible residual scalloping, and one is processed (for demonstration purposes) to yield on average 2.5 dB of residual azimuth scalloping. As described, the scalloping appears as slowly varying dark bands over the image.

Figure 2.6 Effects of Doppler Centroid Estimation Error.

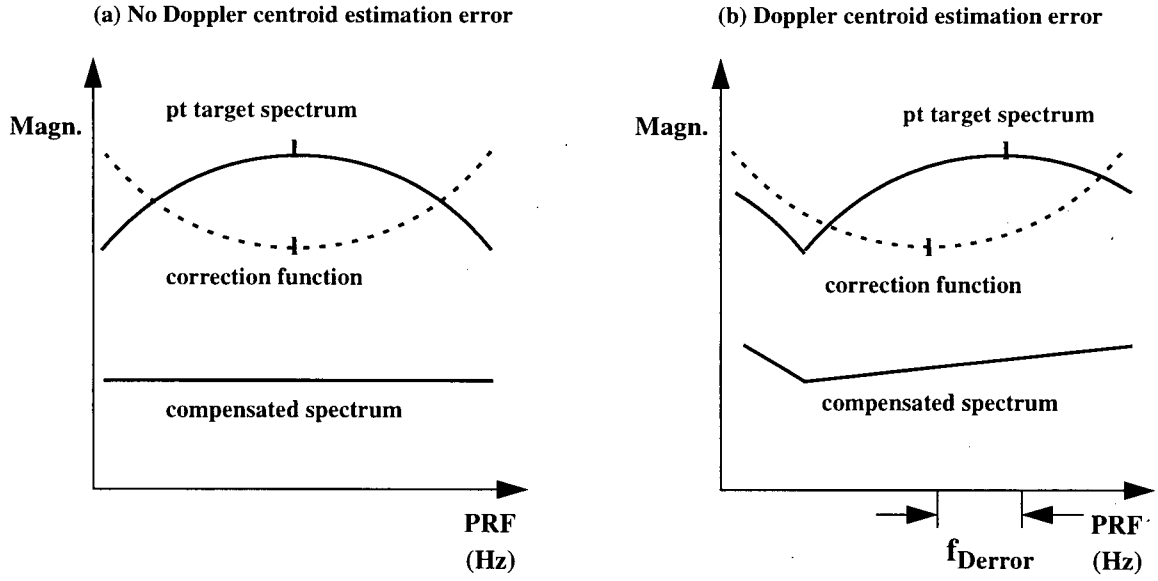

[2] This method for radiometric correction, known as the Inverse Beam Pattern Method, is described in detail in the next section.

2.3.1 Selected Methods for Azimuth Radiometric Correction

(i) Inverse Beam Pattern Method

One method to correct for azimuth scalloping across individual beams involves applying weighting functions which are inversely proportional to the antenna gain pattern function. This technique shall be referred to as the Inverse Beam Pattern Method for descalloping, and is described in more detail below [25].

Let there be L overlapping burst images per aperture. Assume that $A_i(x)$ is the azimuth dependent signal power determined by the azimuth beam pattern of a single burst image, where i to L and x is the frequency variable in Hz. Then, $W_i(x)$ is the look weighting filter to be applied to $A_i(x)$ before look summation.

Each of the L burst images is separated by a burst period, x_P, in the following manner,

$$A_i(x) = A\left(x - \left(i - \frac{L+1}{2}\right)x_P\right). \qquad \text{(EQ 14)}$$

Then, the inverse beam pattern weighting functions can be defined as shown below,

$$W_i(x) = \frac{S(x)}{A_i(x)} \qquad \text{(EQ 15)}$$

where $S(x)$ represents the signal energy of the image. Figure 2.7 illustrates an example case of $A_i(x)$ and $W_i(x)$ for $L = 2$, as defined below, for a constant signal energy level, $S(x) = S$.

Figure 2.7 Power of Burst Image Envelopes and Look Weighting Functions, L=2.

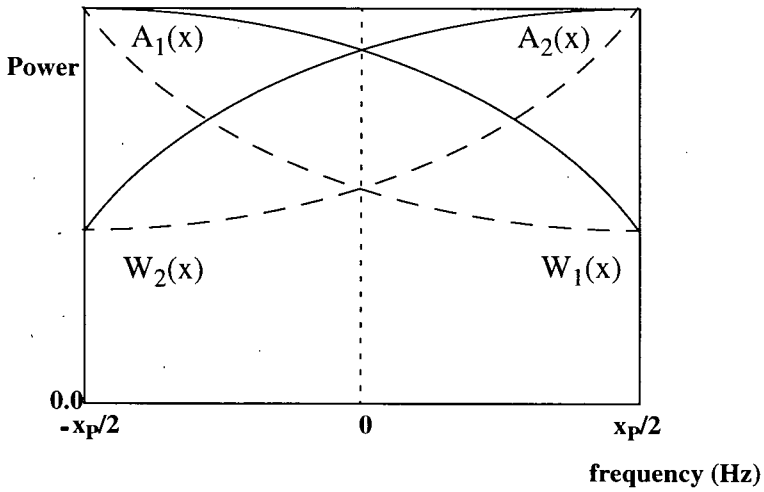

(ii) Constant SNR Method

In [12], Bamler has developed a set of antenna pattern correction functions for burst-mode and ScanSAR processing. The functions are derived to satisfy the following three criteria items in the multilook case:

1. the image signal energy becomes constant over azimuth
2. the noise energy becomes constant over azimuth, and
3. the equivalent number of looks is maximized over azimuth.

The first and second criteria result in a constant signal to noise ratio (S/N) over azimuth, which renders radiometric evaluation of the data less complicated in the presence of noise.

By varying the signal image level, the optimal set of filters can be selected based on certain performance criteria, namely the sensitivity of residual scalloping to Doppler centroid errors, and/or the radiometric resolution. These terms are further discussed in Section 2.3.2.

The following few paragraphs highlight selected points of the look filter set derivation, which is found in complete form in [12].

For this method, each of the L burst images, $A_i(x)$, and weighting filters, $W_i(x)$, is separated by a burst period, x_P, in the following manner,

$$A_i(x) = A\left(x - \left(i - \frac{L+1}{2}\right)x_P\right) \quad \text{(EQ 16)}$$

$$W_i(x) = W\left(x - \left(i - \frac{L+1}{2}\right)x_P\right) \quad \text{(EQ 17)}$$

Figure 2.8 illustrates an example case of $A_i(x)$ and $W_i(x)$ for $L = 3$, and $x_P = 400$ Hz.

Figure 2.8 Power of Burst Images and Look Weighting Functions, L=3.

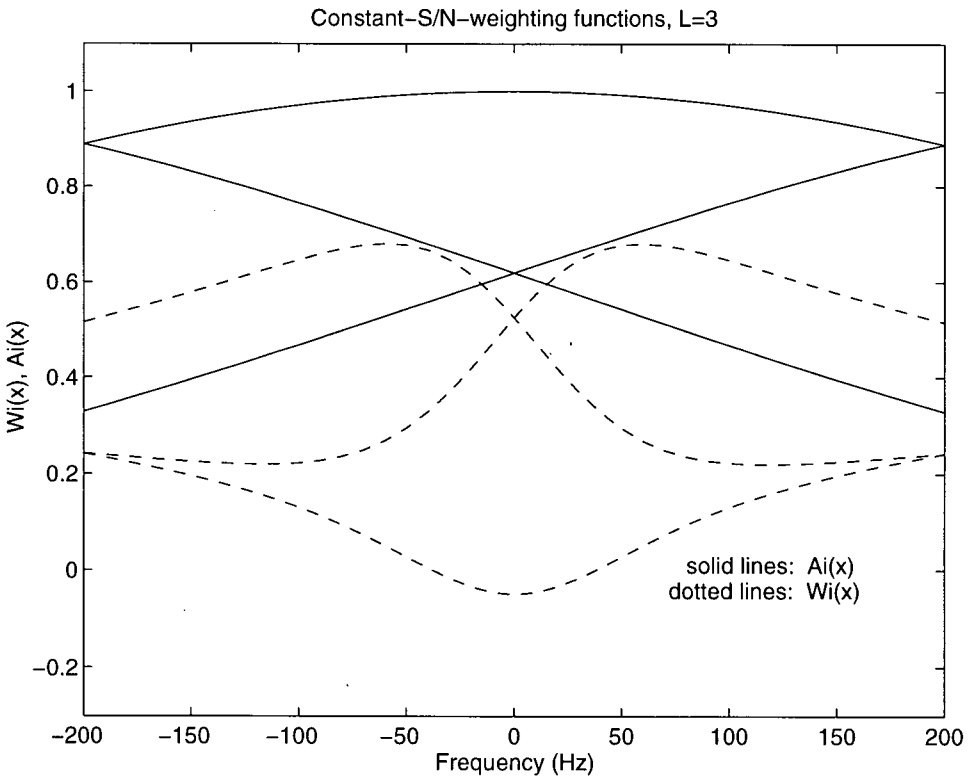

The three criteria for the derivation of the set of $W_i(x)$ from above translate into the following constraints,

$$\sum_{i=1}^{L} A_i(x)\, W_i(x) = S = \text{constant signal level} \quad \text{(EQ 18)}$$

$$\sum_{i=1}^{L} W_i(x) = 1 \quad \text{(EQ 19)}$$

$$L_{equ}(x) = \frac{S^2}{\sum_{i=1}^{L} A_i(x)^2 W_i(x)^2} \rightarrow \max \quad \text{(EQ 20)}$$

which are satisfied for the case of $L = 2$ and $L = 3$ as shown below for $i = 1$[3]. Note that all other W_i functions, $i = 1$ to L, can be obtained by a cyclic shift of the indices, and that x-dependence has been suppressed in the notation below. For $L = 2$,

$$W_1 = \frac{S - A_2}{A_1 - A_2} \quad \text{(EQ 21)}$$

where $S = A_1(x_0) = A_2(x_0)$ for $x_0 = 0$ Hz and $W_1(x_0) = W_2(x_0) = 0.5$[4]. For $L = 3$,

$$W_1 = \frac{(A_2 - A_1)(A_2 - S)A_3^2 + (A_3 - A_1)(A_3 - S)A_2^2}{(A_1 - A_2)^2 A_3^2 + (A_2 - A_3)^2 A_1^2 + (A_3 - A_1)^2 A_2^2} \quad \text{(EQ 22)}$$

2.3.2 Azimuth Radiometric Correction Method Simulations and Performance Results

- **Residual Scalloping**

A Doppler centroid estimation error will lead to residual scalloping caused by a misapplication of the look weighting filter for gain compensation, as presented earlier in Section 2.3. This

[3] Please refer to [12] for the case of L=4.

[4] Please see Appendix A for this derivation.

can be quantified in the following manner, referring to EQ 18 with a Doppler centroid error of f_{Derr},

$$S_{err}(x) = \sum_{i=1}^{L} A_i(x - f_{Derr})\, W_i(x) \qquad \text{(EQ 23)}$$

The resulting radiometric error, $R(x)$, is defined as

$$R(x) = 10\log\left(\frac{S_{err}(x)}{S}\right) \quad [dB] \qquad \text{(EQ 24)}$$

where S is the signal level with no estimation error. The residual scalloping, $RS(x)$, simply measures the greatest difference in radiometric error, for a given signal level.

$$RS(x) = max(R(x)) - min(R(x)) \quad [dB] \qquad \text{(EQ 25)}$$

- **Radiometric Resolution**

The equivalent number of looks measures the amount of speckle reduction obtained by the weighted multilook process, and is calculated as follows, for a given signal level,

$$L_{equ}(x) = \frac{\left[\sum_{i=1}^{L} A_i(x)\, W_i(x)\right]^2}{\sum_{i=1}^{L} A_i^2(x)\, W_i^2(x)} \qquad \text{(EQ 26)}$$

The effective number of looks, N_{eff}, is calculated as the equivalent number of looks in the presence of noise, N_o, and is defined below.

$$N_{eff}(x) = \frac{S^2}{\sum_{i=1}^{L} \left[A_i^2(x) + N_o\right] W_i^2(x)} \quad \text{(EQ 27)}$$

Using the definition above, the radiometric resolution, $RR(S)$, can be defined by considering the worst case (maximum) value over a period, for a given signal level.

$$RR(S) = max\left(10\log\left(1 + \frac{1}{\sqrt{N_{eff}}}\right)\right) \quad [dB] \quad \text{(EQ 28)}$$

- **Discussion of Simulation Method and Performance Results**

Simulations were carried out using both methods outlined in Chapter 3 for the derivation of antenna pattern correction filters for the 2-look, 3-look, and 4-look ScanSAR cases. A nominal burst period, x_p, of 1200 Hz, was used so that the 3-look processing bandwidth was 1200/3=400 Hz, in accordance with the simulation done in [12]. The antenna beam power pattern was defined as

$$A(x) = \left(\text{sinc}\left(\frac{x}{1500}\right)\right)^4 \quad \text{(EQ 29)}$$

and various signal levels (S = 0.4 to 0.9 in steps of 0.05) were tested.

For the 2-look case, only one signal level was considered, namely $S = A(x_o) = 0.889$, where $x_o = 0$ Hz (see Appendix A for the derivation of these values).

For each case, Appendices B and C present sets of 6 plots outlining the simulation and performance results of the Inverse Beam Pattern and Constant SNR methods, respectively. In each set, the first and second plots illustrate the power of each burst image envelope and its

corresponding look weighting function, over the defined period. Both the equivalent number of looks and the radiometric resolution are graphed in plots 3 and 4. Finally, plots 5 and 6 illustrate the noise signal level over azimuth and residual scalloping which results from a Doppler centroid error generating a minimum of 0.2 dB of residual scalloping, respectively.

The sensitivity of residual scalloping with Doppler centroid error was measured in each case for Doppler centroid errors of 5 to 105 Hz. These results appear in Appendix D.

Table 1 summarizes the performance results of each simulation for both the inverse beam pattern and Constant SNR methods (indicted by (inv) and (CR), respectively). The Doppler centroid error resulting in a minimum residual scalloping of 0.2 dB for a given signal level S_D is denoted by f_D. S_R indicates the signal level which yields a minimum radiometric resolution in each case. Finally, the last column lists the greatest and least equivalent number of looks, L_{equ}, measured over the span of azimuth frequencies simulated.

Table 2.1 Performance Results of Azimuth Radiometric Correction Method Simulations

case	f_D (Hz)	S_D	S_R	L_{equ}
L=1 (inv)	20	all S	all S	1
L=2 (inv)	19	all S	all S	2
L=3 (inv)	18	all S	all S	3
L=4 (inv)	16	all S	all S	4
L=2 (CR)	47	0.889	0.889	2, 1.5
L=3 (CR)	90	0.8	0.7	3, 1.5
L=4 (CR)	97	0.6	0.55 or 0.6[a]	4, 2.7

a. for worst case noise variance, N_0=0.1

The simulation results presented in the graph of Appendix D demonstrate that the sensitivity of residual scalloping to Doppler centroid estimation error is reduced when using the Constant SNR method for antenna pattern correction in the multilook case, in comparison with applying inverse antenna beam pattern descalloping functions. In addition, as the number of looks increases, both methods become less sensitive to the effects of Doppler centroid errors.

The performance of the two methods can also be compared with respect to the variance of the signal to noise ratio (SNR) with azimuth frequency. Recalling EQ 19 from Section 2.3.1, this condition is satisfied if the sum of the weighting functions is equal to one for all frequency values, while the signal energy remains constant over all frequency values. The plots showing noise energy as a function frequency in Appendix B clearly demonstrate this condition is not satisfied for all cases of the inverse beam pattern method. However, the corresponding plots of Appendix C show that the Constant SNR method generates weighting functions which consistently satisfy this condition, and further result in a SNR which is constant over azimuth frequency.

From Table 2.1, it is evident that the inverse beam pattern method generates weighting functions which maximize the equivalent number of looks, and hence minimize the radiometric resolution, for all values of azimuth frequency. However, the weighting functions derived using the Constant SNR method result in an equivalent number of looks which varies as a function of both azimuth frequency and signal level, S. Considering the 4-look case of the Constant SNR method, the optimal signal level for the reduction of radiometric resolution is shown to be 0.65 or 0.7, for the worst case of noise variance simulated, yet the effects of Doppler centroid estimation errors are minimized for S=0.8. This observation will prove significant when interpreting the practical results of implementing selected methods for antenna pattern correction.

As a result of simulation testing, the Constant SNR method for antenna pattern correction has demonstrated increasingly improved performance results as the number of looks increases, for specific signal levels. Chapter 4 presents performance results of these two methods for antenna pattern correction in the practical case.

Chapter 3 Selected Methods for Doppler Centroid Estimation in ScanSAR Data

This chapter begins with an outline of the selected methods for the Doppler centroid estimation problem in ScanSAR data. The implementation of each method is then described in detail. In addition, certain assumptions that are implicit for the ideal performance of each estimator are presented. A discussion of the sensitivity of each estimator to the validity of the assumed conditions for optimal performance is included, and the relative performance of the estimators is predicted for certain scenarios.

3.1 Overview and General Comments

The SAR signal is sampled in azimuth at the pulse repetition frequency (PRF) which is chosen to exceed the azimuth bandwidth, but can be many times less than the Doppler centroid frequency. This causes the signal energy to be wrapped around in azimuth frequency resulting in an ambiguity in azimuth frequency equal to an integer multiple of the PRF [26]. Thus, absolute Doppler centroid estimation involves estimating the integer number of wrapped PRFs in addition to the fractional PRF shift. The integer number of wrapped PRFs is known as the Doppler ambiguity. Techniques for resolving the Doppler ambiguity have been developed, including those presented in [27], [28], [29], [46], and [30].

The methods outlined in this thesis exclusively consider the problem of predicting a model for the fractional Doppler centroid value as a function of the range swath over which it varies. This focus is appropriate since the ENVISAT ASAR will be on a yaw-steered platform whose Doppler ambiguity number can be estimated from other methods.

The model for the fractional Doppler centroid value is to be derived as a polynomial fit through estimates over individual range subswaths.

Several (fractional) Doppler centroid estimation methods are evaluated and compared in this work. Each of the methods selected for analysis can be classified as either a **Spectral Distribution Analysis Method** or as a **Phase Increment Method**. The Spectral Distribution Analysis Methods make use of the fact that the Doppler centroid ideally corresponds to the point of the maximum symmetry of the received spectral energy function in the frequency domain (which assumes the shape of a symmetric azimuth beam pattern). The Phase Increment Methods calculate the phase shift of the corresponding time function, and use the property that the phase difference between the autocorrelation function and the nominal (zero-Doppler) autocorrelation function is proportional to the Doppler centroid. The following paragraphs outline each of the estimation methods selected for analysis, which are subsequently described in detail.

The **Energy Balancing** method [31], [18] is a Spectral Distribution Analysis Method which exploits the symmetry of the azimuth antenna beam pattern and has been traditionally used and evaluated for the Doppler centroid estimation of continuous (or strip mode) SAR data. Another method of frequency analysis is the **Correlation with Nominal Spectrum** method [32], [33], which employs the common strategy of correlating the averaged Doppler spectrum of the complex received signal with the expected antenna pattern model in azimuth. However, the correlation and peak-detection of a range-averaged spectrum with the nominal spectrum is not optimal in the presence of multiplicative speckle noise [24]..Bamler has derived an estimator function for frequency correlation [24] which is "optimal" in the sense that the estimator variance reaches a lower bound defined by the Cramer-Rao inequality from estimation theory [37]-[39],

and thus gives superior performance in the presence of speckle noise.

The **Look Power Balancing** algorithm, developed by Jin in [34], and further detailed by Goulding in [35] is a spectral distribution analysis algorithm which, contrary to the above-mentioned estimation methods, was specifically developed for the ScanSAR data mode (but can also be used on continuous data). The algorithm uses the ratio of overlapping portions of burst intensity images corresponding to the same scene, thus reducing the factor of scene-dependence from the azimuth spectrum. A correct estimate is one for which the total energy in the two looks is equal.

In [19], Madsen presents two Phase Increment Methods for Doppler centroid analysis. The **Correlation-Doppler Estimator** (CDE) method is a computationally efficient time-domain approach which analyses the signal phase rather than the signal amplitude. The **Sign-Doppler Estimator** method is derived from the CDE by exploiting the known statistical properties of the received SAR signal in favour of reducing the number of computations required in the algorithm. In [30], Wong et al presents a Doppler centroid estimation scheme which determines the fractional PRF part of the Doppler centroid using a Phase Increment Method and resolves the Doppler ambiguity using a multilook beat frequency method.

All of the above procedures rely on some degree of averaging over range to alleviate the bias effect introduced by strong point target returns in the received data. By increasing the number of samples with spatial diversity involved in the averaging process, the estimation accuracy is improved, at the expense of a greater computational load. Traditional (continuous-mode) approaches to data averaging typically involve large proportions of contiguous azimuth samples. For the case of ScanSAR data, the number of contiguous samples available in azimuth is limited

by the fixed burst length. This introduces another degree of processing complexity to the ScanSAR Doppler estimation problem, as several data groups over azimuth must now be processed and averaged together, as opposed to one larger group extending over azimuth, as in the continuous mode case.

3.2 Spectral Distribution Analysis Methods

3.2.1 The Energy Balancing Method

The operation of the Energy Balancing Method (EB) is described as follows. An initial estimate of the location of the Doppler centroid within the PRF (at baseband) for a given range subswath is typically available from the satellite orbit and attitude data. This is used to define the center of a fractional region of the PRF over which m evenly spaced frequency values, f_{Pi}, $i = 1$ to m, are input as Doppler centroid estimates for the calculation of m different dE values, where dE is defined below. For each value of f_{Pi}, an azimuth line of range compressed data is extracted and azimuth compressed (using the SPECAN algorithm) with f_{Pi} as the Doppler centroid value. Note that since the variance of a single spectral estimate is very large, the spectra of many azimuth lines over the given range subswath are generated and averaged to increase the SNR of the spectral estimate. Recall (from section 2.2.3) that spectral estimates are generally derived using azimuth compressed data to defeat the problem of partial coverage of point targets which may introduce unnecessary bias into the spectral estimate. The averaged spectral estimate is then used to calculate $dE(f_{Pi})$, the energy difference of two bands, E_1 and E_2, placed above and below the processing Doppler centroid estimate in frequency, defined below. This is illustrated in Figure 3.1.

$$dE(f_{Pi}) = \left.\frac{E_1 - E_2}{E_1 + E_2}\right|_{f_{Pi}} \quad \text{(EQ 30)}$$

Figure 3.1 Energy Balancing Method Illustration

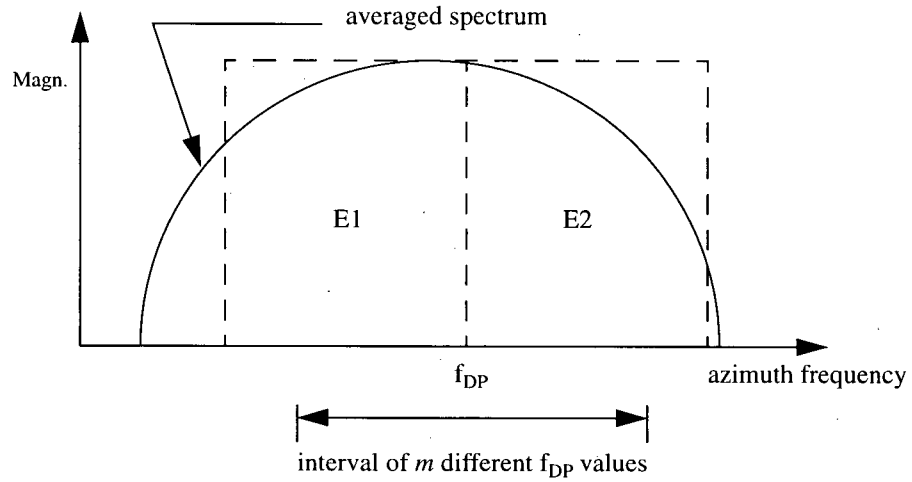

Once all values of dE are calculated for the various processing Doppler frequencies, a curve is fit through the plot of $dE(f_{Pi})$ and the point of zero-crossing defines the measured Doppler centroid estimate as the point of frequency for which the energy on either side is balanced. Figure 3.2 illustrates the calculation of several values of dE (denoted as 'x' points on the lower graph) as a function of several frequency values, f_{Pi}, evenly-spaced over the PRF. The frequency value corresponding to the zero-crossing point of a curve fit through these dE values indicates the measured Doppler centroid estimates (corresponding to 20% of the PRF in this example). This process is repeated over various range subswaths to generate a Doppler centroid estimate model as a function of range.

Figure 3.2 The Energy Balancing Method: Defining the measured estimate

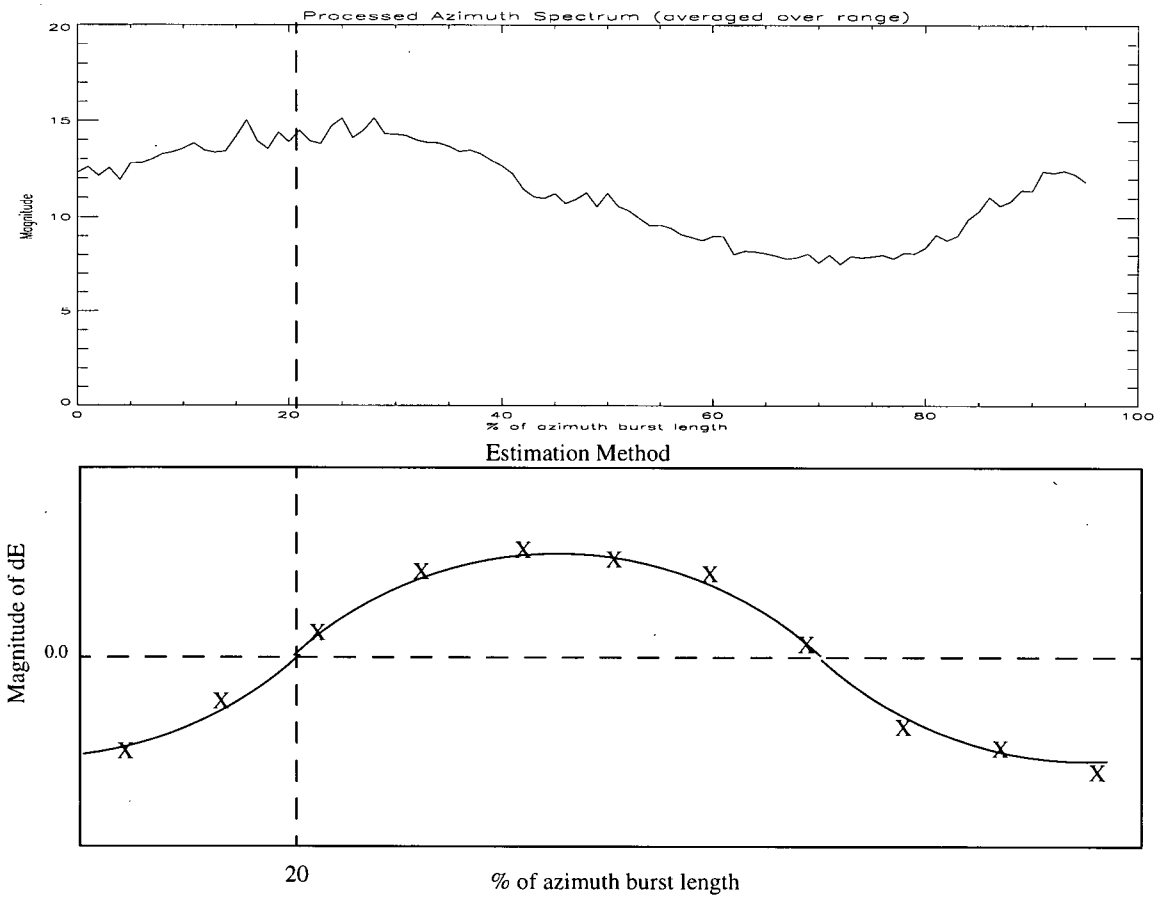

The accuracy of the Energy Balancing Method largely depends on the distribution of the m sample processing frequency points over the chosen frequency region, thus influencing the accuracy of the line fit and resulting zero-crossing point. This presents a trade-off between prediction accuracy and computational efficiency, which may be resolved with knowledge of the degree of noisiness of the estimated spectra, for instance, as fewer estimates need be generated over a relatively smooth averaged spectrum.

METHOD ASSUMPTIONS:

The following are assumptions implicit for the generation of accurate estimation results using this method.

This method assumes that *estimates are calculated from samples extracted from imaged areas of uniform scene reflectivity, such that the spectrum of averaged azimuth data is a fairly smooth function over frequency (assumption **A1**)*. In other words, the scene reflectivity is modelled as a random process which is spatially stationary, such that the variance is not expected to change over the area of estimation. This assumption is no longer valid when the variance of the complex scene reflectivity changes over the area of estimation, which is likely to occur over areas of high scene contrast. This would introduce bias into the averaged frequency domain spectra, and the problem of estimating the frequency point of spectral symmetry becomes more challenging as a result.

Recalling from Section 2.2, the complex SAR reflectivity function is the coherent sum of many randomly distributed scatterers for each imaged resolution cell. *The complex SAR reflectivity function is thus assumed to be modelled as a 2-dimensional Gaussian process containing N samples whose mean approaches zero when N is large {by the Central Limit Theorem} (assumption **A2**)*. This assumption is significant for the successful operation of this method in the following sense. By averaging the complex azimuth spectrum over many samples in range, the symmetric azimuth antenna pattern (which shapes the azimuth spectrum) is assumed to emerge as the predominant spectral pattern because the complex reflectivity function is assumed to have a constant spatial variance. This assumption may not be accurate if the complex reflectivity function received as a result of an imaging terrain which includes strong land-water boundaries. This is because a strong bias would be present due to the variation in backscatter at the coast line which would exist in the spectrum across several samples in range. The prominent spectral pattern would not be that of the azimuth antenna pattern, as there would additionally exist spectral variations due to the scene content which was not effectively averaged out.

Additionally, this method relies on the assumption that *the antenna pattern is symmetric about the midpoint of the spectrum (assumption **A3**).* This assumption is crucial for the identification of that frequency value which properly balances the adjacent energy bands.

In [18], Li reports the estimation error to be on the order of a few hertz, for strip-mode testing of Seasat data using the Energy Balancing method, using azimuth FFT lengths of 2048 samples averaged over 64 range lines for each range area estimate. For evaluation, the estimates over range were fitted to a linear function, and the RMS deviation of each estimate from this function was taken as the estimator standard deviation error. Additionally, Li reports the method to be more accurate for homogeneous regions (oceans) as compared to urban areas, reasoning that the urban scene targets have more backscatter variations as a function of azimuth angle. This is due to the fact that the method is based upon a zero-mean, complex Gaussian ground terrain reflectivity model and continuous data. Errors much greater than a few hertz would arise when the terrain reflectivity is not of a zero-mean Gaussian distribution, such as in the presence of strong land-water boundaries (see above assumption) [20]. This is further confirmed by Madsen, who in [11] demonstrates that the variance of the Energy Balancing estimator is proportional to scene contrast. He also finds that the accuracy of the estimated spectrum improves with the length and number of FFTs, rendering estimator accuracy largely subject to computational expense.

3.2.2 Spectral Magnitude Correlation Methods

As noted previously, the azimuth power spectrum averaged over range shows a pattern similar to the azimuth antenna gain pattern, with a noise floor. Thus, an intuitive approach for the peak detection of the spectrum would be to correlate the nominal spectrum (azimuth antenna beam pattern) with the range-averaged FFT of the complex received data in the azimuth direction,

and locate the spectral peak of the resultant correlation. This constitutes the **Correlation with Nominal Spectrum** (CNS) method, as described in EQ 31 below, where S is the averaged received data spectrum, and B is the azimuth antenna beam pattern model.

$$D(\phi) = \sum_{i=1}^{N} (S(i) \cdot B(i\Delta f - \phi)) \quad \text{(EQ 31)}$$

The value of ϕ for which $D(\phi) = max$ is the measured Doppler centroid estimate.

An example of the voltage of an azimuth antenna beam pattern model, B, for ERS-1 data as obtained from [36] can be given by

$$A(x) = \text{sinc}^2\left(q \cdot \frac{x}{\pi}\right) \quad \text{(EQ 32)}$$

where x is in Hz, and $q = \beta \cdot \frac{\lambda}{2\sqrt{B}}$. The beam fraction term, β, is given in degrees by

$$\beta = 180 \cdot \frac{0.886}{\gamma} \quad \text{(EQ 33)}$$

where the antenna beamwidth, γ, is equal to 0.288 radians. B is a term equal to the product of the ground speed and the platform nadir speed, and has an approximate value of 5.04e7 $(m/s)^2$.

In [24], Bamler finds that the performance of this frequency estimator is determined by the choice of the correlation function, $B(f)$, noting that the correlation and peak-detection of a range-averaged spectrum with the nominal antenna beam pattern model is not optimal in the presence of multiplicative speckle noise. He mathematically derives the shape of the function $B(f)$ which optimizes the estimation accuracy. This constitutes the **Correlation with Optimal Estimator** (COE) method, which is developed in brief below.

The quality of an estimate is often determined by comparing its variance with the Cramer-Rao lower bound [37]-[39]. For any unbiased Doppler frequency estimate ϕ from N data samples, the variance has a lower limit defined as follows, with notation pertaining to this particular estimation problem [24],

$$var\{\phi\} \geq \frac{\Delta f}{\int \left[\frac{A'(f)}{A_s(f) + A_n}\right]^2 df} \qquad \text{(EQ 34)}$$

where $A(f)$ is the nominal power spectrum comprised of both signal and noise spectral components, in the form $A(f) = A_s(f) + A_n$, and the integration extends over one spectral period. In his development, Bamler derives an expression for the variance of $D(\phi)$ from EQ 34 above, treating the function as a stochastic process with an approximate Gaussian distribution, and derives $B(f)$ such that $E\{D(\phi)\} = 0$ for $\phi = f_{D_c}$ the Doppler centroid. Then, the variance of the estimate is finally found to be

$$var\{\phi\} = \Delta f \cdot \frac{\int (A(f) \cdot B(f))^2 df}{\left[\int (A'(f) \cdot B(f))\, df\right]^2} \qquad \text{(EQ 35)}$$

The above equation sets the criteria for the definition of the optimal correlation kernel, $B(f)$, which is presented as

$$B(f) = -\frac{d}{df}\left(\frac{1}{A(f)}\right) = \frac{A_s'(f)}{[A_s(f) + A_n]^2} \qquad \text{(EQ 36)}$$

Upon combining EQ 35 and EQ 36, the Cramer-Rao bound of EQ 34 is indeed satisfied.

Bamler assumes the function $A(f)$ to have the following form, assuming a Seasat or ERS-1-type sensor (with an unweighted azimuth aperture),

$$A(f) = 1 + m \cdot \cos(2\pi f/(PRF)) \quad \text{(EQ 37)}$$

where m depends on both additive noise and the degree of aliasing (in [9], this parameter is set to 0.65 for yaw-steered mode and to 0.5 for roll-tilt mode). This function is referenced in the discussion below, and appears in Figure 3.3.

METHOD ASSUMPTIONS:

Similar to the Energy Balancing Method, the accuracy of the Spectral Magnitude Correlation Methods depends on the validity of assumptions related to scene reflectivity and the distribution of individual scatterers. The breakdown of one or both of assumptions ***A1*** or ***A2*** from Section 3.2.1 is predicted to generate correlation result errors. This is because the shape of the input correlation signal (the received and averaged SAR signal) would generally show deviations from a nominally smooth and symmetric input function, as generated from a scene of uniform reflectivity whose averaged complex backscatter signal can be modelled as a zero-mean, Gaussian process.

The performance of the Spectral Magnitude Correlation methods additionally depends on a third assumption. Both the CNS model and the COE model assume that *an accurate model of the azimuth antenna pattern is known (assumption **A3**)*. Both methods may yield inaccurate results if there is a significant discrepancy between the azimuth antenna pattern model and the actual spectral pattern as measured from averaging a substantial number of azimuth spectra.

In Figure 3.3, an averaged azimuth spectral function as measured from a typical ERS-1 SAR satellite data scene is compared with the two separate antenna pattern models: the Correlation with Nominal Spectrum function (EQ 32) and the Correlation with Optimal Estimator nominal antenna pattern model of EQ 37. The Correlation with Optimal Estimator function (EQ

36, as derived from EQ 37), is also plotted, for reference.

Figure 3.3 Comparison of Azimuth Antenna Pattern Modelling Functions

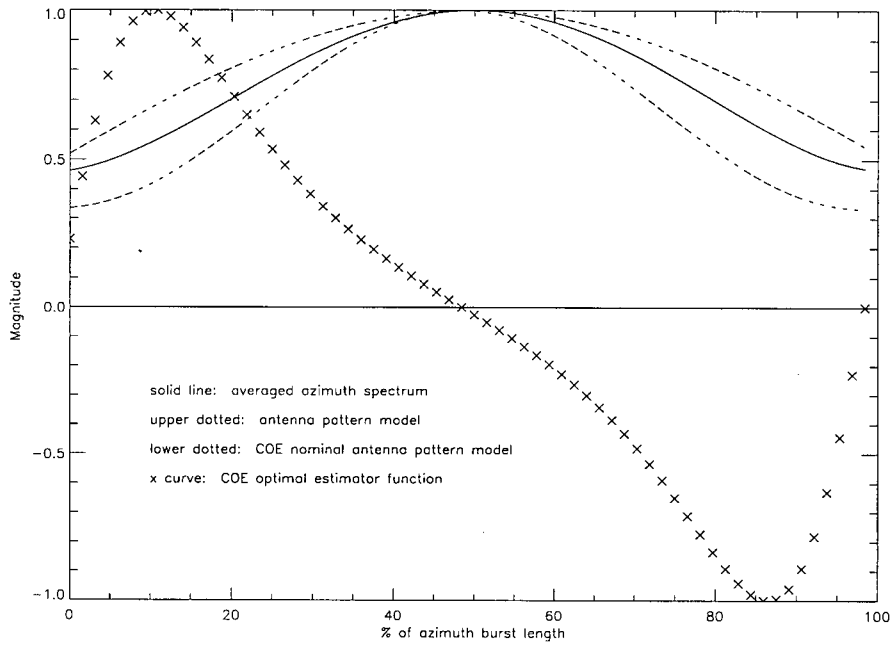

Both the CNS model and the COE model (upper and lower dotted lines, respectively) appear to reflect the measured spectrum (solid line) to a similar degree. It is expected that the COE method performance may be less sensitive to the accuracy of the antenna pattern model since the COE correlation function is designed to be more robust under less favorable SNR conditions. This is because by correlating the measured spectrum with a function related to the reciprocal of the nominal spectrum (this is achieved by the COE), spectral regions with low energy, and thus low speckle noise, contribute more than areas of the spectrum with high energy, thus reducing the bias introduced to the correlation result due to this multiplicative noise [24].

The results presented in [24] demonstrate that this method achieves slightly superior performance in comparison to the other methods tested (Energy Balancing, Correlation Doppler Estimator), all yielding standard deviation errors of under 2 Hz, for a Seasat scene, with estima-

tion blocks of 4096 azimuth samples averaged over 64 range samples.

3.2.3 Look Power Balancing Method

Jin has developed a method specifically for the Doppler centroid estimation of ScanSAR data, using at least 2 azimuth processing looks in the same azimuth burst [34]. This method is referred to as the Look Power Balancing Method (LPB). It is demonstrated in [34] that this algorithm achieves Cramer-Rao's lower bound of EQ 34 for the estimation problem. Considering the 2-look case, the Doppler centroid is measured as the processing Doppler centroid value which yields a ratio of two adjacent burst image intensities of constant magnitude. By basing the estimation method on the analysis of independent image look ratios, the algorithm is less susceptible to the effects of scene contrast (reflectivity) variations than the algorithms previously presented in this chapter. The method, as presented in [34] and further developed in [35] is summarized below for the 2-look scenario.

The raw data of a scene region is range and azimuth compressed, using an initial Doppler centroid estimate, k_{dc} frequency samples (each sample of size PRF/{azimuth FFT length} Hz) as derived from the orbit parameters. Let S_1 and S_2 represent detected portions (of length N_x [1]) of two adjacent azimuth burst intensities at a constant range location r, for k = 1 to N_x samples. Then,

$$S_1(r,k) = \sigma_1(r,k)\gamma_1(r,k) \qquad \text{(EQ 38)}$$

[1] N_x represents the number of 'good points' yielded from the deramp and FFT of the SPECAN method of azimuth compression.

$$S_2(r,k) = \sigma_2(r,k)\gamma_2(r,k) \quad \text{(EQ 39)}$$

where σ_i is the backscattering coefficient of the scene region for each look (σ_1 and σ_2 are assumed to be the same as the same patch of ground is imaged), and γ_i is the speckle noise component (a random, exponentially distributed process) associated with each look. After the application of a correctly positioned radiometric correction function $W(k)$ to each burst, the corrected spectrum functions,

$$C_1(r,k) = W(k)\, S_1(r,k) \quad \text{(EQ 40)}$$

$$C_2(r,k) = W(k)\, S_2(r,k) \quad \text{(EQ 41)}$$

and portions of each burst corresponding to the same patch of ground can be extracted, as

$$X_1(r,m) = C_1(r,\phi_1) \quad \text{(EQ 42)}$$

$$X_2(r,m) = C_2(r,\phi_2) \quad \text{(EQ 43)}$$

where $\phi_1 = k1i$ to $k1f$ and $\phi_2 = k2i$ to $k2f$, and $k1f - k1i + 1 = k2f - k2i + 1 = \frac{N_x}{2}$ samples. These terms, along with the above-mentioned functions are illustrated in Figure 3.4 which presents a graphical illustration of the Look Power Balancing Method, as discussed later in this section.

Figure 3.4 Illustration of Look Power Balancing Method Implementation

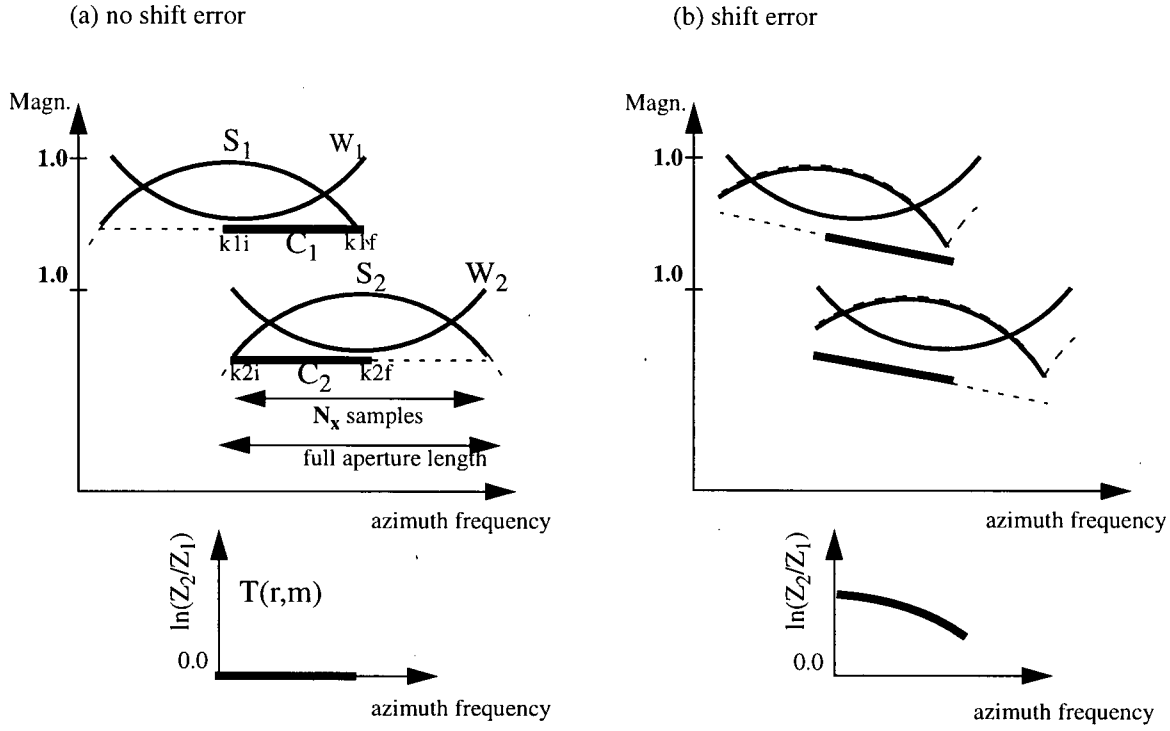

These two look portions are low-passed filtered to reduce the variance of the data, yielding filtered outputs $Z_1(r,m)$ and $Z_2(r,m)$.

Then, by taking the ratio of the terms Z_1 and Z_2, one can eliminate the backscatter coefficient associated with each look (recalling expressions σ_i from EQ 38 and EQ 39) which is generally unknown and unpredictable. Thus,

$$t(r,m) = \frac{Z_2(r,m)}{Z_1(r,m)} = \frac{W(\phi_2)\,\gamma_2(r,\phi_2)}{W(\phi_1)\,\gamma_1(r,\phi_1)} \qquad \text{(EQ 44)}$$

However, the ratio of the random speckle noise process terms has an unbounded variance. Simply taking the natural logarithm of the above expression changes the ratio of the speckle noise terms from multiplicative to additive.

$$T(r,m) = \ln\left(\frac{Z_2(r,m)}{Z_1(r,m)}\right) = \ln\left(\frac{W(\phi_2)}{W(\phi_1)}\right) + \ln\left(\frac{\gamma_2(r,\phi_2)}{\gamma_1(r,\phi_1)}\right) = A(m) + B \qquad \text{(EQ 45)}$$

Furthermore, when the above expression, shown in Figure 3.4, is averaged over several samples in range, by the Central Limit Theorem, B becomes Gaussian distributed process with a mean of zero and a variance of 3.29 [34].

$$L(m) = \sum_{r=R_1}^{R_2} T(r,m) \qquad \text{(EQ 46)}$$

One can now apply a matching technique based on correlation for the detection of the point of equal look powers, which leads to the Doppler centroid measure. Alternately, Goulding presents in [35] a comparison method based on the generation of a set of reference template functions for each initial Doppler centroid estimate k_{dc}. This is achieved by multiplying the azimuth antenna beam pattern model by its inverse, for various inverse functions (each shifted in frequency sample increments) and extracting the two look portions from the squared product. After applying a low-pass filter to the two looks, the natural logarithm of their ratio is taken. A family of reference templates is thus generated for a range of shifted increments centered around the initial estimate (corresponding to a shift of zero). The measured logarithmic ratio of EQ 46 is thus compared to each of the generated template functions. The Doppler centroid estimate is then obtained by adding the index of the template function which yields the closest match (a least-squares comparison is applied) to the initial estimate (all in frequency samples). The value in hertz can be calculated by multiplying this last quantity by the PRF and dividing by the azimuth FFT length.

The operation of this algorithm can be illustrated with reference to Figure 3.4, which depicts the aspects of the method of Look Power Balancing for (a) a correctly predicted Doppler

centroid initial estimate, and (b) an initial estimate of the Doppler centroid which is in error of roughly 10% of the PRF. For the purposes of this illustration, the spectra shown for a given range value are assumed noiseless.

The effective gain in azimuth applied to any point on the ground is the product of the azimuth antenna pattern, the applied correction function, the backscatter coefficient of the ground region, and the speckle noise component of the ground region. As shown above, by taking the logarithmic ratio of two independent look products and averaging over range, both the backscatter coefficient and the speckle noise component terms are effectively eliminated as deterministic factors of the result. The azimuth antenna pattern and the applied correction function are thus the only factors which contribute to the determination of the logarithmic ratio function. When the Doppler centroid estimate is correct; the product of the azimuth antenna pattern and the applied correction function is constant and equal for both looks. Thus, the resulting logarithmic ratio function in this case is constant and zero. When the Doppler centroid estimate is incorrect, however, the product of the azimuth antenna pattern and the applied correction function is not constant, nor is it equal for both looks. In this case, the resulting logarithmic ratio function is not constant and nonzero. By predicting (using a matching technique such as template modelling) the shape of different logarithmic ratio functions, the Look Power Balancing method can identify and quantify Doppler centroid estimation errors.

METHOD ASSUMPTIONS:

Similar to the Magnitude Spectral Correlation Methods, the accuracy of the Look Power Balancing Method relies on the validity of the assumption that *an accurate model of the azimuth antenna pattern is known (assumption **A3**)*. It is expected that the estimation performance is

sensitive to the accuracy with which the antenna pattern model reflects the measured spectrum.

In addition, this method assumes that *the logarithm of the ratio of the speckle noise components of two looks imaging the same patch of ground is an additive process. When averaged over several samples in range, this ratio is assumed to become a Gaussian distributed process with a mean of zero and a variance of 3.29 (assumption **A4**).* It is expected that regions of high scene contrast may present scenarios where this assumption could break down, thus rendering the method susceptible to speckle noise.

Note that the performance of the Look Power Balancing Method does not rely on the validity of assumptions related to scene reflectivity and/or the distribution of individual scatterers. It is thus predicted that the performance of this method is less sensitive than other methods to areas of high scene contrast and/or areas containing land-sea boundaries.

Jin presents the results of estimations performed using bursted ERS-1 data (to simulate the ScanSAR scenario) of both a sea-ice region and a mountainous region. The estimation accuracy of the Look Power Balancing method was compared to that of Bamler's Optimal Estimator method for these two scenes, using an azimuth overlap region of 64 samples, averaged over 128 samples in range (equivalently, 1024 azimuth samples by 8 range samples for the continuous Optimal Estimator method). Similarly to earlier accuracy measures, the estimates were fitted to a linear function over ground range, and the deviation of each estimate from this function was taken as the estimation error. While the Look Power Balancing method definitely outperforms the latter method in the high contrast (mountainous) scene, both methods yielded similar errors for the low-contrast (sea-ice) data (estimation errors generally ranged from 9.5 to 12 Hz). Additionally, Mittermayer reports (in [40]) a sensitivity of the Look Power Balancing method to low signal to

noise ratios, and to antenna pattern shape discrepancies.

3.3 Phase Increment Methods

Madsen has developed a time-domain approach to the Doppler centroid estimation problem. The **Correlation Doppler Estimator** (CDE) [19] measures the Doppler centroid from phase increments in the raw signal data, as opposed to analyzing spectral amplitude characteristics. Phase increments of the signal data are derived from the Averaged Cross Correlation Coefficient of adjacent azimuth samples [41]. The method as presented in [19] and [41] is summarized below.

The autocorrelation function, $R_r(n)$, of the discrete azimuth complex received time domain signal *h(n)* (assumed to be a stationary, stochastic process) of length *N* samples at a specific range index *r* can be expressed as

$$R_r(r,n) = \frac{1}{N} \sum_{m=1}^{N} h(n+m)\, h^*(m) \Big|_r \qquad \text{(EQ 47)}$$

This function is then averaged over several range samples,

$$R(n) = \sum_{r=R1}^{R2} R_r(r,n) \qquad \text{(EQ 48)}$$

to reduce the variance. Then, recalling the shifting property of the Fourier Transform, shifting a signal (the power spectral density function) in the frequency domain imposes a linear phase shift on the time-domain autocorrelation function which can be measured to yield the size of the frequency shift. Assume that the power spectral density $S_o(k)$ of length *N* samples is shifted by k_{dc} frequency samples to form *S(k)*. Then,

$$S(k) = S_o(k - k_{dc}) \quad \text{(EQ 49)}$$

and

$$R(n) = e^{j\frac{2\pi}{N}nk_{dc}} R_o(n) . \quad \text{(EQ 50)}$$

Thus, the Doppler centroid can be measured as the difference between the phase of the measured autorrelation function and the nominal (non-shifted) autocorrelation function, $R_o(n)$, of phase value zero. This phase can be expressed in terms of frequency samples, constituting the Doppler centroid shift k_{dc} in the following manner,

$$k_{dc} = \frac{N}{2\pi n} \arg \{R(n)\} \quad \text{(EQ 51)}$$

where the function *R(n)* can be obtained from EQ 48.

Note that the phase value of the function *R(n)* is measured at a lag of one time sample (n=1). In this sense, the algorithm measures the Doppler centroid shift by quantifying the change in phase incurred by correlating the received signal with itself at a lag of one time sample. This can be further explained with reference to Figure 3.5.

The upper illustration of Figure 3.5 represents the phase of a linear FM signal, $\theta(n)$, whose minimum corresponds to the Doppler centroid value (in time) at a phase of zero. Every target experiences a linear FM phase history. The phase history of a target as observed by an imaging system during a time interval T_o corresponds to a portion of $\theta(n)$ centered about time sample t_o. Then, the lower plot illustrates this change in phase per pulse (or at an increment of one time sample) experienced by a point target as it passes through the beam of the imaging system. The Doppler centroid value obtained from EQ 51 can be related to the lower plot of Figure 3.5 in

the following manner. Consider the expansion of the value $\arg\{R(n)\}$ shown below, with reference to EQ 47, and using the complex identity $h(n) = A(n)\,e^{j\theta(n)}$, at a constant range. Then, $\arg\{R(n)\}$ can be rewritten as

$$\arg\{R(n)\} = \frac{1}{N}\arg\left(\sum_{m=1}^{N} A(n+m)\,e^{j\theta(n+m)}\,A(m)\,e^{-j\theta(m)}\right). \qquad \text{(EQ 52)}$$

Figure 3.5 Graphical Illustration of Phase Increment Method for Doppler Centroid Estimation

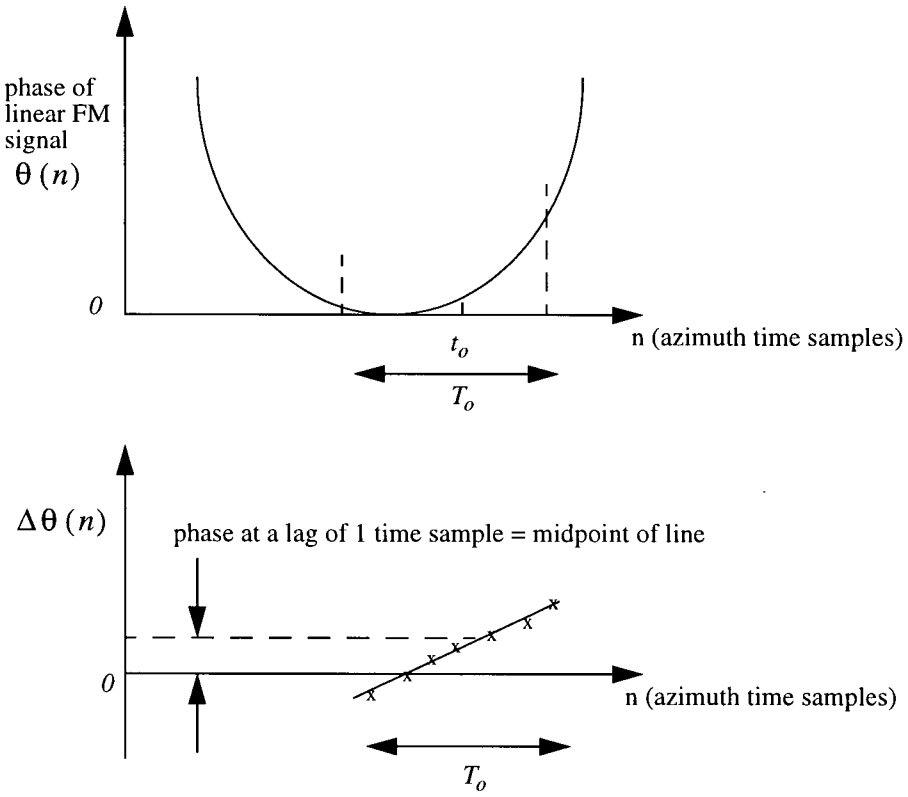

This can be further expanded for $n = 1$,

$$\arg\{R(1)\} = \frac{1}{N}\arg\left[e^{j\theta(1+1)}e^{-j\theta(1)} + e^{j\theta(1+2)}e^{-j\theta(2)} + e^{j\theta(1+3)}e^{-j\theta(3)} + \ldots + e^{j\theta(1+N)}e^{-j\theta(N)}\right] \qquad \text{(EQ 53)}$$

which can be rewritten as

$$\arg\{R(1)\} + \frac{1}{N}[(\theta(2)-\theta(1)) + (\theta(3)-\theta(2)) + (\theta(4)-\theta(3)) + \ldots + (\theta(1)-\theta(N))] . \quad \text{(EQ 54)}$$

The midpoint line drawn in the lower plot of Figure 3.5 is thus a graphical representation of the result of EQ 54 for the calculation of a Doppler centroid estimate using the Phase Increment method.

This method can be further described by considering the process by which the individual phase increments are summed to estimate the centroid. This summation can be illustrated by considering each phase increment to be a vector in the complex plane. Then, increments of the phase are equal to the instantaneous frequency of the target divided by the PRF. When a target is adequately sampled in azimuth, the difference between the smallest and largest phase increment do not exceed 2 pi (in the absence of noise). If the oversampling ratio is 1.2, then the range of phase increments are confined to (2*pi)/1.2. Thus, when the phase increments are plotted in the complex plane, they do not overlap, and unambiguously represent the fractional part of the Doppler frequency.

When drawing the phase increments in the complex plane, it is seen that they are weighted towards the centroid. Thus, finding the average phase increment by adding the individual phase increments together in the complex plane (i.e., using vector addition), the centroid can be estimated. This is illustrated in Figure 3.6, for a Doppler centroid of PRF/5 (corresponding to the scenario depicted in Figure 3.5). Note that if receiver noise is present, it contributes equally in all directions of the complex plane, so does not bias the estimate [47].

Figure 3.6 Illustration of Phase Increment Summation in the Complex Plane.

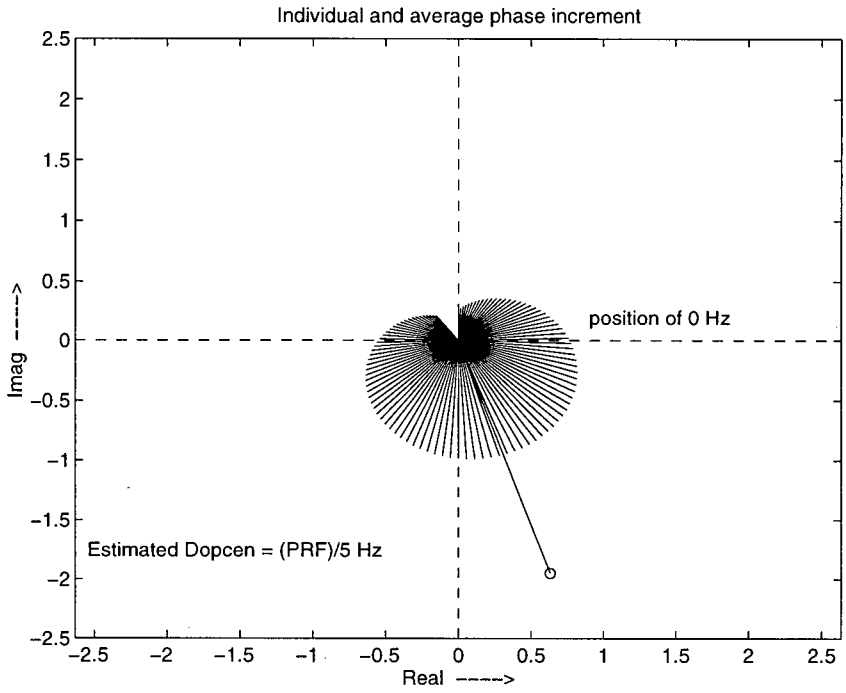

With the **Sign-Doppler Estimator** (SDE) [19], Madsen derives the correlation coefficients of the received complex SAR signal by simply analyzing the sign of the data values in favour of reducing the complexity of the estimation computations, where many of the repeated calculations become sign comparisons (computationally simple) which renders the process more attractive for real-time implementation. An additional advantage to considering only the sign of data samples is in the resulting equalization of the weighting of strong and weak point targets such that the estimator is less sensitive to strong scene content changes [42]. The highlights of the method derivation are presented below.

Recalling $h(n)$ from EQ 47 to be a complex number, where $h(n) = I(n) + jQ(n)$, with $I(n)$ and $Q(n)$ both being real Gaussian processes, then the Arcsine Law of Gaussian processes [21] can be applied to calculate the autocorrelation function. Stated precisely, if the real part and the imaginary part of a complex digital signal are nearly Gaussian processes, then the autocorrelation

function can be calculated only by examining their signs. Further details of this method are systematically presented in [19], and will not be repeated here. Finally, the Doppler shift, k_{dc}, can be expressed in frequency samples as

$$k_{dc} = \frac{N}{2\pi n} \arg \{ \rho (n) \} \qquad \text{(EQ 55)}$$

where $\rho (n)$ is the normalized correlation coefficient derived from autocorrelations of the sign values of the complex data.

METHOD ASSUMPTIONS:

Similar to several methods presented above, the accuracy of the Phase Increment Methods depends on the validity of assumptions related to scene reflectivity and/or the distribution of individual scatterers (assumptions ***A1*** and ***A2*** from Section 3.2.1). With specific reference to assumption **A2**, the Sign Doppler Estimation method assumes that the complex received SAR signal can be modelled as a Gaussian distributed process. This assumption is necessary for the implementation of the Arcsine Law of Gaussian process for the derivation of the autocorrelation function. The Sign Doppler Estimation Method is likely to produce estimates with less accuracy when either of assumptions ***A1*** and ***A2*** are no longer valid, such as in the case of regions of high scene contrast or those containing land-sea boundaries (as stated in earlier sections).

As a result of simulations using data blocks of 2048 azimuth samples over 64 range samples from a relatively non-homogeneous Seasat scene, Madsen reports the accuracy of the SDE estimates to be on the order of both the CDE and the Energy Balancing methods. The SDE method did outperform the other methods by a small margin (estimation errors ranged from 6 to 10 Hz, roughly), yet with a significant savings in computation time. Additionally, both methods

were found to have an estimation error variance which is proportional to scene contrast, and further testing of different scene data was quoted as a subject of future work.

Chapter 4 Doppler Centroid Estimation Method Simulations and Comparison Results

This chapter begins by describing the selection and processing of the scene data used for analysis. The objectives, simulation method, and results of two measures used to quantify the relative estimation performance of the selected methods for Doppler centroid estimation are then described in detail. The results of simulations are presented with reference to the predicted performance of the estimators based on the validity of certain assumptions developed in Chapter 3. This is followed by a brief discussion of estimator computational efficiency. The results are then summarized in the final section of the chapter.

4.1 Scene Data Selected for Analysis

As ENVISAT satellite (to be launched in 1998) raw data was not available at the time of this study, all simulations were carried out using data acquired from the first Earth Resources Satellite (ERS-1). On July 17, 1991, the European Space Agency (ESA) launched ERS-1 and so began the first major European global satellite mission for the collection of worldwide geographic earth monitoring data. The ERS-1 satellite operates on a sun-synchronous, near-polar orbit, at a nominal altitude of 785 km. The remote sensing instrumentation includes an active microwave instrument containing a SAR capable of obtaining scene data strips to create an image of an area approximately 100 km (azimuth) by 100 km (ground range) in size, at a nominal incidence angle of 23 degrees in normal yaw-steering mode. During the first half of April 1992, the satellite operated in a Roll-Tilt mode (RTM) to allow experimentation with the SAR at an incidence angle of 35 degrees instead of the normal mode 23 degrees, thereby permitting analysis of a totally different set of signatures from objects on the Earth's surface. While in Roll-Tilt Mode, the

satellite antenna motion is no longer guided to compensate for earth rotation effects as is the case of yaw-steering mode. As pertaining to the problem of Doppler centroid estimation, this results in an increased maximum Doppler centroid drift over the imaged range swath.

Two ERS-1 raw data scenes were selected for this investigation. Each scene contains approximately 5500 range samples by 28000 range lines of raw data, corresponding roughly to a 100 km square patch of ground. The **Netherlands Scene** was acquired in Roll-tilt mode during orbit 3760 on April 4, 1992. This scene captures the south-western coastal region of the Netherlands bordering on the North Sea, and is characterized by several land-water boundaries which pose a challenge to the problem of Doppler centroid estimation (please refer to section 2.2.2). Also present is a region of strong reflectors surrounded by the sea which present an additional challenge for localized Doppler centroid estimation.

The signal data for the **Squamish Scene** was acquired by the ERS-1 SAR in yaw-steered mode during orbit 4123 on April 29, 1992. This scene captures the mountainous terrain of Squamish, British Columbia and is a suitable candidate for evaluating Doppler centroid estimators over areas of high scene contrast. Some land-water boundary features exist in the scene, but none were included in the areas seletected for estimation.

4.1.1 Scene Data Processing

All processing was carried out using the SPECAN algorithm as implemented by Ngo and Vigneron in [15], modified for ScanSAR simulations. The scenes were processed using typical ERS-1 parameters as listed in Table 4.1, using one look for both range and azimuth compression. FFT lengths of 256 samples (range) and 64 samples (azimuth) were used for compression,

yielding output image resolution cells of pixel spacing 60.7 m (ground range) by 90.4 m (azimuth). Doppler centroid estimation simulations were performed on range compressed data as

Table 4.1 ERS-1 Parameters Used for Scene Processing

Range Bandwidth	15.55 MHz
Range FM Rate	4.188e11 Hz/s
Range Sampling Rate	18.983 MHz
Range FFT Length	256 samples
Radar Wavelength	0.0567 m
Pulse Repetition Frequency (PRF)	1680 Hz
Azimuth Oversampling Ratio	1.2
Radar platform speed (approximate)	7035 m/s
Nominal Slant Range	856 km
Azimuth FFT Length	64 samples
Nominal Azimuth FM Rate	2043 Hz/s

opposed to raw range data in order to increase the dynamic range of the signal and the standard deviation of the Doppler estimates [42]. In addition, the range dependence of the Doppler centroid drift is kept distinct in the estimation methods by using range compressed data.

4.2 Comparison of Methods Based on RMS Deviation of Estimates over Range

4.2.1 Objectives of Study

In theory, the Doppler centroid varies approximately linearly over ground range [18], [7]. One way to evaluate the performance of an estimator is to fit a linear function over ground range to several estimates computed over specific extents in range and calculate the RMS deviation of the estimates with respect to the line to give an indication of each estimator's standard deviation. Several authors [18], [24], [11] have used this method to measure the relative performance of

different estimators.

This research work involves the investigation of the radiometric effects of Doppler centroid errors and aims to quantify the relative performance of selected Doppler centroid estimation techniques with respect to output radiometric image quality. Although the precise Doppler centroid value is very difficult to quantify, one can determine that Doppler centroid estimate (accurate to within one frequency sample[1]) which yields the least amount of azimuth residual scalloping for a given number of averaged data samples. Thus, the approach for the relative comparison of estimators is a modification of the above method in the following manner. Rather than calculating the RMS deviation of the estimates over range with respect to a linear function through the estimate set, the RMS deviation is calculated with respect to a set of 'radiometric truth' values (estimation points measured to yield the least amount of residual scalloping in a gain-corrected azimuth spectrum) measured over range. Using this basis for comparison, the estimator yielding the lowest RMS deviation error is that one which provides estimates for the processing of an image containing the best output radiometric image quality in azimuth.

4.2.2 Methodology of Evaluating Estimators

For each scene, three separate regions of varying scene content were arbitrarily selected over azimuth for the evaluation of the estimators (please refer to Figure 4.1). The scene was further partitioned into eight subswaths over slant range, each of length 200 range compressed samples (a typical subswath length for a ScanSAR system). For each azimuth region, each estimator calculated an estimation of the Doppler centroid value by incorporating the same number of

[1] One frequency sample in for this set of processing parameters is equal to (1680 samples/sec)/(64 FFT azimuth samples) = 26 Hz.

data samples into each estimate measured over slant range. To simulate a typical ScanSAR scenario [18], [9], each azimuth region was divided into 12 bursts, each of length 64 azimuth samples, with an inter-burst gap of 128 azimuth samples. Figure 4.2 illustrates the number of samples involved for the calculation of a single estimate corresponding to the first (slant) range subswath, for a given azimuth region. This calculation consists of averaging the spectral output of a complex 64-point azimuth FFT over the entire range subswath[2]. This spectrum is further averaged together with 11 additional burst groups of data over azimuth, as defined in Figure 4.2, to yield an estimate for a given range subswath.

Figure 4.1 Scene Data Organization

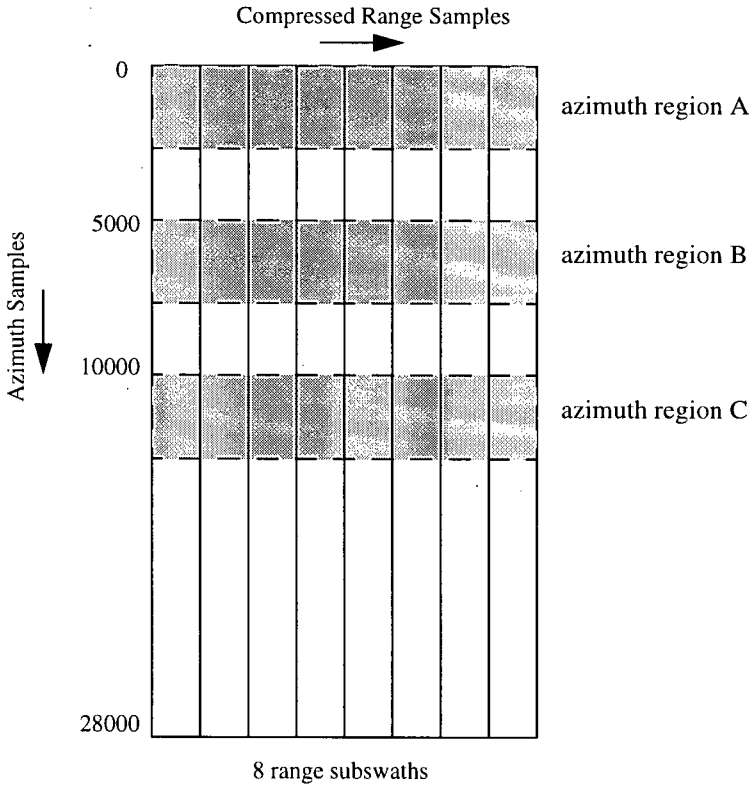

A set of estimations was thus generated as a function of slant range by each of the

[2] The Doppler centroid drift over a range subswath of length 200 range compressed samples was found to be negligible for both cases of roll-tilt mode and yaw-steered ERS-1 data.

candidate Doppler centroid estimators, for each of the three separate azimuth regions.

Figure 4.2 Detailed View of Data Samples Averaged for One Estimation Point (1st range subswath, azimuth region A)

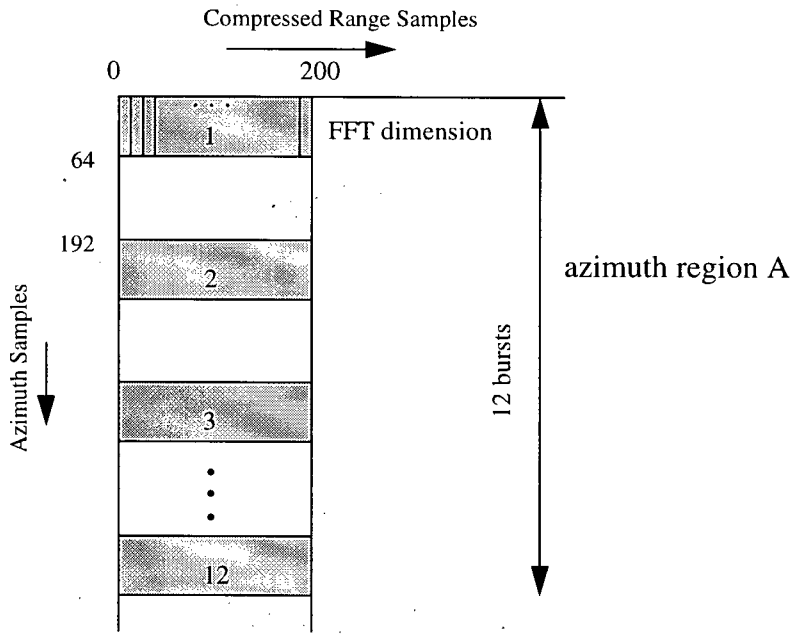

The RMS deviation measure, e_m, for a given estimator m was then calculated with respect to a radiometric truth line, RT (the measurement of the radiometric truth line is described later in this section) as shown below,

$$e_m = \sqrt{\frac{1}{3 \cdot 8} \sum_{n=1}^{3} \left(\sum_{i=1}^{8} [E_m(n,r_i) - RT(r_i)]^2 \right)} \qquad \text{(EQ 56)}$$

where E_m is the set of estimations measured by estimator m as a function of both range subswath r_i and azimuth region n. In addition, a maximum deviation measure, MD_m, of each estimate from radiometric truth line was measured for each estimator in the following manner,

$$MD_m = max_{n,i}\{abs\{E_m(n,r_i) - RT(r_i)\}\}. \quad \text{(EQ 57)}$$

The radiometric truth line for each scene was calculated as a function of slant range subswath by averaging the azimuth FFT spectrum over 83 bursts in azimuth (as illustrated in Figure 4.3), each separated by an inter-burst period of 128 samples, and over the range extent of the subswath. This yielded a radiometric truth vector eight elements in size, where each element represented the radiometric truth value corresponding to a particular slant range subswath. By averaging a substantial amount of data for the generation of each radiometric truth value, the biasing effects of noise and scene contrast variations are assumed to be effectively averaged out, leaving a fairly smooth spectral function. By applying an antenna pattern correction function appropriately shifted in azimuth, the azimuth shift which minimized the amount of residual scalloping present in the "corrected" spectrum was recorded as the Doppler centroid shift (in frequency samples) required to maximize the output radiometric image quality for that particular extent over range.

Figure 4.3 Definition of Samples Averaged for Radiometric Truth

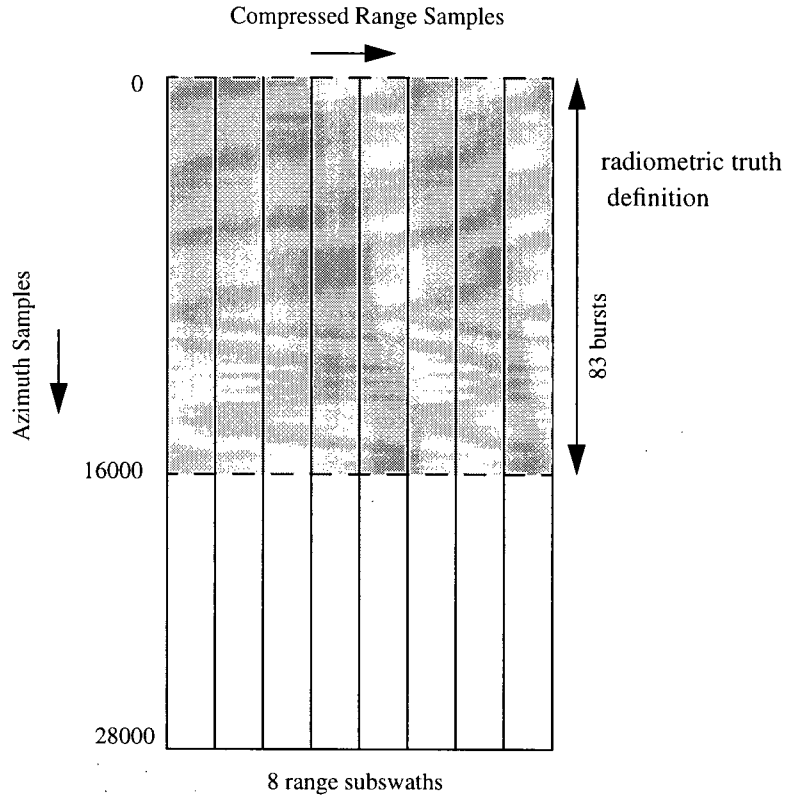

As the Doppler centroid is predicted to vary linearly over ground range, a line was then fit to the radiometric truth vector over ground range, yielding a radiometric truth line, for each scene of data tested.

4.2.3 Results

(i) Netherlands Scene Simulation Results

The following Doppler centroid estimation methods were evaluated in this study: the Energy Balancing Method (EB), the Correlation with Nominal Spectrum Method (CNS), the Correlation with Optimal Estimator Method (COE), the Sign-Doppler Estimation Method (SDE), the Look-Power Balancing Method using the azimuth antenna pattern model from [36] (LPBI), and the Look-Power Balancing Method using the averaged azimuth spectrum to model the azimuth antenna pattern (LPBII)[3]. Appendix F contains six graphs which present the Doppler

centroid estimates over ground range for the simulated methods over each of the three azimuth regions tested as well as the RMS deviation measure calculated for each method. Note that the radiometric truth line as measured for the Netherlands scene is plotted alongside the set of results on each graph for comparison.

Figure 4.4 presents the measured radiometric truth values over ground range, as well as the radiometric truth line fit to these measurements, for the Netherlands Scene. Note that the radiometric truth vector was found to be fairly linear over ground range. This is in accordance with the predicted drift behavior of the Doppler centroid over ground range [7].

Figure 4.4 Radiometric Truth Over Ground Range: Measurement versus Line Fit

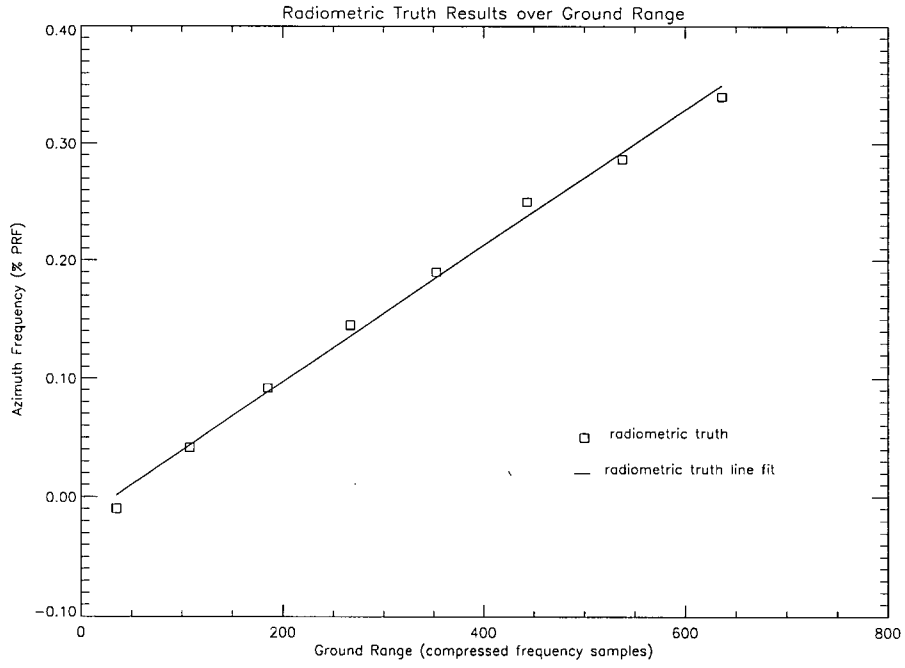

It is thus assumed that the measured radiometric truth line for the Netherlands Scene provides a suitable set of baseline results for the comparison of the selected estimators based on the calcula-

[3] This last method will also be referred to as the Look-Power Balancing Method (II).

tion of RMS deviation values as described in Section 4.2.2.

In order to predict the impact of scene content on the measured RMS deviation results, the reader is encouraged to refer to the results shown in Appendix F with respect to a plot of the processed Netherlands Scene, found for example in Appendix J, Figure J.1. Note that Figure 4.5 contains an example of one of the plots of Appendix F, and presents test results for the Energy Balancing estimation method. The scene extent of the image of Figure J.1 corresponds to that described in Figure 4.1. This scene is found to contain both land and sea regions, with several land-water boundaries as well as several highly reflective targets (showing bright intensities) located in the center region of the image. The plots of Appendix F indicate that each of the methods consistently produced estimates which tended to deviate greatly from the radiometric truth value for the specific region of samples located in the ***sixth subswath*** over slant range within ***azimuth region C*** (recalling the conventions established in section 4.2.3). Upon referring to the processed image plot, one can isolate this region in the scene (located at roughly three-quarters of the slant range extent, and one half of the azimuth extent of the image) as containing several closely spaced groups of bright targets, surrounded by a weakly reflective water surface. This region thus represents an area of high scene contrast. In addition, this region of samples contains a portion of a land-sea boundary.

Figure 4.5 RMS Deviation Measurement Results: Energy Balancing Method, Netherlands Scene

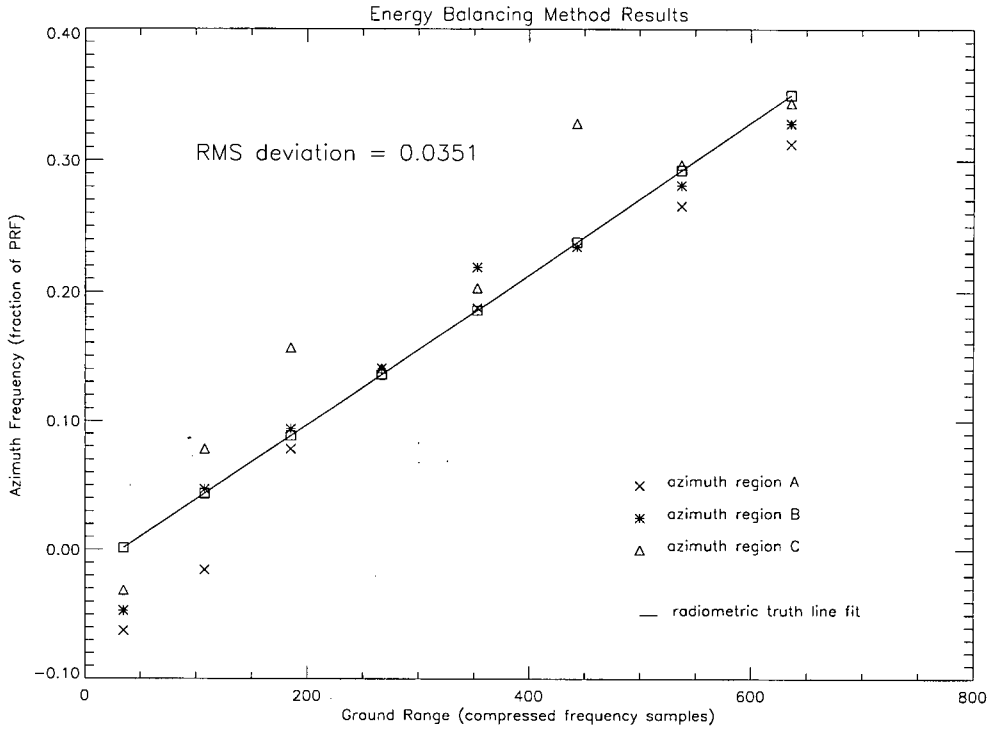

Recall, from Section 3.2.1, assumption ***A1*** (*estimates are calculated from samples extracted from imaged areas of uniform scene reflectivity, such that the spectrum of averaged azimuth data is a fairly smooth function over frequency*) and assumption ***A2*** (*The complex SAR reflectivity function is thus assumed to be modelled as a 2-dimensional Gaussian process containing N samples whose mean approaches zero when N is large {by the Central Limit Theorem}*). It is likely that assumptions ***A1*** and ***A2*** are no longer valid for the samples in this region due to the combination of scene features present. This results in a relatively poor performance of most of the estimation methods, as predicted in Chapter 3. Note that the performance of the LPBII estimator showed the least amount of sensitivity to this scene region.

Conversely, one can consider the region of image samples corresponding to each of the azimuth regions measured over the ***eighth subswath*** in slant range. All three of these regions in the Netherlands Scene (lower to mid extent in azimuth direction, far extent in slant range

direction) correspond to portions of the sea which are not characterized by rapidly-varying bright and dark regions, and thus represent scene areas of relatively low contrast. In addition, this region contains no areas of land-sea boundaries, thus assumptions ***A1*** and ***A2*** are likely more valid for the samples contained in this region. This is reflected in the estimation results plotted in Appendix F, which generally show less deviation from the radiometric truth line than is the case for other range subswaths.

Figures 4.6 and 4.7 summarize the RMS deviation and maximum deviation results calculated for each of the methods for the Netherlands Scene simulations, based on the data presented in Appendix F (also included are the Squamish scene testing results, which will be discussed in the following section).

Figure 4.6 Comparison of RMS Deviation Results

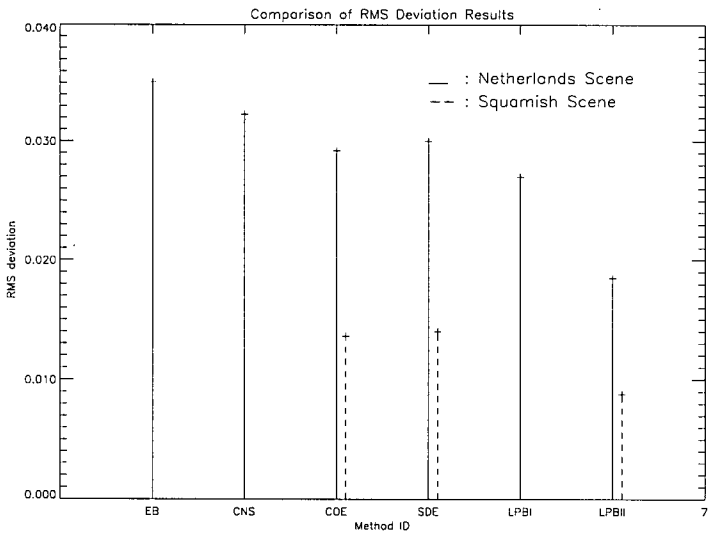

Figure 4.7 Comparison of Maximum Deviation Results

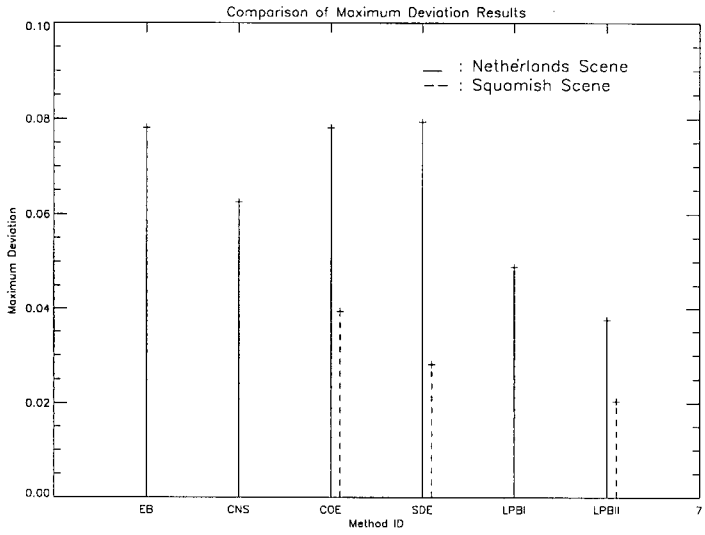

The RMS deviation test results indicate fairly similar estimation performances by all methods tested, with method LPBII showing slightly more favorable estimation results relative to the other methods. The maximum deviation testing results further support this finding. This indicates that the Look-Power Balancing (II) estimator is less susceptible than the other methods to the effects of high contrast scene areas and land-sea boundary areas for Doppler centroid estimation. In addition, the results indicate that the accuracy of the Look-Power Balancing method is sensitive to the choice of function selected for azimuth antenna pattern modelling, as demonstrated by the different estimation results achieved using the Look-Power Balancing method implemented using two distinct antenna pattern modelling functions. Both results in accordance with the predictions section 3.2.3.

(ii) Squamish Scene Simulation Results

Based on the comparative findings shown above, methods COE, LPBI, and LPBII were identified as candidate methods for further testing with this set of data. Appendix G contains the results of this study for the Squamish scene, and an example of the processed image is found in

Appendix J, Figure J.3.

Figure 4.8 presents the measured radiometric truth values over ground range, as well as the radiometric truth line fit to these measurements, for the Squamish Scene. The radiometric truth vector was once again found to be fairly linear over ground range (shown in Figure 4.8). Similar to above, it was thus assumed that the radiometric truth vector for the Squamish Scene provides a suitable set of baseline results for the comparison of the selected estimators based on the calculation of RMS deviation values.

With reference to the plots presented in Appendix G and the processed image, some observations relating the estimation results to scene content may be noted. The image is composed of numerous regions of sharply varying intensities uniformly distributed throughout the entire image, and thus represents a scene of a high contrast. Of additional note is the absence of land-water boundary features in the scene areas for estimation.

Figure 4.8 Radiometric Truth Over Ground Range: Measurements versus Line Fit.

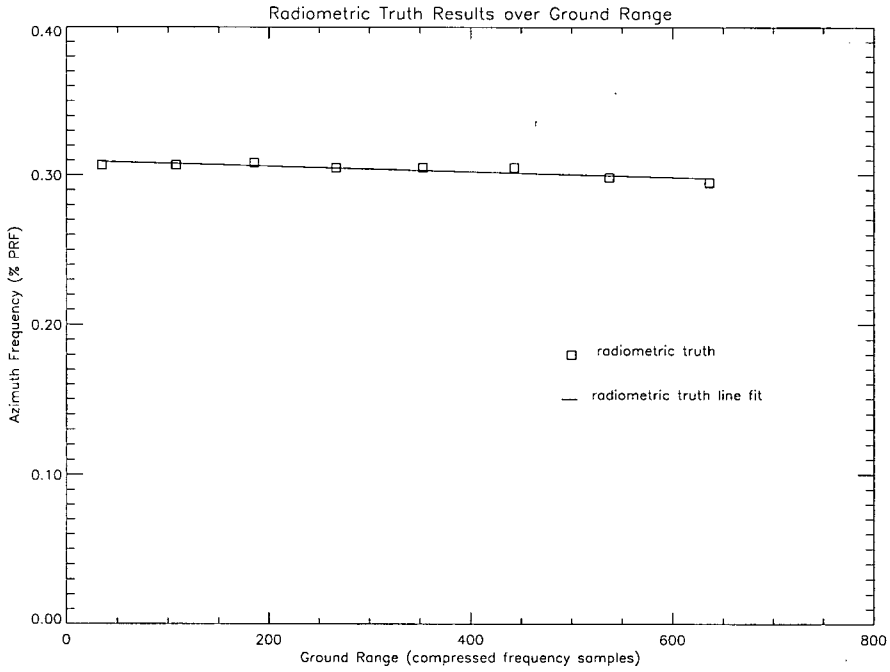

Among the specific groups of data samples over which the estimator performance was evaluated in the study, none demonstrated estimation results which were consistently poor for all methods tested. In addition, the estimation measures were generally found to lie closer to the radiometric truth values when compared with the results from the Netherlands Scene simulations. This is likely due to the fact that the scene reflectivity of the Squamish scene has remained more uniform (e.g. the variance has remained more constant over the scene area) and the complex scene reflectivity of this Squamish Scene is more accurately modelled as a Gaussian distributed process of zero mean (assumptions ***A1*** and ***A2*** of section 3.2.1) than that of the Netherlands Scene. Hence, the performance of the estimation methods is improved for scene data which more accurately represents an ideal case scenario.

The results are presented in summary form in Figures 4.6 and 4.7. The relative performance of those estimators tested with the Squamish Scene tends to be consistent with the results of the simulations performed with the Netherlands Scene. The RMS deviation result of LPBII was once again found to be lower than that of the other methods tested. This result was further supported by the maximum deviation results, indicating once again that the estimation performance of method LPBII tends to be less susceptible to scene areas of high contrast.

4.3 Comparison of Methods Based on Radiometric Quality of Output Images

4.3.1 Objectives of Study

One objective of this study is to quantify and compare the amount of residual scalloping present in the final images processed with each individual estimator. A second objective is to quantify and compare the amount of residual scalloping generated in the output image as a result of applying different antenna pattern correction methods. Specifically, the Inverse Beam Pattern

(IBP) Method and the Constant SNR (CR) Method (for the 1 and 2 look cases) as developed and simulated in Chapter 2 are to be evaluated in this context.

4.3.2 Methodology of Evaluating Estimators

For this set of tests, images were processed using the set of estimates generated over azimuth and range from each estimator[4], as presented in Section 4.2.3. In addition, the range compressed data was azimuth processed using three separate methods for azimuth antenna pattern correction (as developed in Chapter 2), namely the Inverse Beam Pattern Method (one and two look cases), and the Constant SNR Method (2 look case).

For each processed image, an overall measure of residual scalloping was quantified as follows. The output FFT spectra corresponding to a processed and gain corrected burst in azimuth were averaged over each range subswath, and each of these burst group spectra were further averaged over azimuth (for a total of 23 output azimuth burst groups). A measure of residual scalloping, x_i, was calculated for each range subswath (referring to Figure 4.9) by measuring the effective decrease in intensity over the output gain-corrected and averaged spectrum, $\bar{S}$, corresponding to each range subswath. This is given by

$$x_i = abs\{20\log\left(\frac{avgB}{avgA}\right)\} \quad [dB] \qquad \text{(EQ 58)}$$

where *avgA* and *avgB* are the calculated averages of the first and last 10% of spectral magnitude values of $\bar{S}$, respectively. For the calculation of each x_i, it was necessary to average over a large number of samples (within the subswath to be quantified) to minimize the variation of $\bar{S}$ due to

[4] Note that only the three estimator methods which showed superior results from the initial study of Section 4.2 are evaluated in this set of tests.

noise and scene content, such that the spectral variation resulting from the effects of residual scalloping can be seen. Finally, an overall measure of residual scalloping, $\bar{x}$, was assigned to each processed image by averaging the x_i values corresponding to each subswath.

Figure 4.9 Illustration of the Quantification of Residual Scalloping over one Range Subswath of an Output Image

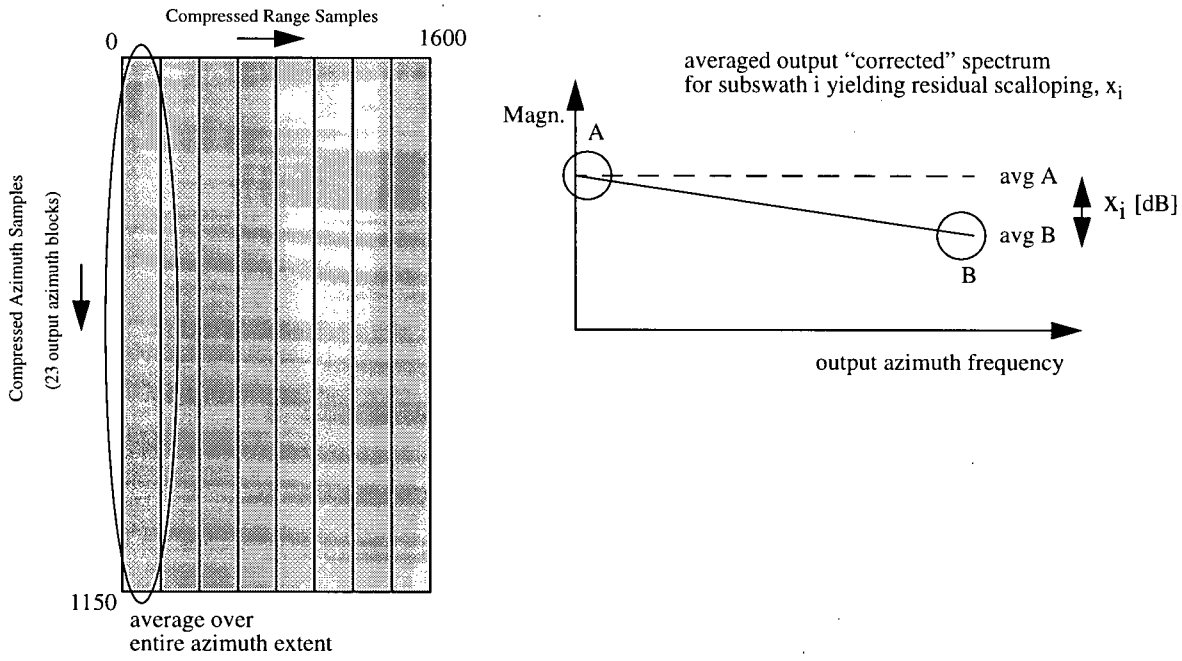

4.3.3 Results

(i) Netherlands Scene

Appendix H contains the results of applying methods COE, SDE and LPBII to process the Netherlands Scene data image. For each estimation method, the quantification of the residual scalloping resulting from applying the Inverse Beam Pattern Method (for 1 and 2 looks) and the Constant SNR Method (for 2 looks) for antenna pattern correction are illustrated. As an example, Figure 4.10 plots the magnitudes of corrected azimuth spectra, averaged over each entire range subswath. For the situation of a perfectly estimated Doppler centroid value corresponding to a particular range subswath, the spectrum would be a flat function of azimuth frequency, assuming

assuming that assumptions ***A1*** and ***A2*** (from Section 3.2.1) were valid and a sufficient amount of averaging has occurred to minimize the spectral variance resulting from terrain backscatter. The spectral variations captured in each plot reflect to some degree the effects of a randomly varying terrain backscatter, but the sloping effect present in the spectra associated with each subswath can be significantly attributed to residual scalloping. Note that for each plot set, the spectral magnitude plots associated with the Constant SNR (2 look) Method for antenna pattern correction are consistently 2.5 dB lower than the remaining two spectral magnitude plots. This arises as a result of the implementation of the method in question, and in no way modifies the measurement outcome. Figure 4.11 presents an example of the averaged azimuth spectral scalloping measure per subswath, corresponding to the plot of Figure 4.10, for the COE method. For each subswath, the three calculated point on each vertical line correspond to each of the three antenna pattern correction methods.

The performance of the Doppler centroid estimation methods as a function of scene contrast can be compared by quantifying the residual scalloping present in processed images generated using the IBP, 1 look scenario for antenna pattern correction, with reference to the example image found in Figure J.1 of Appendix J. Recalling from Section 4.2.3, an image area present within the ***sixth range subswath*** was found to be of high scene contrast and contained land-sea boundaries. With reference to Figures H.2, H.4, and H.6, the averaged azimuth spectral scalloping measure corresponding to the ***sixth range subswath*** consistently shows a significant degree of residual scalloping, for the IBP, 1 look case. Additionally, the low scene contrast regions with no land-sea boundaries found in the ***eighth range subswath*** (as described in Section 4.2.3) correspond to consistently low azimuth spectral scalloping measures, once again for the IBP, 1 look case.

Figure 4.10 Magnitude of Averaged Output Azimuth Spectra (8 adjacent subswaths shown). *antenna pattern correction method: Inverse Beam Pattern, 1 look (plain Line); Inverse Beam Pattern, 2 look (dotted line); Constant SNR Method, 2 look (dashed line).*

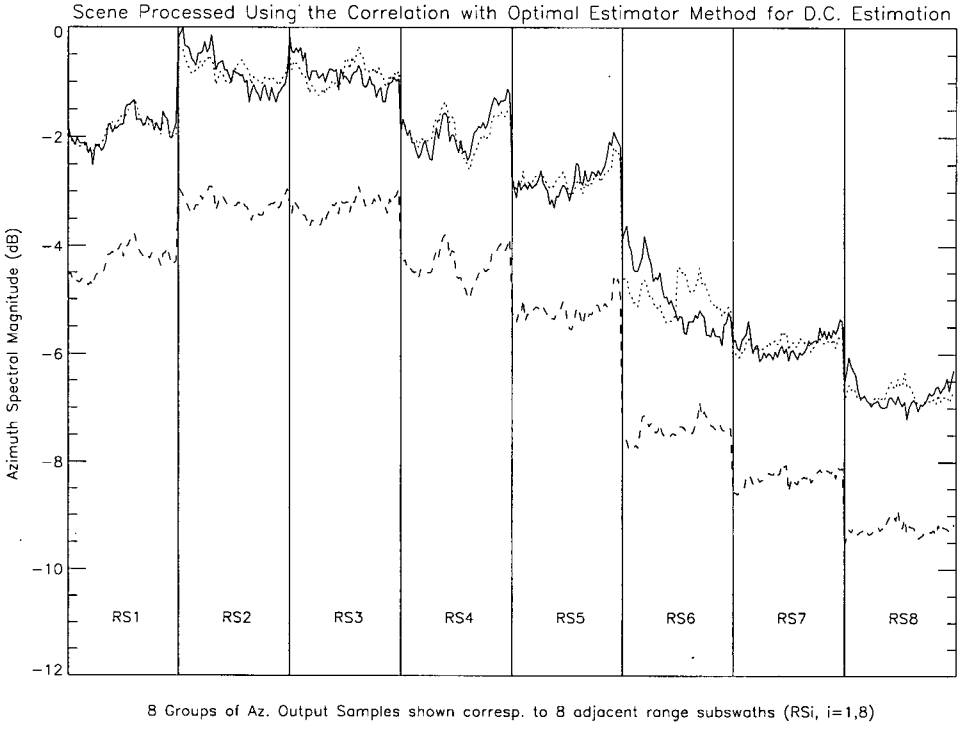

Figure 4.11 Averaged Azimuth Spectral Scalloping Measure per Subswath (8 adjacent subswaths shown). *antenna pattern correction method: Inverse Beam Pattern, 1 look ('x'); Inverse Beam Pattern, 2 look (triangle); Constant SNR Method, 2 look ('*').*

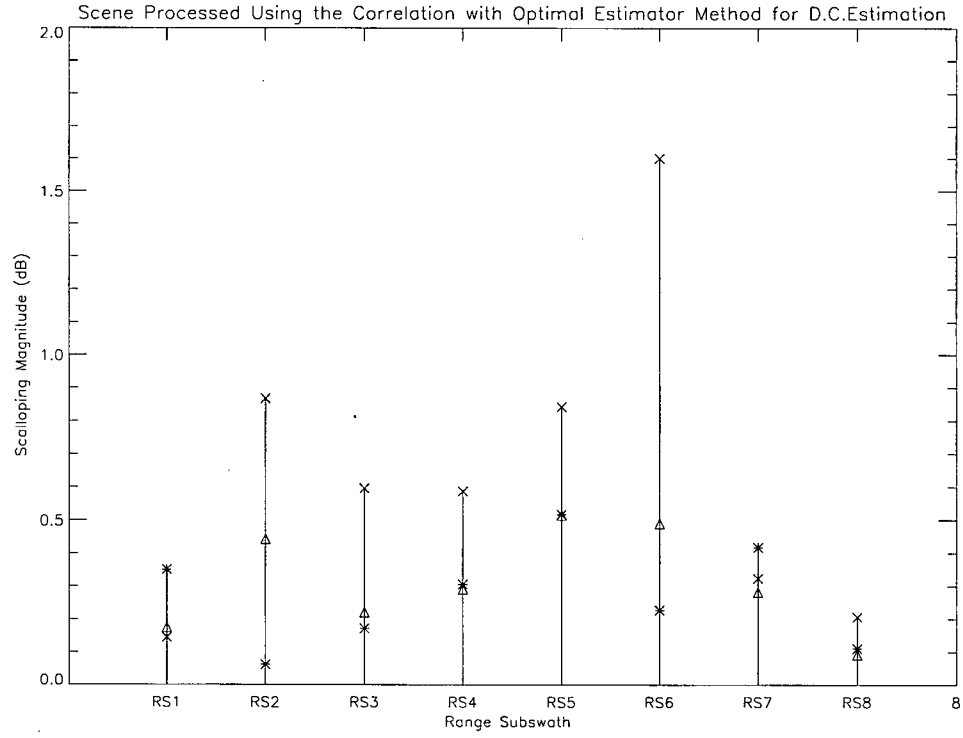

Table 4.2 summarizes the overall azimuth scalloping measures, as derived in Section

Table 4.2 Overall Azimuth Scalloping Measures (dB), Netherlands Scene

	A.P.C. Methods			D.C.Est. Error
estimator	IBP, 1L	IBP, 2L	CR, 2L	(Hz)
COE	0.65	0.31	0.27	19.8
SDE	0.61	0.29	0.27	17.8
LPBII	0.54	0.26	0.28	14.4
rad. truth	0.47	0.22	0.25	-

4.3.2, for simulations carried out with the Netherlands Scene, for the three methods of antenna pattern correction. Also included are the measured results of images processed using the set of Doppler centroid estimates derived as the radiometric truth vector, for comparison. The overall azimuth scalloping measure, $\bar{x}$, derived using the radiometric truth vector set of estimates is expected to approach zero in the ideal case, for a given antenna pattern correction method. The results presented in Table 4.2 demonstrate values of $\bar{x}$ derived from images processed using radiometric truth estimates which are inferior to those measured for methods COE, SDE, and LPBII for a given antenna pattern correction method. A possible source of error for the measurement of the radiometric truth values exists due to the smallest measurement interval. This was one frequency sample for the measurement of radiometric truth. Thus, the measurements are accurate to the one half of a frequency sample, or 13 Hz.

The results presented in Table 4.2 indicate that images processed using LPBII were found to have an overall azimuth scalloping measure that was less than those processed using COE or SDE, for each antenna pattern correction scenario. This is largely due to the fact that the perfor-

mance of method LPBII does not rely on the validity of assumptions ***A1*** and ***A2***, as do the other performance methods. This result was predicted in section 3.2.3.

Among the methods for antenna pattern correction, the overall azimuth scalloping measure was found to decrease significantly for the correction methods employing 2 looks, relative to the one look scenario, for all estimation methods. However, there was little distinction between the performance of the CSNR method and that of the IBP method according to practical results, as opposed to the scenario predicted by the simulation results of Section 2.3.2. The following paragraph relates these results to the ideal case simulation results of Section 2.3.2.

Section 2.3.2 of this thesis presented an analysis of the sensitivity of residual scalloping with Doppler centroid estimation error, for various antenna pattern correction scenarios. The plots appearing in Appendix D summarized the findings of this study. The results derived in this section can be compared to the set of simulation results as presented for the ENVISAT case from Appendix D, for the three antenna pattern correction schemes evaluated in this chapter. This comparison plot appears below. Also included in this plot are the scalloping measures derived for the images processed with the radiometric truth set of estimates.

The Doppler centroid estimation error figures appearing in Table 4.2 were calculated for each estimator COE, SDE, and LPBII, in order to situate specific $\bar{x}$ points on the plot. This was calculated, by simply summing the absolute distance of each estimation point to the radiometric truth value (using the results measured in Section 4.2.3), and dividing by the number of points in the summation.

Figure 4.12 Comparison of the results of the Netherlands Scene simulations with the predicted performance of antenna pattern correction methods.

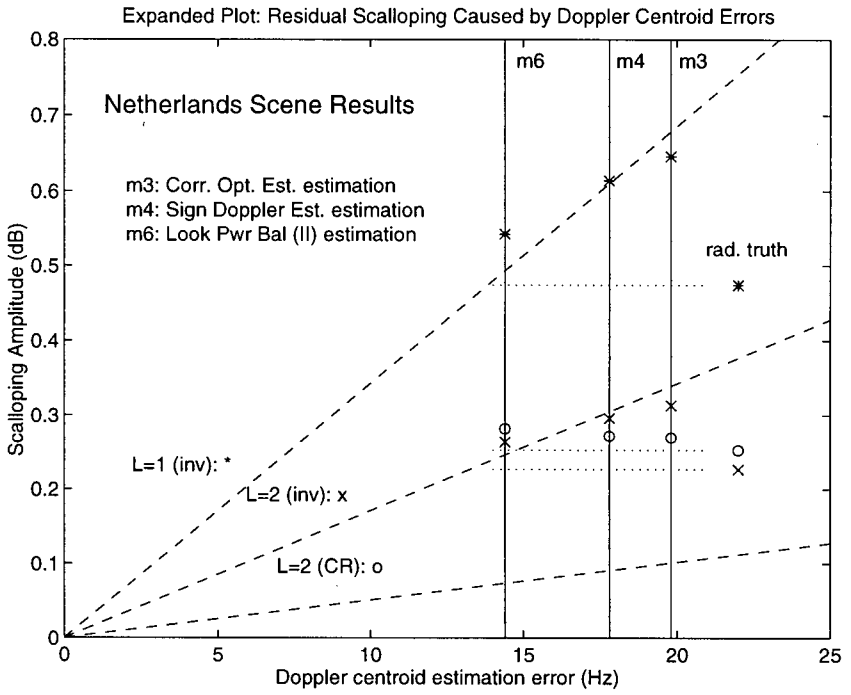

Observing the graph of Figure 4.12, the results of this study show a fair degree of correlation overall to those results measured in Section 2.3.2. The following development relates the reduction of scalloping performance of the antenna pattern correction methods to the equivalent number of looks achieved in the implementation of each method over azimuth.

The amount of scalloping is reduced when employing an increasing number of looks for antenna pattern correction. The performance of both methods for antenna pattern correction with respect to the equivalent number of looks can be described with respect to Figure 4.13.

Figure 4.13 Illustration of the Equivalent Number of Looks achieved by the Antenna Pattern Correction Methods for various multilook implementations.

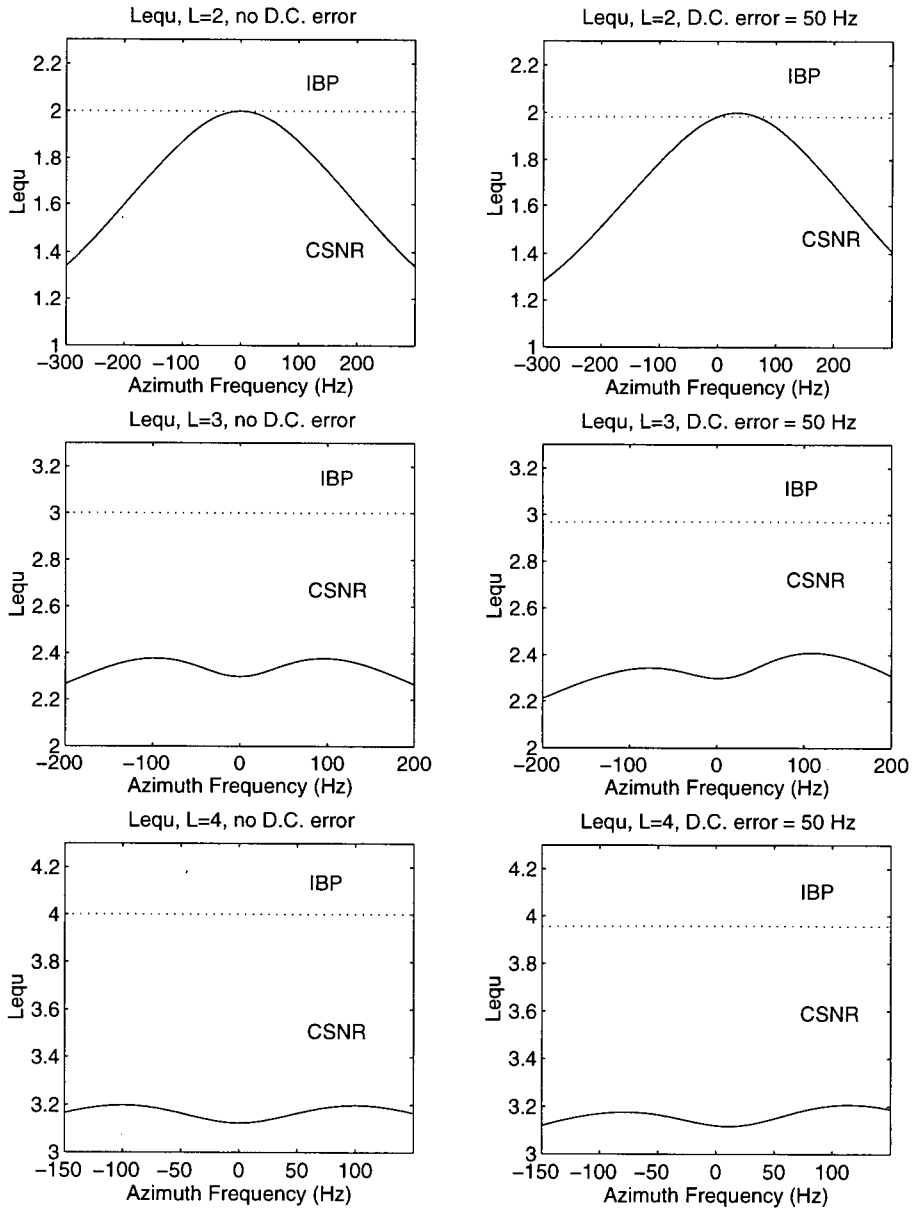

Figure 4.13 presents a set of plots for the equivalent number of looks over azimuth for both the Inverse Beam Pattern Method (IBP) and the Constant SNR Method (CSNR). The first set of plots (the top two figures) demonstrates the 2 look simulation results. The 3 and 4 look simulation results are presented in the lower two sets of plots. For each set of plots, the left plot

illustrates the case of zero Doppler centroid estimation error, and the right plot illustrates a 50 Hz Doppler centroid estimation error. These simulation results were carried out using the parameters presented in Section 2.3 for the ENVISAT ScanSAR case, using equation 26 to derive the equivalent number of looks (Lequ). In all cases, the signal level for the implementation of the CSNR method was chosen so as to minimize the residual scalloping over azimuth.

The following results are derived with respect to Figure 4.13. Consider first the performance of the CSNR method. For each of the multilook simulation results, the Lequ is not constant over azimuth. In addition, as the number of looks increases, Lequ deviates further from the nominal number of looks in the implementation. Thus, it appears that the CSNR method does not maximally employ the input looks over azimuth. Conversely, the IBP method consistently shows a maximization of Lequ over azimuth for each multilook implementation. The significance of this result is not known at this point. However, it is possible that the amount of scalloping is increased using the CSNR method for this reason in practice, when compared to the simulation results for the 2 look implementation. This may also explain the fact that there is little distinction between the practical performance of the CSNR method and the IBP method for the 2 look implementation.

In addition, the performance of the CSNR method may be more sensitive than that of the IBP method with respect to the equivalent number of looks achieved over azimuth. This may be because the CSNR method generates weighting functions which de-emphasize the outer looks. Conversely, the weighting functions derived using the IBP method emphasize the outer looks to equalize the power, thereby maximizing the equivalent number of looks.

Thus, the CSNR functions derived to minimize the residual scalloping result in an equiva-

lent number of looks which is not maximized over azimuth. This may explain the fact that there appears to be little distinction between the practical performance of scalloping reduction of the CSNR method and the IBP method for the 2 look implementation. Further sources of discrepancy can be attributed to residual spectral variance resulting from non-uniform scene reflectivity, speckle and ambiguity noise, and antenna pattern modelling.

(ii) Squamish Scene Simulation Results

Appendix I contains the results of applying methods COE, SDE, and LPBII to process the Squamish Scene data image. These results are organized and presented in this appendix and summarized in Table 4.3 in the same manner as that described for the Netherlands scene results.

The overall azimuth scalloping measures as derived from images processed using the radiometric truth set of estimations (for the Squamish Scene, in Table 4.3) are once again tabulated for reference. These values are found to be lower in most cases than those measured for methods COE, SDE, and LPBII for a given antenna pattern correction scenario.

Regarding the correlation of regions of samples showing high scene contrast levels to the measured quantities of azimuth scalloping over each range subswath, there were no groups of data samples averaged over which the performance of estimators COE, SDE, and LPBII (for the IBP, 1 look scenario) demonstrated consistently poor estimation results. In addition, the overall azimuth scalloping measures, as summarized in Table 4.3, are consistently lower in value than those measured for the Netherlands Scene. This once again leads to the assumption that the scene reflectivity of the Squamish scene has remained more uniform (e.g. the variance has remained more constant over the scene area) and the complex scene reflectivity of this Squamish Scene is likely more accurately modelled as a Gaussian distributed process of zero mean (assumption ***A2***

of section 3.2.1) than that of the Netherlands Scene, due to the absence of land-sea boundaries in the Squamish Scene.

Table 4.3 Overall Azimuth Scalloping Measures (dB), Squamish Scene

	A.P.C. Methods			D.C.Est. Error
estimator	IBP, 1L	IBP, 2L	CR, 2L	(Hz)
COE	0.24	0.12	0.17	10.4
SDE	0.31	0.17	0.17	10.3
LPBII	0.25	0.16	0.13	9.3
rad. truth	0.26	0.14	0.12	-

With reference to the relative performance of each estimator for the IBP, 1 look scenario, the image processed using SDE demonstrated more residual scalloping than those processed using COE or LPBII. This is expected due to the predicted sensitivity of the Sign Doppler Estimator (SDE) method for Doppler centroid estimation (and the resulting presence of residual scalloping) to high contrast scenes. Regarding the performance of the antenna pattern correction methods, the 2 look methods were found to outperform the 1 look method once again in minimizing $\bar{x}$, for all estimation methods. However, overall distinction in performance between the IBP and CSNR 2 look methods was again found to be negligible as a result of measurements with this data set. In fact, the CSNR method results tend to approach those of the IBP method for the two look implementation. As presented earlier in this section, this is likely due to the fact that the scalloping is not maximally reduced for a given number of input looks using the CSNR method.

Figure 4.14 presents a comparison of the $\bar{x}$ values generated from this study and the antenna pattern correction method simulation results (as derived using ENVISAT parameters).

The two sets of data appear to show a low degree of correlation, when compared to that observed in the case of the Netherlands Scene data set results. Possible sources of discrepancy may be attributed to residual spectral variance resulting from non-uniform scene reflectivity, speckle and ambiguity noise, and antenna pattern modelling.

Figure 4.14 Comparison of the results of the Squamish Scene simulations with the predicted performance of antenna pattern correction methods

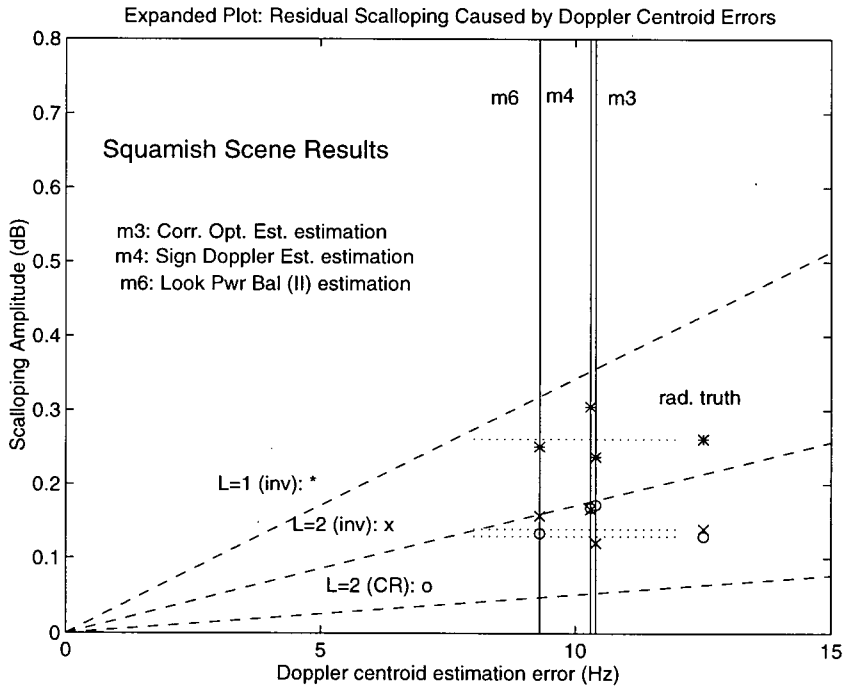

4.4 Computational Efficiency of Methods

This section presents a comparison of the computational efficiency of the Correlation with Optimal Estimator, Sign-Doppler Estimator and Look Power Balancing methods for Doppler centroid estimation.

The following assumptions are implicit in this analysis:

- one complex addition requires 2 FLOPS (floating point operations)
- one complex multiplication requires 6 FLOPS
- one real multiplication requires 1 FLOP
- one real addition requires 1 FLOP
- one Fast Fourier Transform requires $5N\log_2 N$ FLOPS, where N = # of FFT samples
- one sign comparison requires 2 FLOPS
- one detection of a complex number (2 real multiplications + 1 real addition) requires 5 FLOPS
- one logarithm operation requires 7 FLOPS

Each estimation method will be compared based on the number of FLOPS required for the calculation of an estimation point over one range subswath containing 12 bursts of length 64 azimuth samples (N = 64), averaged over 200 range samples. This is assumed to be a typical scenario for ScanSAR Doppler centroid estimation.

(i) Correlation with Optimal Estimation Method

The calculation of the 64-point FFTs involved in the 12 bursts, each averaged over 200 rangelines involves $C1$ FLOPS, where

$$C1 = 12 \cdot 200 \cdot 5N\log_2 N = 4.608e6. \quad \text{(EQ 59)}$$

The detection of the above outputs requires $C2$ FLOPS, where

$$C2 = 12 \cdot 200 \cdot N \cdot 1 \text{ detection} = 768e3 . \quad \text{(EQ 60)}$$

Summation of the above lines for averaging $C3$ FLOPS, where

$$C3 = 12 \cdot 200 \cdot N \cdot 1 \text{ real addition} = 153.6e3. \quad \text{(EQ 61)}$$

Finally, the correlation operation requires $C4$ FLOPS, where

$$C4 = N \cdot 2 \cdot N \cdot (1 \text{ real addition} + 1 \text{ real multiplication}) = 16.4e3 \quad \text{(EQ 62)}$$

The contributions of the other processing calculations to the final estimate are assumed negligible. Thus, summing the above values yields a total of

$$C1 + C2 + C3 + C4 = 5.546e6 \text{ FLOPS} \quad \text{(EQ 63)}$$

for the Correlation with Optimal Estimator Method for Doppler centroid estimation.

(ii) Sign-Doppler Estimator Method

The calculation of each of 4 sign correlation values yields

$$4\,[\,(200 \cdot 64 \cdot 1 \text{ real multiplication} + 1 \text{ sign comparison}) + 1 \text{ detection of size N}] \quad \text{(EQ 64)}$$

which calculates to 52.5e3 FLOPS per burst. Over 12 bursts, this comes to 0.629e6 FLOPS in total, where the calculations involved in deriving the correlation coefficients are assumed negligeable in comparison to those operations carried out in the processing loop.

(iii) Look-Power Balancing Method

The operations involved for the processing, detection, and averaging of two looks can be calculated as $C5$ FLOPS, where

$$C5 = 2 \text{ looks} \cdot (C1 + C2 + C3) = 11.06e6 \quad \text{(EQ 65)}$$

and $C1$, $C2$, and $C3$ were presented in equations 57, 58, and 59. The weighing of the looks, ratio division of looks, and logarithm operations are estimated to require $C6$ FLOPS, where

$$C6 = 12 \cdot 200 \cdot (1 \text{ real multiplication} + 1 \text{ real multiplication} + 1 \text{ logarithm}) = 21.6e3 \quad \text{(EQ 66)}$$

It is assumed that the calculation of the template functions is not implemented as a real time

operation, and the comparison of the averaged look-ratio quantity to the set of template functions requires a negligible amount of operations compared to those included above. Then, it is found that the Look Power Balancing Method for Doppler centroid estimation requires C5 + C6 = 11.08e6 FLOPS in total.

The following table summarizes the findings of this section. For an illustrative comparison of the relative computational efficiency of each method, the quantities from column 1 are presented in column 2, normalized to the amount of FLOPS required for the Correlation with Optimal Estimation Method.

Table 4.4 Summary of Computational Efficiency Requirements

method	FLOPS	approximate normalization
COE	5.546 e6	1.00
SDE	0.629 e6	0.11
LPBII	11.08 e6	2.00

The Sign-Doppler Method operates with roughly 11% of the computational requirements of the Correlation with Optimal Estimator Method, while the Look Power Balancing requires roughly double the operations. A sensitivity analysis was carried out using various numbers of bursts, burst sizes, and numbers of range samples to constitute different parameter sets representing other possible ScanSAR scenarios. The results shown in Table 4.4 were found to be representative for all of the ScanSAR scenarios examined. Note that for increasing burst sizes, the efficiency rate of the Sign Doppler Estimator compared with the other two methods was found to increase. This is expected, as the Sign Doppler Estimator does not use FFT operations, which

become computationally expensive with increasing burst sizes. It is important to recognize that while these relative measures would have proved to be more significant years ago, the technological advancements of carrying out fast digital signal processing operations such as FFT's in real time using relatively inexpensive hardware have greatly lessened the significance of comparing the above methods based on this criteria.

4.5 Summary of Results

The aim of this chapter was to evaluate the *relative* performance of certain methods for the improvement of radiometric image quality. Thus, in the interpretation of the results generated, conclusions will be formed based on trends apparent in the results, rather than on the absolute numerical quantities derived from each investigation. Further testing involving more data of various contrast levels would constitute a more reliable pool of results from which numerical values could be assigned to each estimator and antenna pattern correction scheme with a higher degree of confidence.

Based on the observations noted in Sections 4.2.3 and 4.3.3, the performance of each of the selected methods for Doppler centroid estimation was found to be sensitive to scene contrast and to the presence of land-sea boundaries. However, the Look Power Balancing (II) Method was found to show a superior degree of tolerance to such scene feature variations relative to the other methods tested. As a result, the Doppler centroid estimations derived using this method were found to be the most accurate over areas of high scene contrast and for areas containing land-sea boundaries. As predicted in section 3.2.3, this is largely due to the fact that the accuracy of the LPB method does not rely on the validity of assumptions related to scene reflectivity and/or the distribution of individual scatterers (***A1*** and ***A2***, from Section 3.2.1), whereas all other methods

do. This is also in accordance with the result reported by Jin, who in [34] quotes the performance of this method to be superior to that of the Correlation with Optimal Estimator method, with the generated estimation errors similarly ranging from 9.5 Hz to 12 Hz over mountainous terrain.

The performance of the Look Power Balancing Method for Doppler centroid estimation was found to be sensitive to antenna pattern modelling. This result is in agreement with the prediction of Section 3.2.3, as drawn from the assumption that the performance accuracy of the LPB is based on the knowledge of an accurate model of the azimuth antenna pattern model (assumption ***A3*** from Section 3.2.3). This conclusion is also in agreement with the results of simulation carried out by Mittermayer et al. in [40].

Implementing an antenna pattern correction scheme with 2 looks as opposed to one look was found to yield output images of improved radiometric image quality. This result supports the conclusions drawn based on the ideal scenario simulations found in Section 2.3. In addition, the IBP method consistently showed a maximization of the equivalent number of looks over azimuth. Conversely, the CSNR functions derived to minimize the residual scalloping resulted in an equivalent number of looks which was not maximized over azimuth. It is possible that the amount of scalloping was increased using the CSNR method for this reason in practice, when compared to the simulation results for the 2 look implementation. As a result, there appeared to be little distinction between the practical performance of scalloping reduction of the CSNR and IBP methods for the 2 look implementation.

Chapter 5 Conclusions

5.1 Summary

This thesis was concerned with improving the radiometric image quality in azimuth of remote sensing images processed using ENVISAT ScanSAR satellite data. Although several authors have investigated Doppler centroid estimation techniques for the case of continuous-mode data processing, there have been relatively few contributions to the problem of Doppler centroid estimation for ScanSAR data. In addition, this thesis presents a novel evaluation of the performance of two selected antenna pattern correction methods for ScanSAR data in the presence of Doppler centroid estimation errors

Images generated from burst-mode SAR data (e.g. ENVISAT ScanSAR data) exhibit a radiometric 'banding' pattern because a time-varying portion of the return energy from each scatterer is captured by the imaging system. This variable portion of the return energy becomes modulated in azimuth according to a portion of the receiver antenna gain pattern, resulting in the periodic 'banding' effect of image intensity, known as scalloping. The focus of this thesis was the investigation of a radiometric image quality improvement scheme based on an accurate estimation of the Doppler centroid for ENVISAT ScanSAR data which reduces the output radiometric scalloping in azimuth to a level below which it is visibly undetectable (0.2 dB).

One way to correct for azimuth scalloping in ScanSAR data involves applying weighting functions to the azimuth processed data which are inversely related to the expected scalloping pattern. However, an inaccurate estimation of the Doppler centroid of the frequency spectrum of azimuth data leads to a misapplication of the antenna beam correction pattern functions, resulting in residual scalloping over azimuth. In addition, the amount of speckle reduction obtained by a

weighted multilook process can be described by the equivalent number of looks. The optimal set of weighting functions can be selected so as to satisfy a criterion which involves reducing the amount of residual scalloping and/or maximizing the achieved equivalent number of looks.

This thesis has presented the work done in quantifying the performance of both the Inverse Beam Pattern Method (IBP) and the Constant SNR Method (CSNR) for antenna pattern correction for a simulated case of ENVISAT ScanSAR data. As well, an investigation of the practical performance of the IBP and CSNR methods for antenna pattern correction for the 2 look implementation was presented.

By varying a design parameter in the derivation of the CSNR weighting functions, these functions can be customized to meet certain requirements. Specifically, the sensitivity of residual scalloping to Doppler centroid estimation errors and the amount of achieved speckle reduction are the two design criteria to consider when setting the design parameter for the CSNR method. The CSNR method generates weighting functions which de-emphasize the outer looks. Conversely, the weighting functions derived using the IBP method emphasize the outer looks to equalize the power, thereby maximizing the equivalent number of looks.

The simulation results demonstrated that the weighting functions generated using the IBP method were found to maximize the equivalent number of looks over azimuth, but were more sensitive with respect to residual scalloping to Doppler centroid estimation errors. However, the weighting functions derived using the CSNR method resulted in an equivalent number of looks which varied over azimuth frequency, yet these functions showed less sensitivity with respect to residual scalloping to Doppler centroid estimation errors.

For the practical testing, the CSNR functions were designed so as to minimize the residual scalloping over azimuth. As the number of looks increased, the sensitivity of residual scalloping to Doppler centroid estimation errors was found to decrease for both methods. With respect to the CSNR method results, the amount of scalloping was increased in practice when compared to the results of simulation for the 2 look case. This may be due to the fact that the equivalent number of looks was not maximized over azimuth for the specific CSNR method implementation. As a result, there appeared to be little distinction between the practical performance of scalloping reduction of the CSNR and IBP methods for the 2 look implementation.

Errors in the estimation of a Doppler centroid model used for the azimuth processing of ScanSAR data using the SPECAN algorithm will also introduce azimuth radiometric scalloping in the output image. Several methods for Doppler centroid estimation were implemented and the relative performance of each method was quantified using simulations with ERS-1 SAR data. Certain assumptions implicit for the ideal performance of each estimator were explained, and the relative performance of the methods for certain estimation scenarios was predicted accordingly. The estimators were then compared on the basis of the measured RMS deviation errors and residual scalloping present in the images processed using each method. The following paragraphs summarize the results of these investigations.

The performance of each of the selected methods for Doppler centroid estimation was found to be sensitive to scene contrast and to the presence of land-sea boundaries in the scene. However, the Doppler centroid estimations derived using the Look Power Balancing Method were found to be the most accurate over image areas of high scene contrast and for areas containing land-water boundaries. This is largely due to the fact that, contrary to the other methods

tested, the accuracy of the Look Power Balancing Method does not rely on the validity of assumptions related to scene reflectivity and/or the distribution of individual scatterers. In addition, the performance of the Look Power Balancing Method for Doppler centroid estimation was found to be sensitive to antenna pattern modelling.

5.2 Future Work

The effectiveness of the radiometric correction schemes discussed above should be tested with a larger set of scene data, comprising images of various scene content features and contrast levels. Further testing involving more data of various contrast levels would constitute a more reliable pool of results from which absolute ratings could be assigned to each estimator and antenna pattern correction scheme with a certain degree of confidence, to support the relative performance trends observed thus far.

With respect to those methods tested for antenna pattern correction, future work should include measuring the effect on radiometric speckle of an equivalent number of looks which varies over azimuth. In addition, testing should be carried out using sets of CSNR functions designed to satisfy different criteria involving residual scalloping reduction and/or speckle reduction in order to fully characterize the performance of the CSNR method with respect to the IBP method. An thorough analysis of the equivalent number of looks achieved by both methods in the presence of Doppler centroid estimation errors should also be investigated with respect to the effects on the amount of observed residual scalloping.

This thesis work was largely concerned with the evaluation of Doppler centroid estimation methods using data scenes of high contrast and containing land-sea boundaries. This is because certain assumptions for the ideal operation of the estimators are not valid using data with this type

of scene content. Generating accurate estimates is thus more challenging for the estimators. However, for the evaluation of antenna pattern correction schemes, it is useful to test with low contrast images since any residual scalloping resulting from an inaccurate antenna pattern correction implementation is more visible in scenes of low contrast than in those of high contrast. It would also prove worthwhile to investigate the trade-off of the gain in radiometric image quality achieved as a result of implementing more looks for antenna pattern correction versus the complexity of implementation and computational expense involved in implementing these methods in the ENVISAT ScanSAR system.

Bibliography

[1] C. Elachi. *Spaceborne Radar Remote Sensing: Applications and Techniques.* New York, N.Y. IEEE Press, 1987.

[2] K. Tomiyasu. "Conceptual performance of a satellite borne, wide swath synthetic aperture radar," IEEE Trans. on Geoscience and Remote Sensing vol.GE-19, pp. 108-116. Mar. 1995.

[3] K. Tomiyasu. "Tutorial Review of Synthetic Aperture Radar (SAR) with Applications to Imaging of the Ocean Surface," Proc. of the IEEE, vol 66 no 5, May 1978. pp. 563-583.

[4] I.G. Cumming, J.R. Bennett. "Digital Processing of Seasat SAR Data," International Conference on Acoustics, Speech and Signal Processing, Washington, D.C., 1979.

[5] J. P. Fitch. *Synthetic Aperture Radar*, New York. Springer-Verlag, 1988.

[6] MacDonald Dettwiler and Associates, Ltd., "Spectral analysis approach to the compression of linear FM signals," Tech. rep. TN-79-276-003, 1979.

[7] J.C. Curlander, R.N. McDonough. *Synthetic Aperture Radar: Systems and Signal Processing.* New York, John Wiley and Sons, Inc., 1991.

[8] R.K. Moore, J.P. Claassen, Y.H. Lin. "Scanning Spaceborne Synthetic Aperture Radar with Integrated Radiometer," IEEE Trans. Aerosp. and Elect. Systems, vol. AES-17, no. 3, May 1981. pp. 410-421.

[9] K. Eldhurset, P.A. Valand. "ScanSAR processing and simulation for ASAR using ERS-1 raw data," Int. J. Remote Sensing, vol 16 no 14, 1995, pp. 2657-2674.

[10] S. Ahmed, H.R. Warren, M.D. Symonds, R.P Cox. "The Radarsat System," IEEE Trans. Geosc. and Rem. Sens. vol. 28, no. 4, July 1990.

[11] S. Karnevi, E. Dean, D.J.Q. Carter, S.S. Hartley. "ENVISAT's Advanced Synthetic Aperture Radar: ASAR," *ESA Bulletin*, November 1993, European Space Agency. pp. 30-35.

[12] R. Bamler."Optimum look weighting for burst-mode and ScanSAR processing," IEEE Trans. on Geoscience and Remote Sensing vol. 33 no.3, pp.722-725. May 1995.

[13] R.M. Wedding, J.R. Bennett, I.G. Cumming. "Algorithms for preprocessing of satellite SAR data," Proceedings of the ISPRS Commission II Symposium, Ottawa, Canada, 1982.

[14] I.G. Cumming, M. Sack, M.R. Ito. "Applications of efficient linear FM matched filtering algorithms to synthetic aperture radar processing," IEE Proceedings, 132 pt. F no. 1, February 1985.

[15] T. Ngo and C. Vigneron. *Project Report: UBC SQLP v.1.7.* Radar Remote Sensing Group, University of British Columbia, 1995.

[16] H. Hobooti. *Radiometric Correction in Range-SPECAN SAR Processing.* M.A.Sc. thesis, Dept. of Electrical Engineering, The University of British Columbia, September 1995.

[17] N. Levanon. *Radar Principles.* New York, John Wiley and Sons Inc., 1988.

[18] F.K. Li, D.N. Held, J.C. Curlander, C. Wu. "Doppler parameter estimation for spaceborne synthetic aperture radars," IEEE Trans. Geosc. Rem. Sens., vol 23, no 1, 1985, pp. 47-56.

[19] S.N. Madsen. "Estimating the Doppler centroid of SAR data," IEEE Trans. Aerosp. Electron. Syst., vol 25, 1989, pp.134-140.

[20] F. Wong, G. Kuduvalli, I. Cumming, R. Slim. "On-Board Doppler Centroid Estimation," Tech. rep. OB-TN-50-7400, Macdonald Dettwiler and Associates, Ltd., January 1996.

[21] A. Papoulis. *Probability, Random Variables, and Stochastic Processes*, New York: McGraw-Hill, 1965, pp.197-198 and 483-485.

[22] H.A. Zebker, J. Villasenor. "Decorrelation in Interferometric Radar Echoes," IEEE Trans. on Geosc. and Remote Sensing , vol 30 no 5, September 1992. pp. 950-959.

[23] T. Ngo and C. Vigneron. *User Manual: UBC SQLP v.1.7.* Radar Remote Sensing Group, University of British Columbia, 1995.

[24] R. Bamler. "Doppler frequency estimation and the Cramer-Rao bound," IEEE Trans. Geosc. Rem. Sens. vol 29, no 3, May 1991, pp. 385-390.

[25] C.M. Vigneron, M. Goulding, I.G. Cumming, P. Lim. "Radiometric Effects of Doppler Centroid Estimation Error in ENVISAT ScanSAR Data," Tech. rep. PO-MDA-GS-2043 50-7430. Macdonald Dettwiler and Associates, Ltd., February 1996.

[26] G.W. Davidson. *Image Formation from Squint-Mode Synthetic Aperture Radar.* PhD thesis, Dept. of Electrical Engineering, The University of British Columbia, September 1994.

[27] I. Cumming, P. Kavanagh, M. Ito. "Resolving the Doppler Ambiguity for Spaceborne Synthetic Aperture Radar," Proc. IEEE IGARSS 1986, pp. 1639-1643.

[28] C.Y. Cheng and J. Curlander. "Doppler Centroid Estimation Ambiguity for Synthetic Aperture Radars," in Proc. IGARSS '89 Symp., pp. 2567-2571.

[29] R. Bamler and H. Runge. "PRF-ambiguity resolving by wavelength diversity," IEEE Trans. Geosc. Rem. Sens. vol 29 no 6, pp. 997-1003, Nov. 1991.

[30] F. Wong, I. Cumming. "A Combined SAR Doppler Estimation Scheme Based upon Signal Phase," IEEE Trans. Geosc. Rem. Sens., vol. 34 no. 3, May 1996. pp. 696-707.

[31] J.C. Curlander, C. Wu, A. Pang. "Automated preprocessing of spaceborne SAR data," in Proc. IGARSS '82 (Munich), pp. 3.1-3.6.

[32] E.A. Herland. "Seasat SAR processing at the Norweigian Defence Research Establishment," Proc. of an EARSeL-ESA Symp., Voss, Norway, May 19-20, 1981. pp.247-253.

[33] R.N. McDonough, B.E. Raff, J.L. Kerr. "Image formation from spaceborne synthetic aperture radar signals," Johns Hopkins APL Technical Digest, vol 6 no 4, 1985. pp. 300-312.

[34] M.Y. Jin. "Optimal Range and Doppler Centroid Estimation for a ScanSAR System," IEEE Trans. Geosc. Rem. Sens. vol 34 no 2, March 1996, pp. 479-488.

[35] M. Goulding. "Doppler Centroid Estimation by Use of a Look-Power Balancing Technique for the CDPF RSARP ScanSAR Processor," Technical Note, MacDonald Dettwiler and Associates Ltd., July 1995.

[36] **dtSAR source code**, MacDonald Dettwiler and Assoc. Ltd., 1994.

[37] H. Cramer. *Mathematical Methods of Statistics.* Princeton, N.J.: Princeton Univ. Press, 1946.

[38] A. P. Sage, J.L. Melsa. *Estimation Theory with Applications to Communications and Control.* New York: McGraw-Hill, 1981.

[39] S.L. Marple. *Digital Spectral Analysis.* Englewood Cliffs. N.J.: Prentice-Hall. 1987.

[40] J. Mittermayer, A. Moreira, G. Davidson, R. Bamler, Y.L. Desnos. " High Precision Processing of SIR-C ScanSAR Data," Technical Report - Deutsche Forschungsanstalt fur Luft-und Raumfarhrt (DLR) and European Space Agency (ESA-ESTEC), April, 1996.

[41] J. Siewerth. "Theory and Quantitative Comparison of Doppler Centroid Estimation Methods," in Proc. IGARSS '89, pp. 2576-2578.

[42] A. Moreira, R. Scheiber. "Doppler Parameters Estimation Algorithms for SAR Processing with the Chirp Scaling Approach," Proc. IGARSS '94, pp. 1977-1979.

[43] H. Richardson, G. Kuduvalli, I. Cumming, R. Slim. "Selection of On-Board Algorithms," Tech. rep. OBSP/TNT/0003/MDA, Macdonald Dettwiler and Associates, Ltd., December 1995.

[44] European Space Agency **internet hompepage**, http://services.esrin.esa.it/.

[45] M. Sack, M.R. Ito, I.G. Cumming. "Application of efficient linear FM matched filtering algorithms for synthetic aperture radar processing," IEEE Proceedings, vol 132, 1985, pp. 45-57.

[46] C. Chang, J.C. Curlander. "Algorithms to Resolve the Doppler Centroid Estimation Ambiguity for Synthetic Aperture Radar," IEEE Trans. on Geosc. Rem. Sens., 1992.

[47] Discussion with I.G. Cumming.

Appendix A: Determination of Signal Level for the Constant SNR Method, Case of L=2

This appendix presents a more complex derivation of the Constant SNR method look weighting filters which satisfies equations 18 to 20 from Chapter 2 over all x for the case of $L = 2$.

Consider the derived look filter functions from section 2.3.2, for $L = 2$:

$$W_1(x) = \frac{S - A_2(x)}{A_1(x) - A_2(x)} \quad \text{(EQ 67)}$$

$$W_2(x) = \frac{S - A_1(x)}{A_2(x) - A_1(x)}. \quad \text{(EQ 68)}$$

Inspection of equations 67 and 68 above reveals that for $A_1(x) = A_2(x)$ at $x = x_o$, the denominators of each of the functions are zeros for all S. Thus, $W_1(x_o)$ and $W_2(x_o)$ approach infinity and therefore the constraints of equations 18 to 20 are not satisfied at $x = x_o$. Thus, we need to find values $W_1(x)$ and $W_2(x)$ which do satisfy these constraints at $x = x_o$.

For $A_1(x) = A_2(x)$ at $x = x_o$, equations 18 and 19 can be rewritten as

$$A_1(x_o)\,[W_1(x_o) + W_2(x_o)] = S \quad \text{(EQ 69)}$$

$$W_1(x_o) + W_2(x_o) = 1. \quad \text{(EQ 70)}$$

Using equations 69 and 70 above yields a single value for S,

$$S = A_1(x_o) = A_2(x_o). \quad \text{(EQ 71)}$$

Inspection of equation 70 above reveals that there are an infinite number of combinations of

$W_1(x_o)$ and $W_2(x_o)$ for this solution. We further impose the constraint of equation 20 to determine one solution. This constraint can be rewritten for L=2 and $A_1(x_o) = A_2(x_o)$, as

$$min\left[W_1^2(x_o) + W_2^2(x_o)\right]. \quad \text{(EQ 72)}$$

Then, solving equations 70 and 72 yields the following solution at $x = x_o$.

$$W_1(x_o) = W_2(x_o) = 0.5 \quad \text{(EQ 73)}$$

Appendix B: Inverse Beam Pattern Method Results

This appendix presents a set of 6 plots outlining the simulation results of the Inverse Beam Pattern method for antenna pattern correction, as described in Section 2.3. In each set, the first and second plots illustrate the power of each burst image envelope and its corresponding look weighting function, over the defined period. Both the equivalent number of looks and the radiometric resolution are graphed in plots 3 and 4. Finally, plots 5 and 6 illustrate the noise signal level over azimuth and residual scalloping which results from a Doppler centroid error generating a minimum of 0.2 dB of residual scalloping, respectively.

Figure B.1 Inverse Beam Pattern Simulation Results: One Look Case

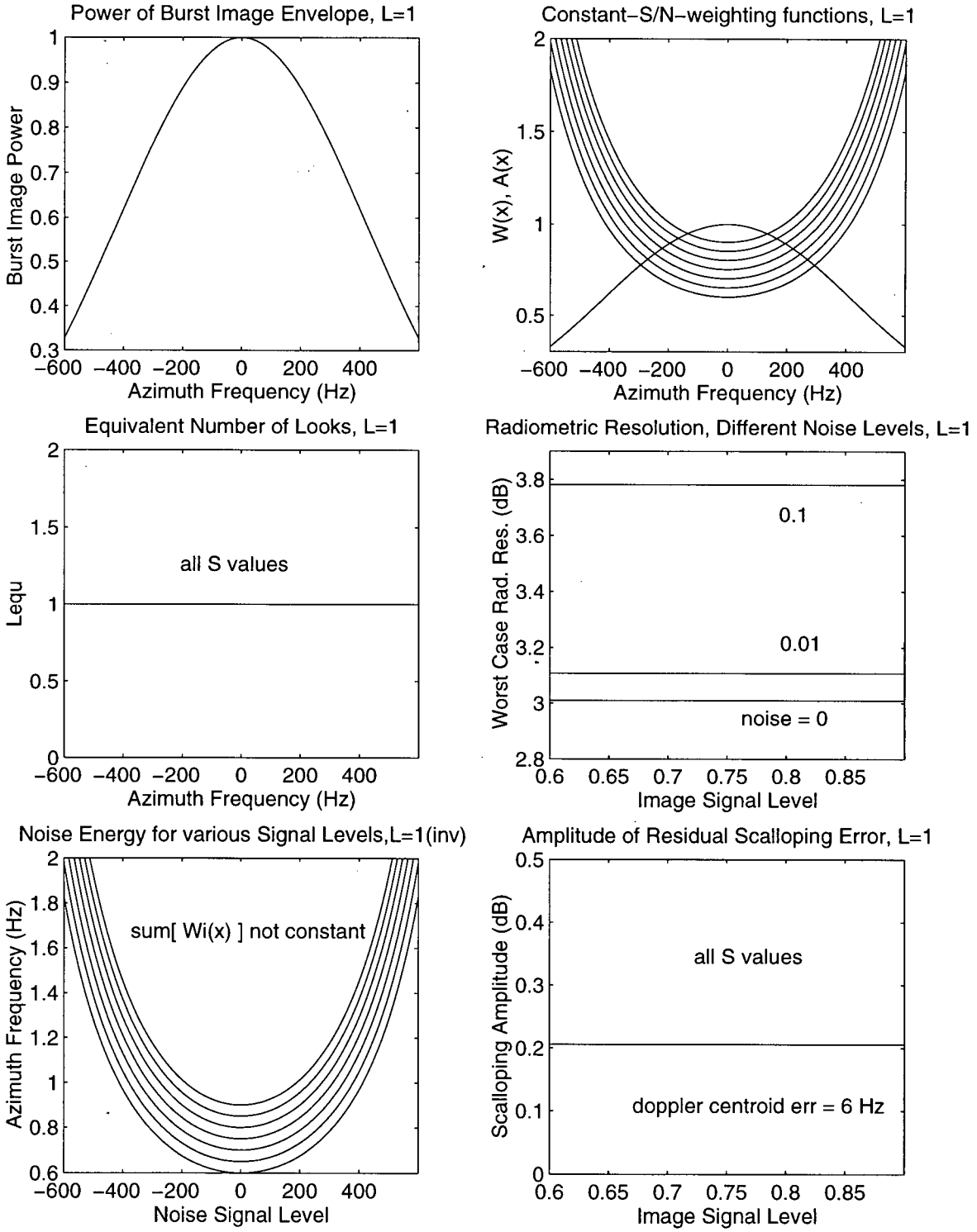

Figure B.2 Inverse Beam Pattern Simulation Results: Two Look Case

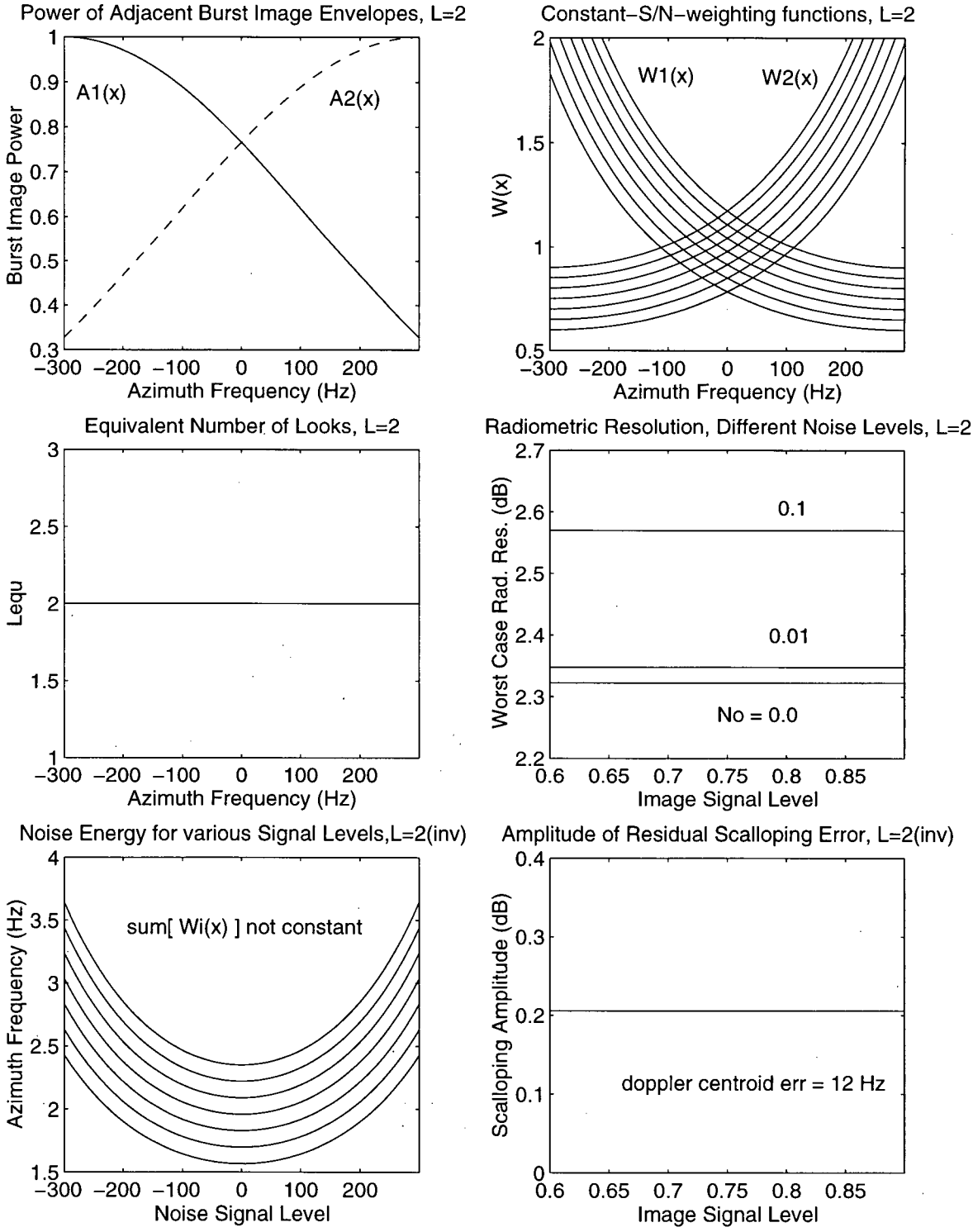

Figure B.3 Inverse Beam Pattern Simulation Results: Three Look Case

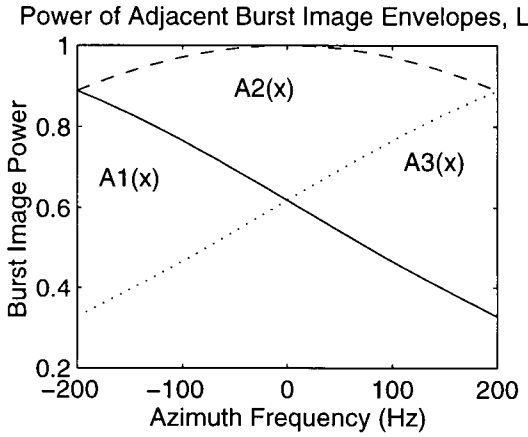

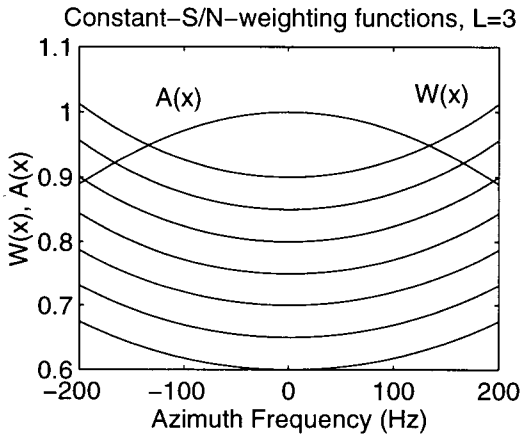

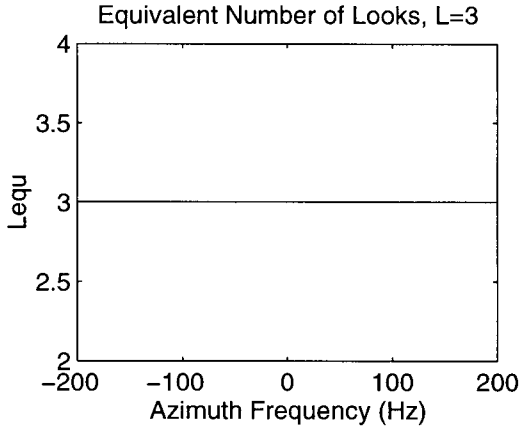

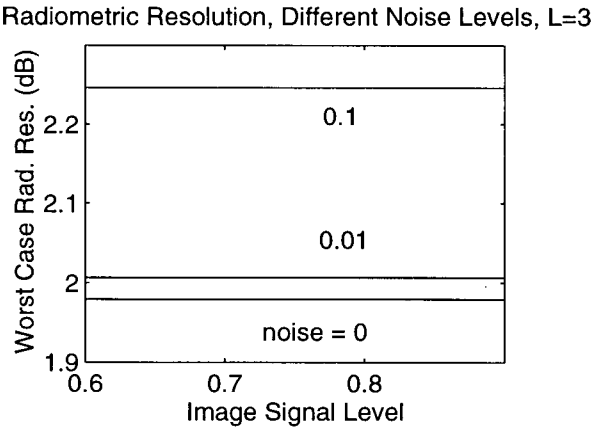

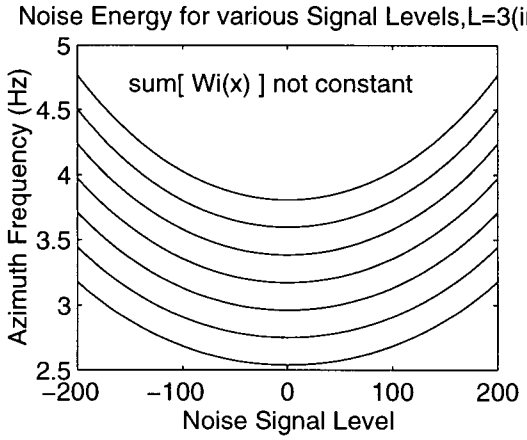

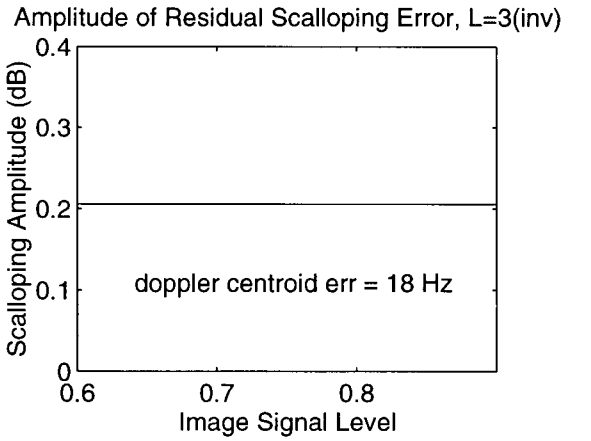

Figure B.4 Inverse Beam Pattern Simulation Results: Four Look Case

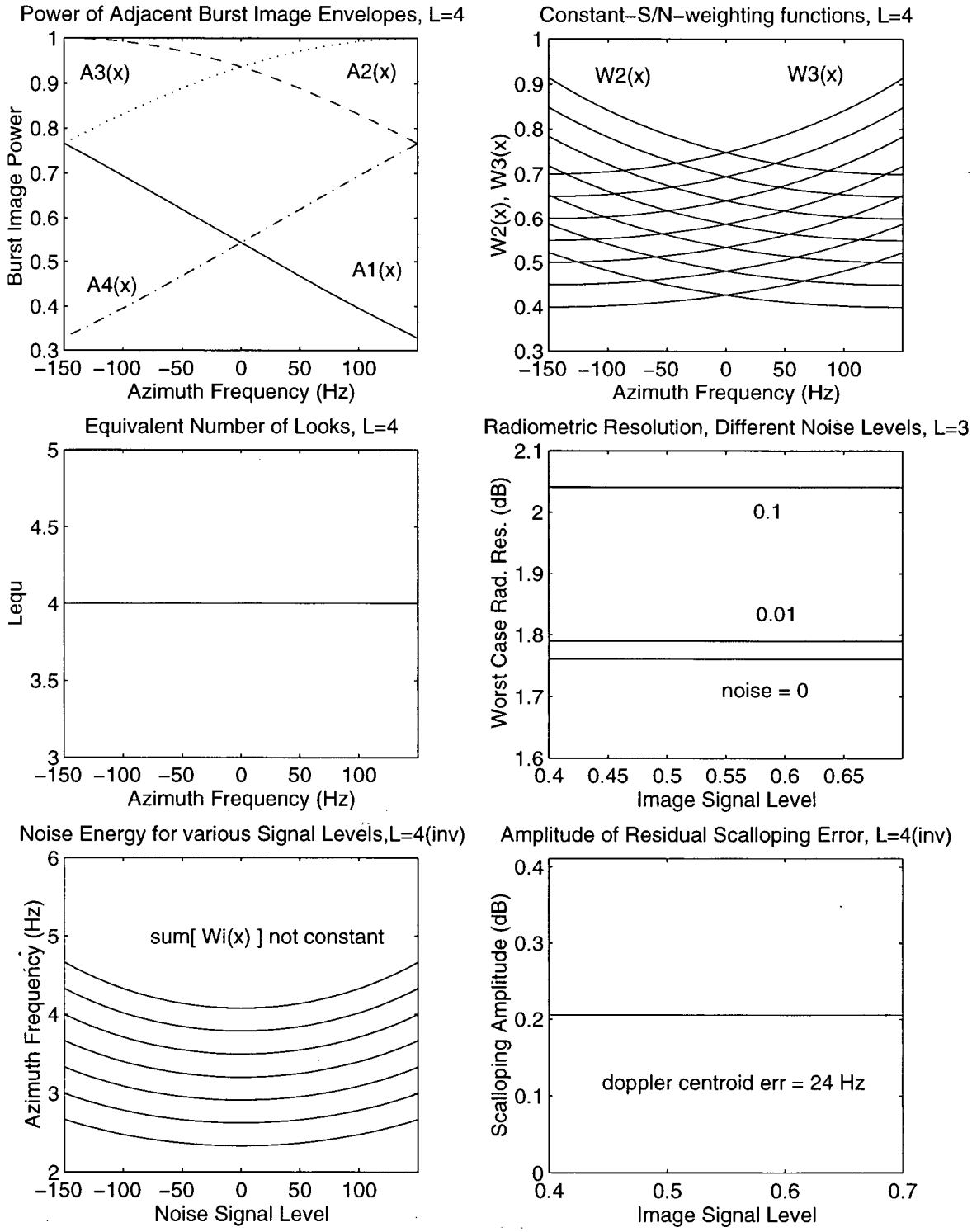

Appendix C: Constant SNR Method Results

This appendix presents a set of 6 plots outlining the simulation results of the Constant SNR method for antenna pattern correction, as described in Section 2.3. In each set, the first and second plots illustrate the power of each burst image envelope and its corresponding look weighting function, over the defined period. Both the equivalent number of looks and the radiometric resolution are graphed in plots 3 and 4. Finally, plots 5 and 6 illustrate the noise signal level over azimuth and residual scalloping which results from a Doppler centroid error generating a minimum of 0.2 dB of residual scalloping, respectively.

Figure C.1 Constant SNR Method Simulation Results: Two Look Case

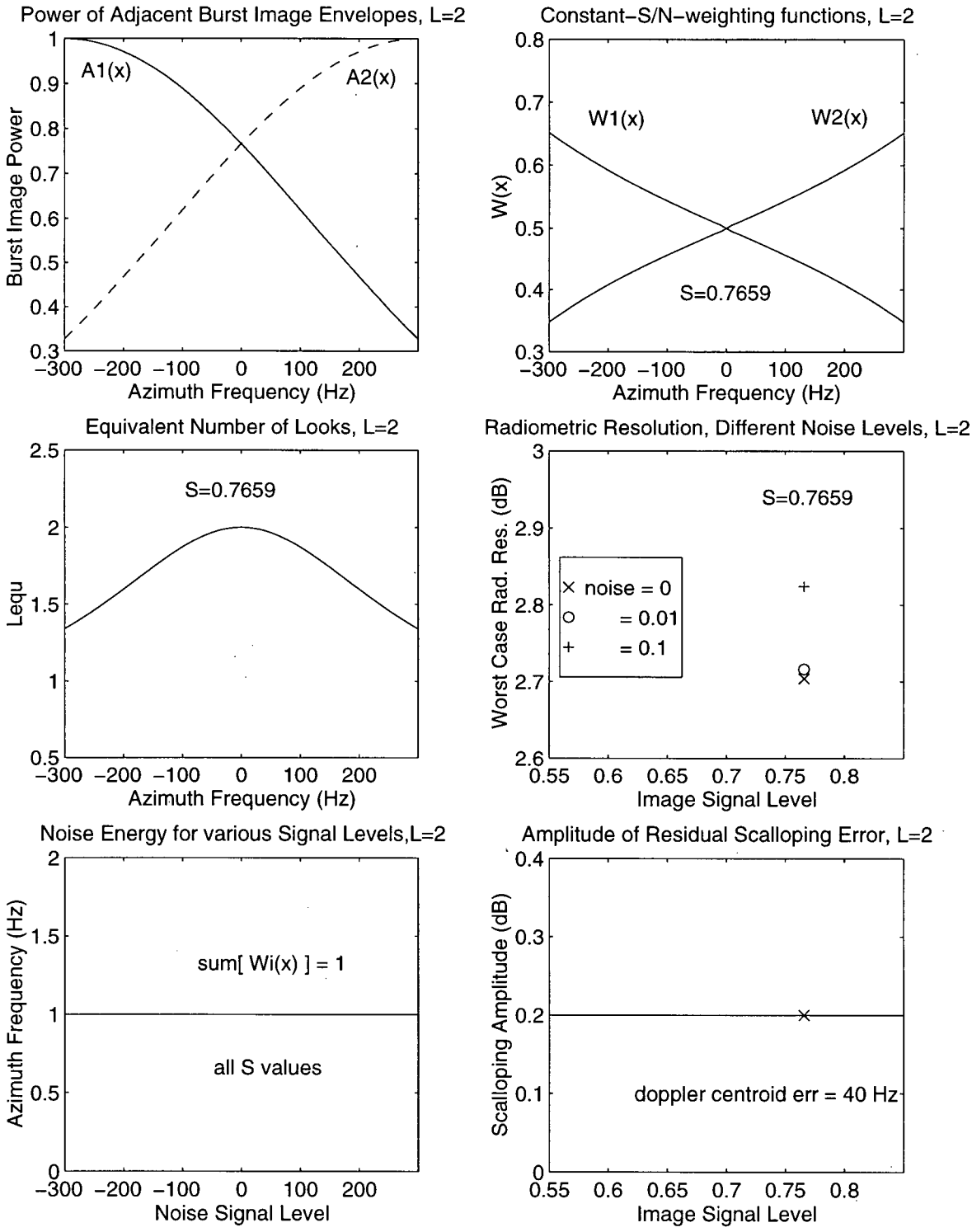

Figure C.2 Constant SNR Method Simulation Results: Three Look Case

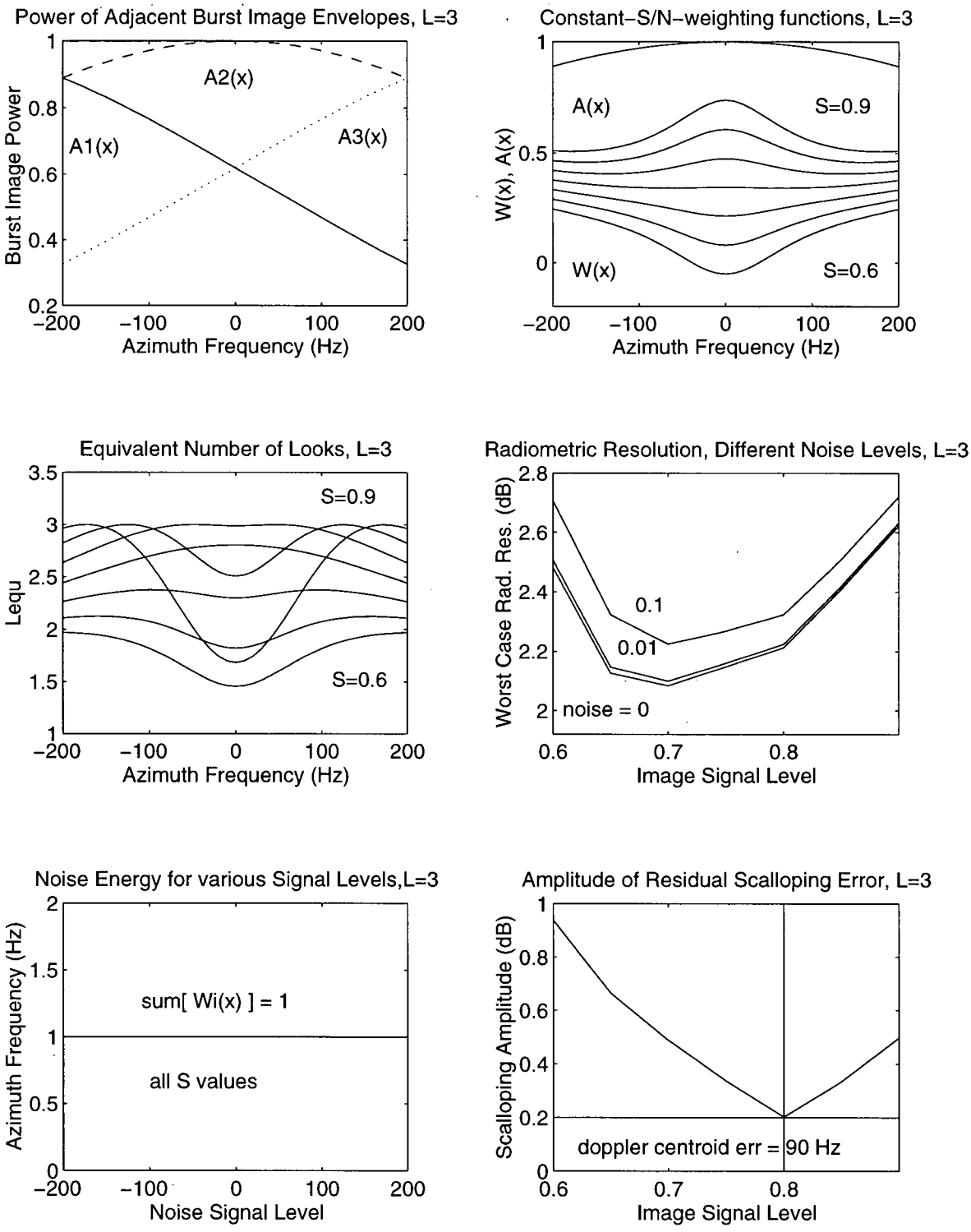

Figure C.3 Constant SNR Method Simulation Results: Four Look Case

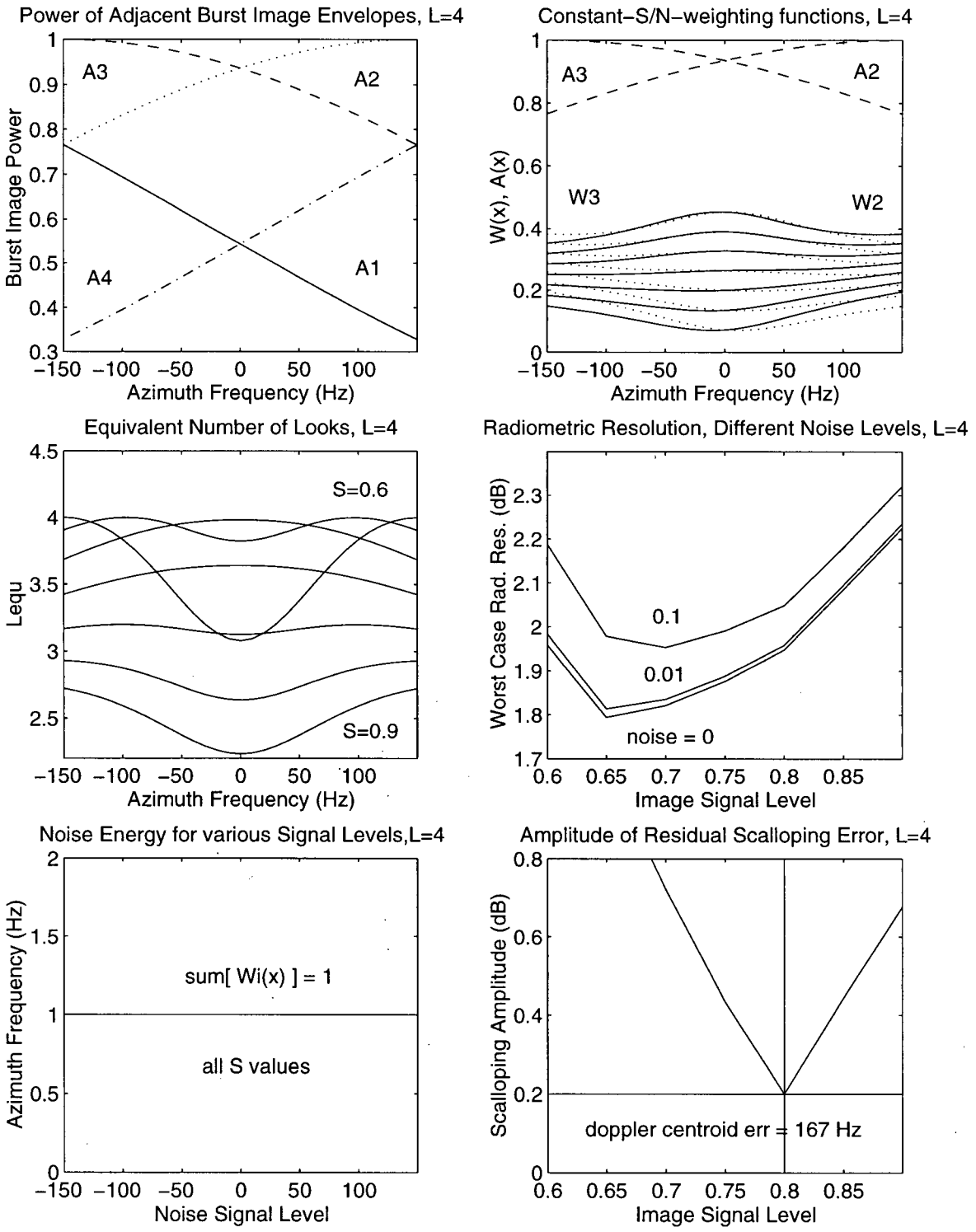

Appendix D: Doppler Centroid Estimation Error Sensitivity

This appendix presents simulation results describing the sensitivity of residual scalloping to Doppler centroid estimation errors, as measured for each antenna pattern correction method (please refer to Section 2.3.2 for more details).

Figure D.1 Residual Scalloping Caused by Doppler Centroid Errors

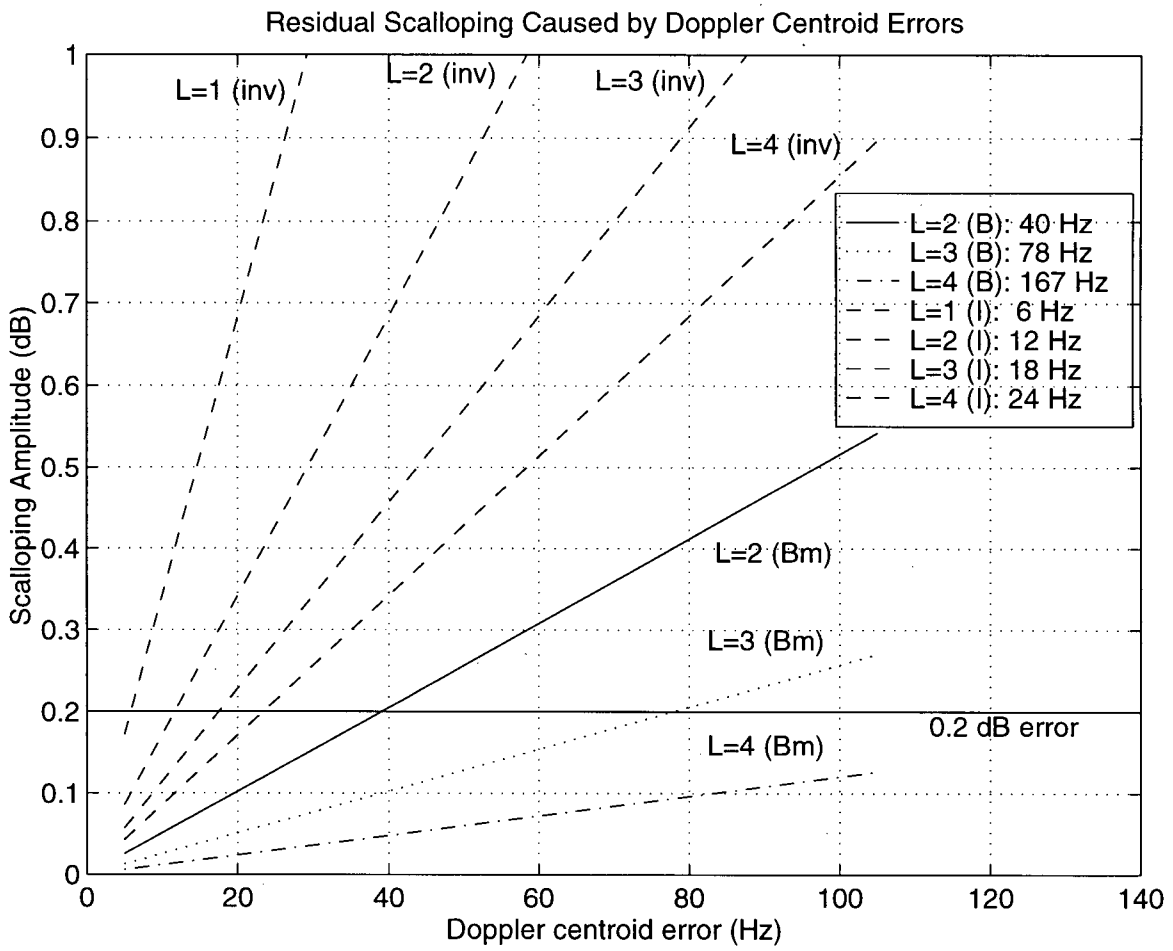

Figure D.2 Expanded Plot: Residual Scalloping Caused by Doppler Centroid Errors

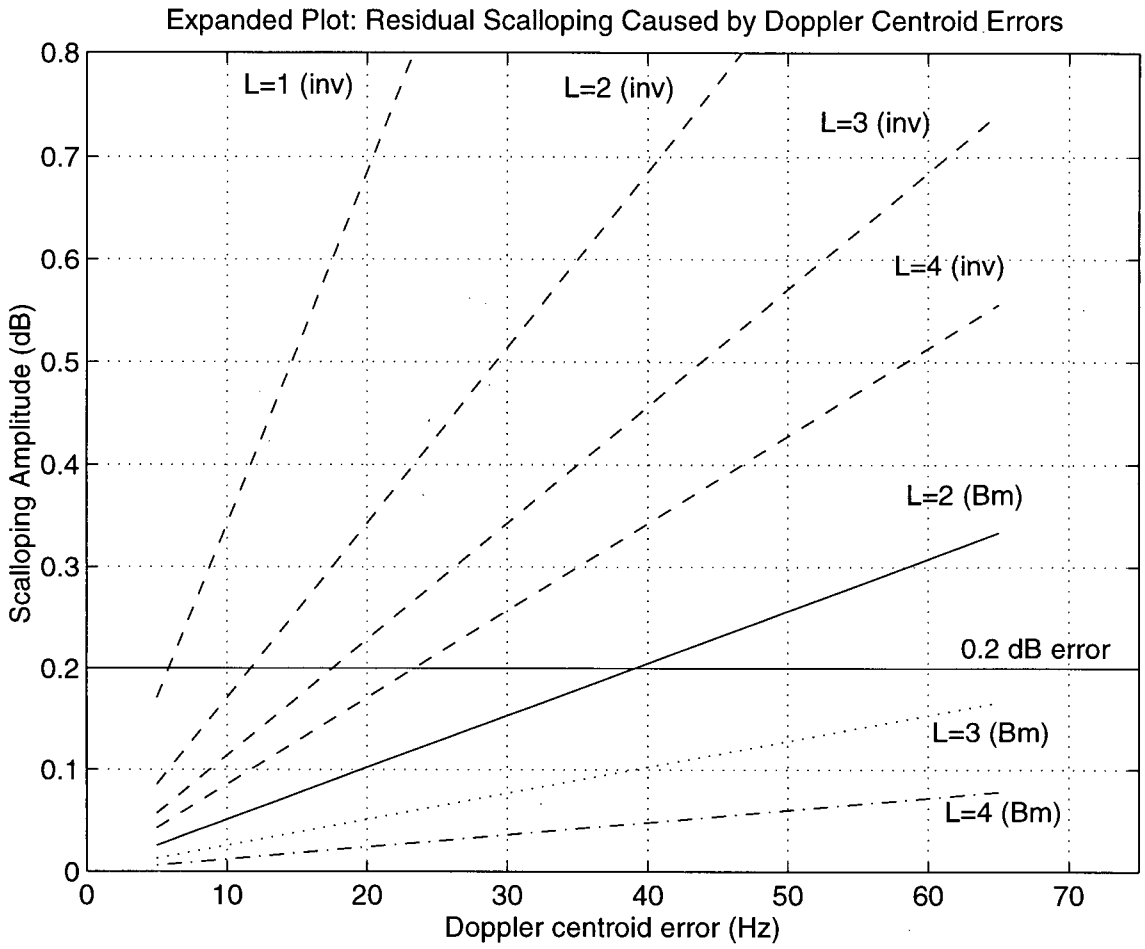

Appendix E: Residual Scalloping Illustration on a Low Contrast Scene

This appendix presents an example of a SAR image of low contrast which demonstrates residual scalloping due to burst mode data processing. A second image is included to illustrate the effects of residual scalloping correction for image quality improvement.

Figure E.1 Single look, low contrast scene (Chilcotin, ERS-1 data), 0 dB of residual scalloping.

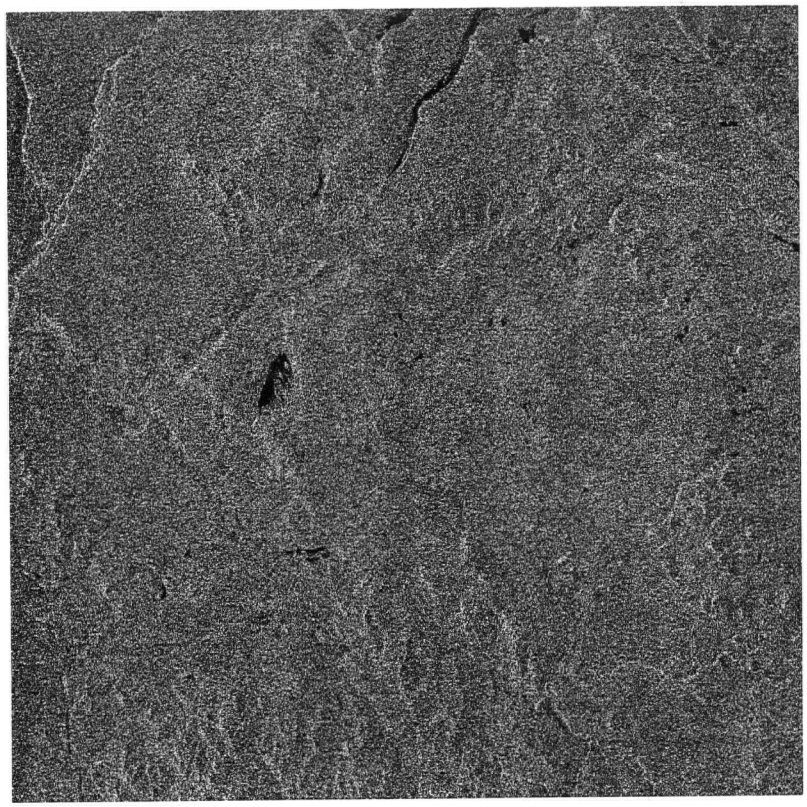

Figure E.2 Single look, low contrast image (Chilcotin, ERS-1 data), 2.5 of dB residual scalloping.

Appendix F: RMS Deviation of Doppler Centroid Estimates over Range: Netherlands Scene

This appendix presents the RMS Deviation testing results for the Netherlands Scene, for each Doppler centroid estimation method. These results are described in Section 4.2 of Chapter 4.

Figure F.1 Energy Balancing Method Results

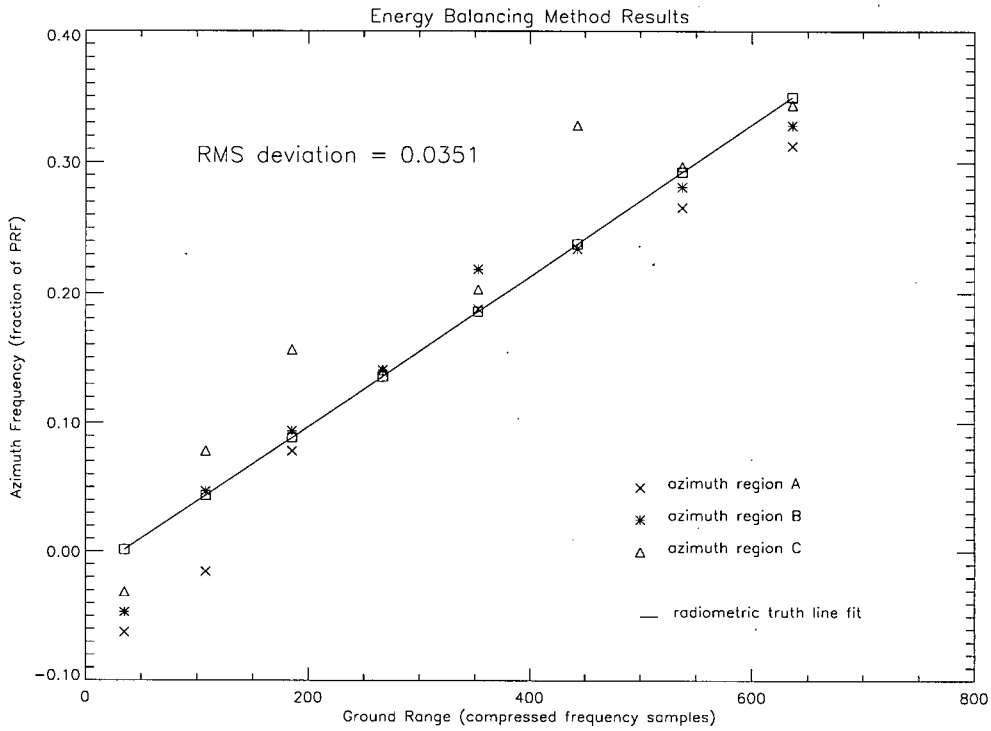

Figure F.2 Correlation with Nominal Spectrum Method Results

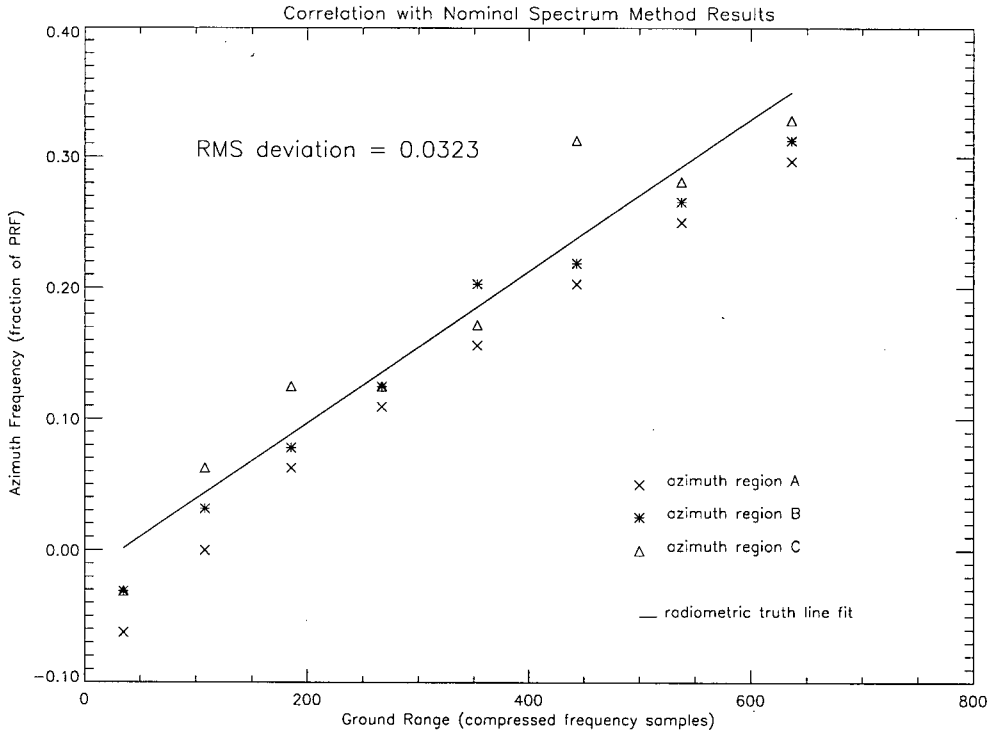

Figure F.3 Correlation with Optimal Estimator Method Results

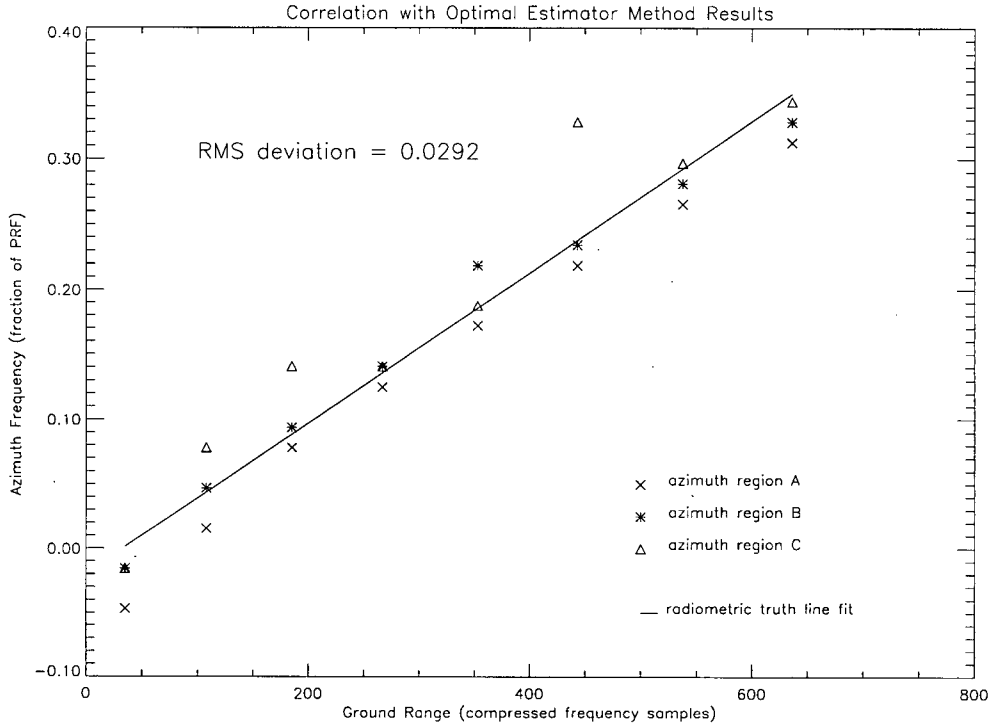

Figure F.4 Sign Doppler Estimator Results

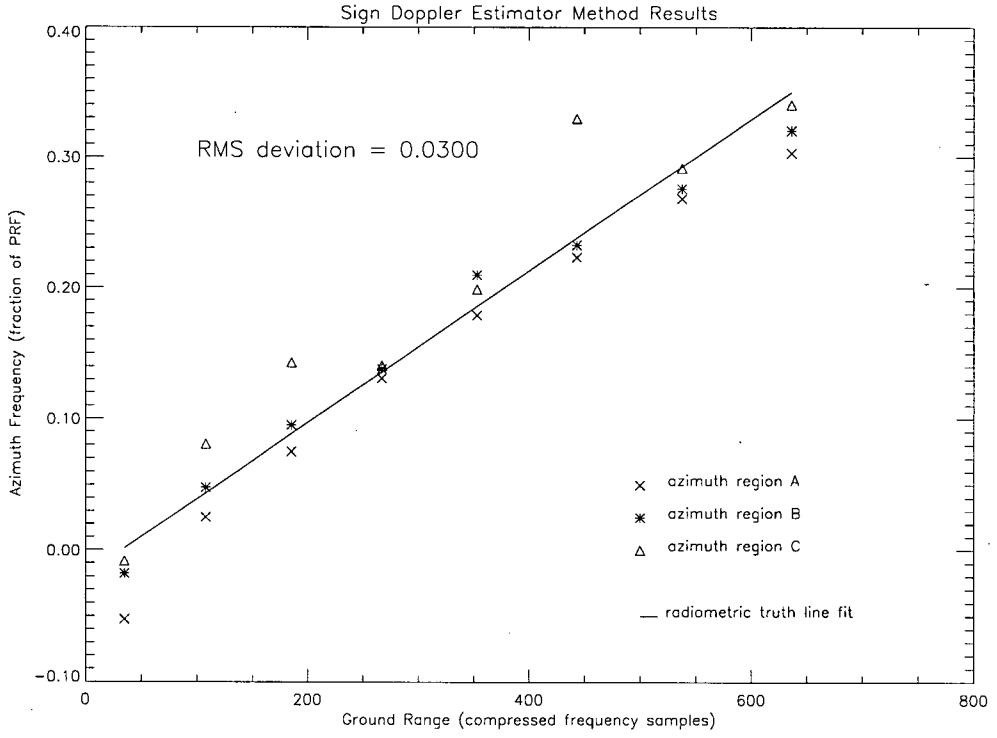

Figure F.5 Look-Power Balancing (I) Method Results

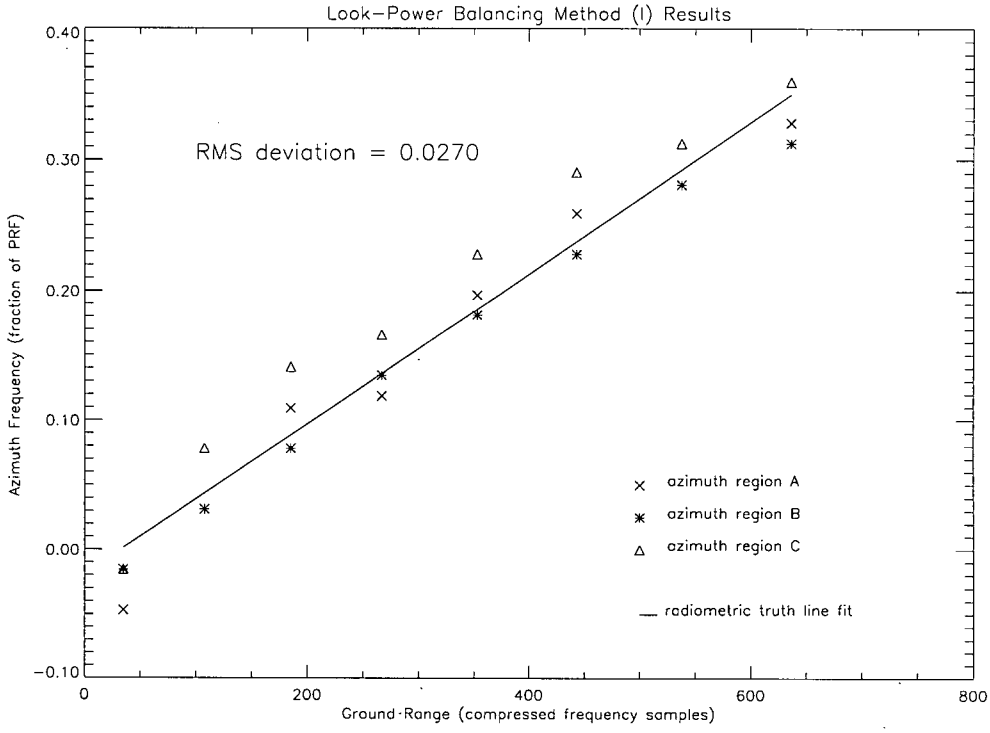

Figure F.6 Look-Power Balancing (II) Method Results

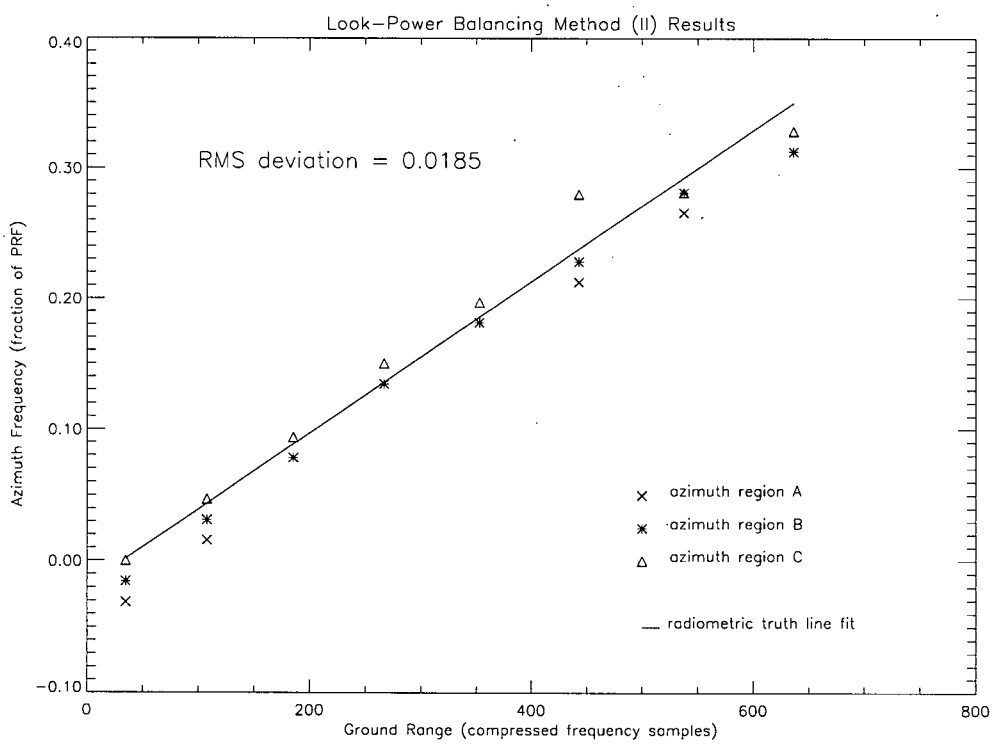

Appendix G: RMS Deviation of Doppler Centroid Estimates over Range: Squamish Scene

This appendix presents the RMS Deviation testing results for the Squamish Scene, for each Doppler centroid estimation method. These results are described in Section 4.2 of Chapter 4.

Figure G.1 Correlation with Optimal Estimator Method Results

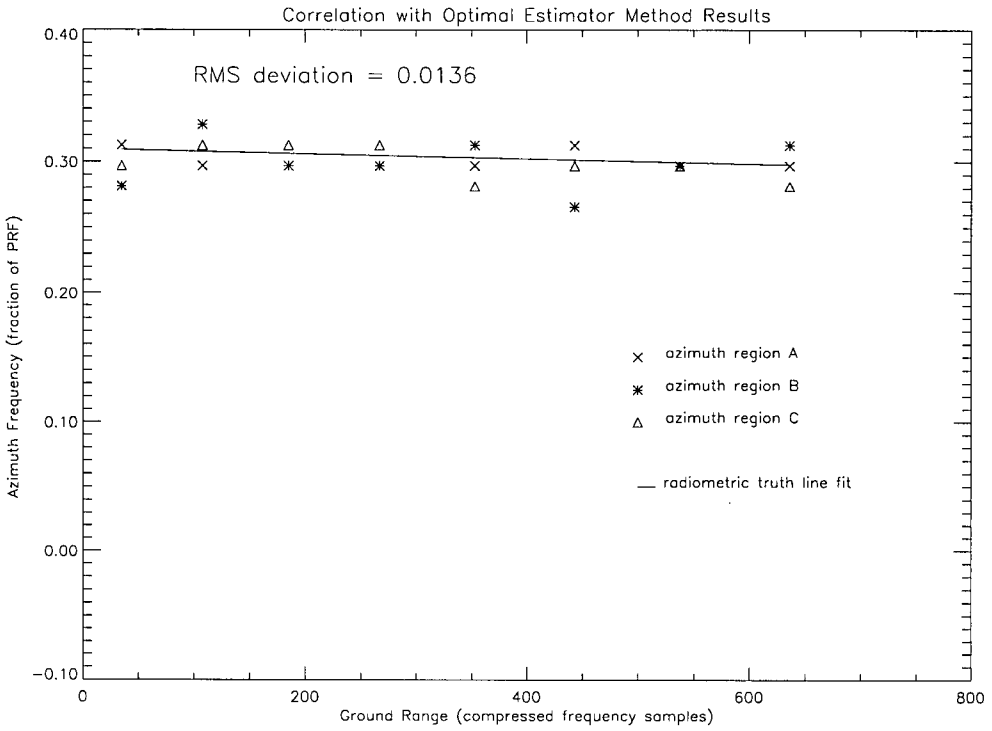

Figure G.2 Sign Doppler Estimator Method Results

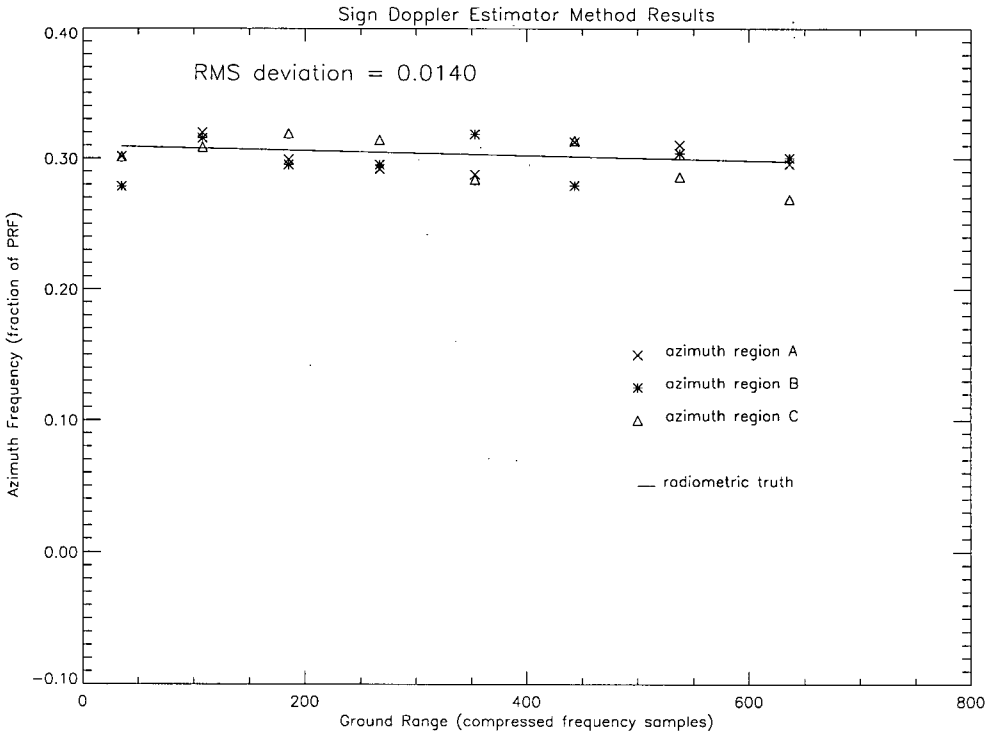

Figure G.3 Look-Power Balancing (II) Method Results

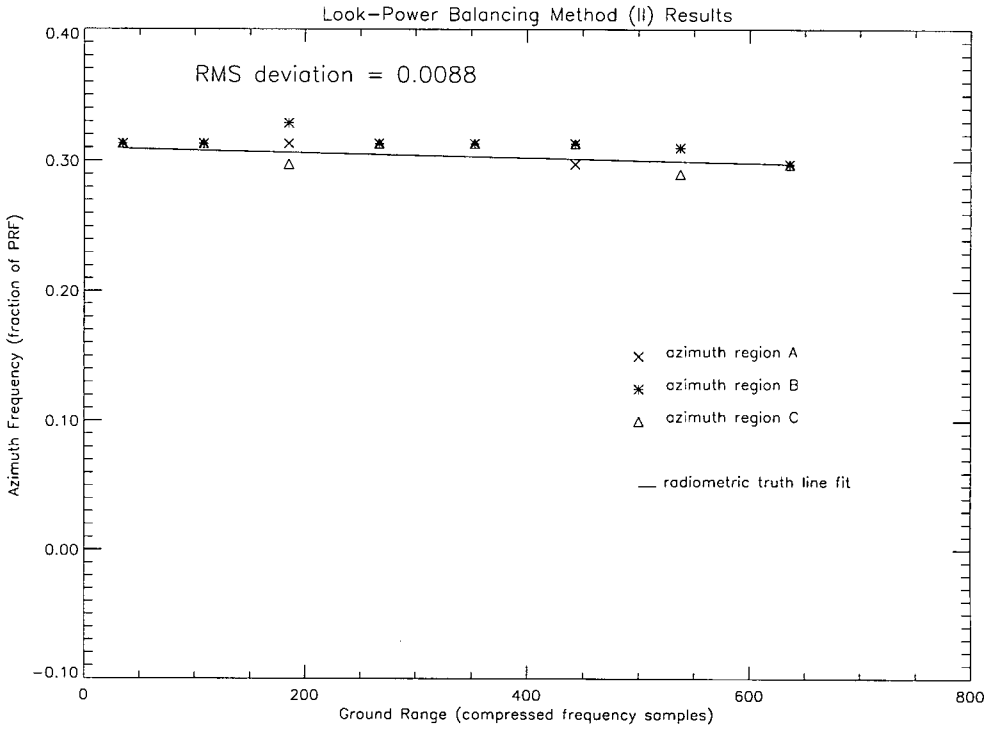

Appendix H: Azimuth Radiometric Scalloping Measurement Results: Netherlands Scene

This appendix contains the results of applying methods COE, SDE and LPBII to process the Netherlands Scene data image. For each estimation method, the quantification of the residual scalloping resulting from applying the Inverse Beam Pattern Method (for 1 and 2 looks) and the Constant SNR Method (for 2 looks) for antenna pattern correction are illustrated.

Figure H.1 Magnitude of Averaged Output Azimuth Spectra (8 adjacent subswaths shown). *antenna pattern correction method: Inverse Beam Pattern, 1 look (plain Line); Inverse Beam Pattern, 2 look (dotted line); Constant SNR Method, 2 look (dashed line).*

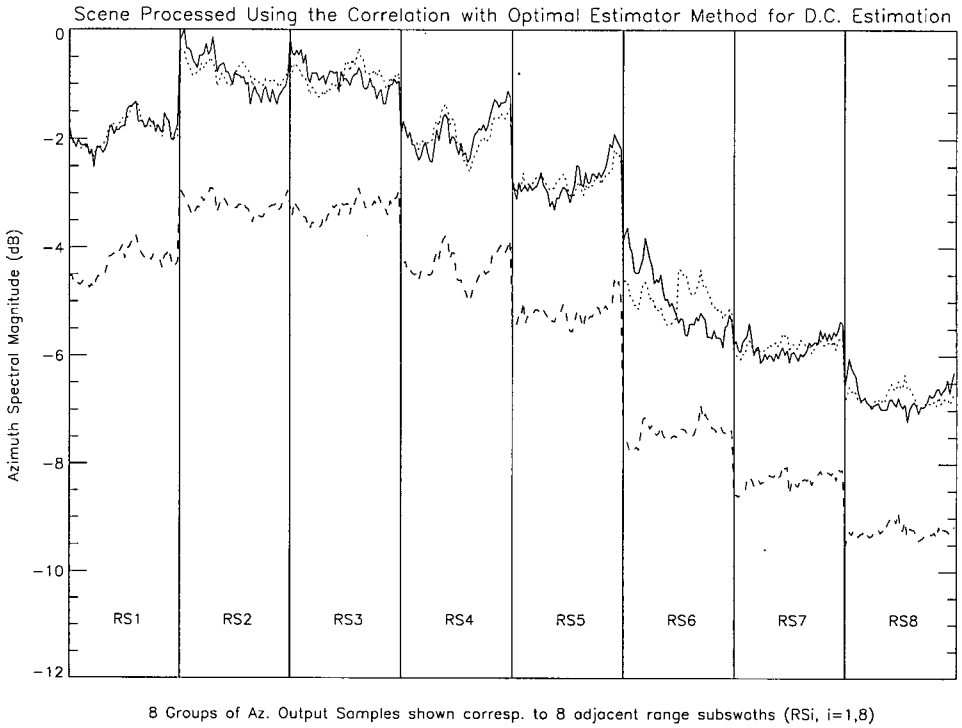

Figure H.2 Averaged Azimuth Spectral Scalloping Measure per Subswath (8 adjacent subswaths shown). *antenna pattern correction method: Inverse Beam Pattern, 1 look ('x'); Inverse Beam Pattern, 2 look (triangle); Constant SNR Method, 2 look ('*').*

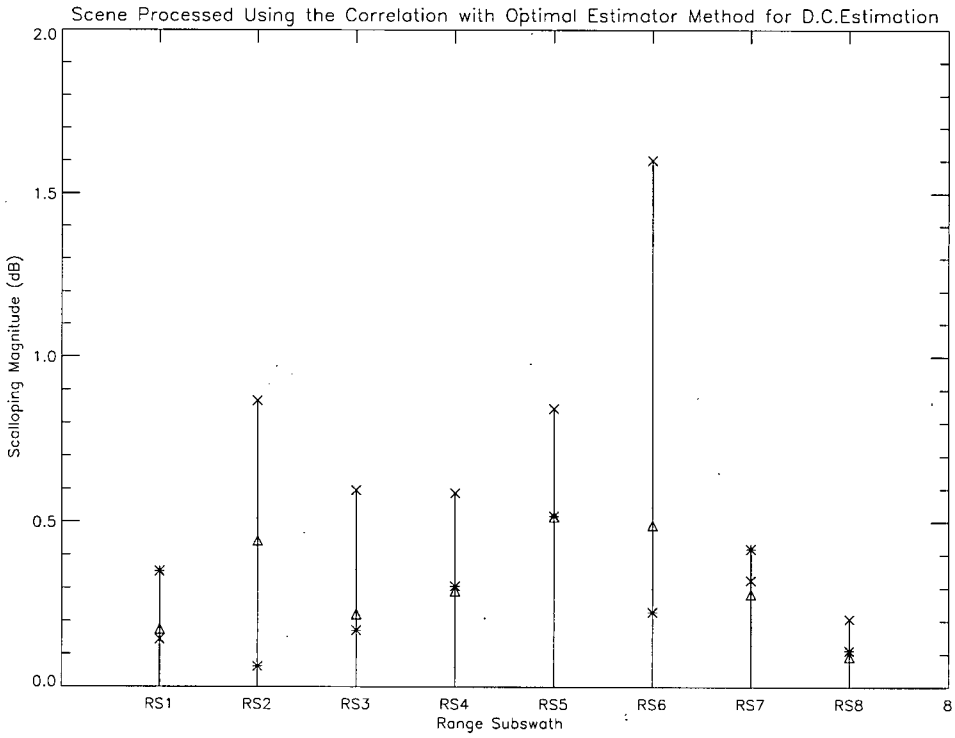

Figure H.3 Magnitude of Averaged Output Azimuth Spectra (8 adjacent subswaths shown). *antenna pattern correction method: Inverse Beam Pattern, 1 look (plain Line); Inverse Beam Pattern, 2 look (dotted line); Constant SNR Method, 2 look (dashed line).*

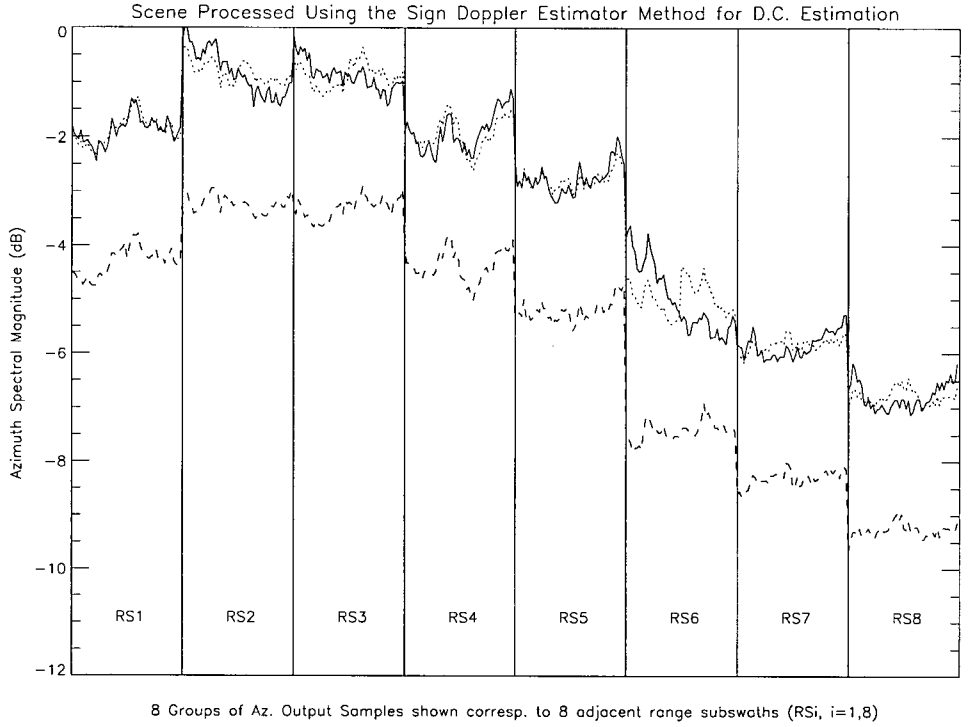

Figure H.4 Averaged Azimuth Spectral Scalloping Measure per Subswath (8 adjacent subswaths shown). *antenna pattern correction method: Inverse Beam Pattern, 1 look ('x'); Inverse Beam Pattern, 2 look (triangle); Constant SNR Method, 2 look ('*').*

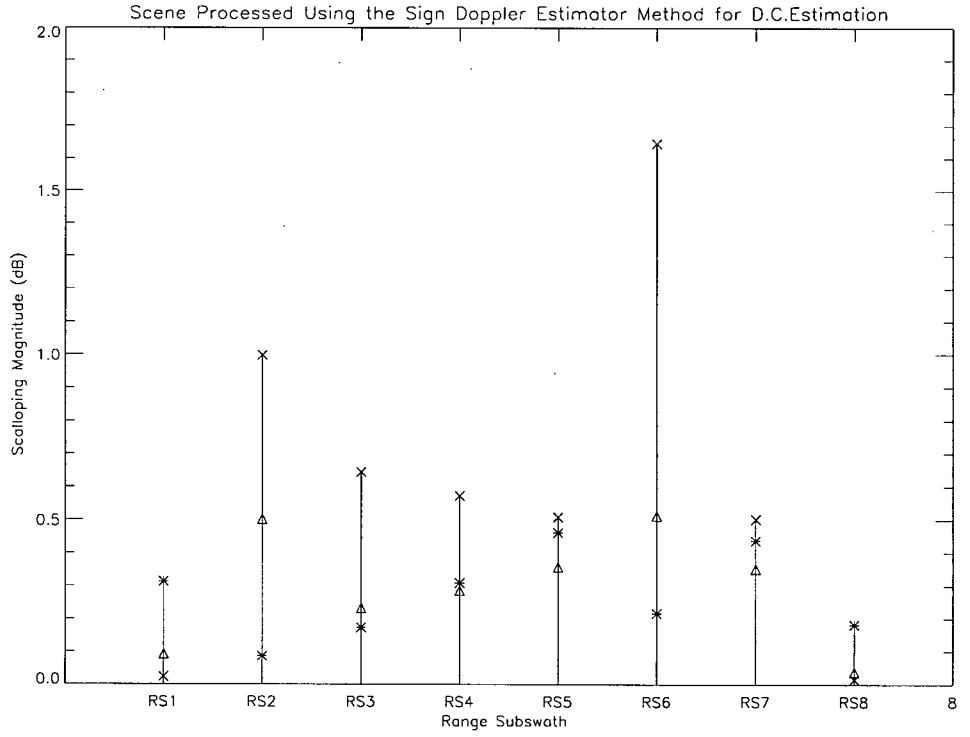

Figure H.5 Magnitude of Averaged Output Azimuth Spectra (8 adjacent subswaths shown). *antenna pattern correction method: Inverse Beam Pattern, 1 look (plain Line); Inverse Beam Pattern, 2 look (dotted line); Constant SNR Method, 2 look (dashed line).*

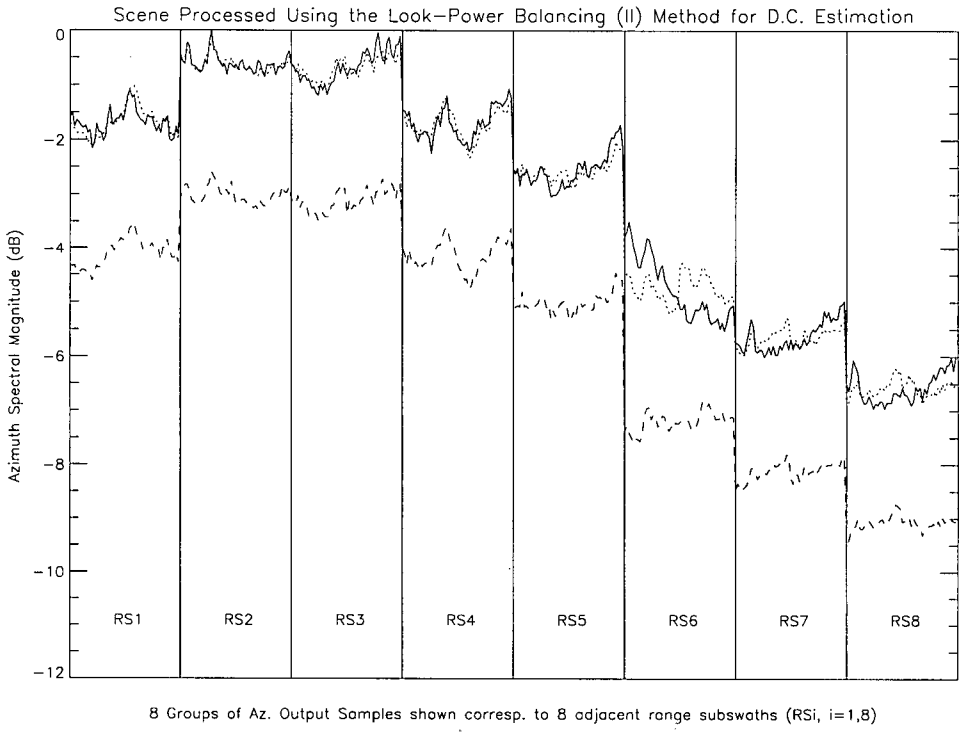

Figure H.6 Averaged Azimuth Spectral Scalloping Measure per Subswath (8 adjacent subswaths shown). *antenna pattern correction method: Inverse Beam Pattern, 1 look ('x'); Inverse Beam Pattern, 2 look (triangle); Constant SNR Method, 2 look ('*').*

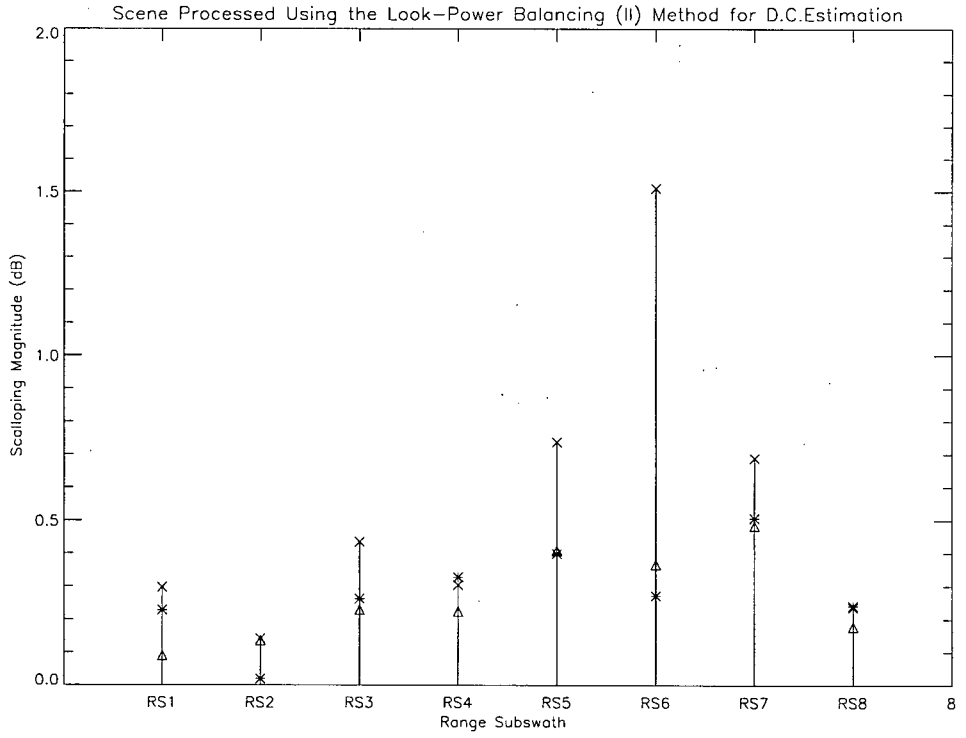

Appendix I: Azimuth Radiometric Scalloping Measurement Results: Squamish Scene

This appendix contains the results of applying methods COE, SDE and LPBII to process the Squamish Scene data image. For each estimation method, the quantification of the residual scalloping resulting from applying the Inverse Beam Pattern Method (for 1 and 2 looks) and the Constant SNR Method (for 2 looks) for antenna pattern correction are illustrated.

Figure I.1 Magnitude of Averaged Output Azimuth Spectra (8 adjacent subswaths shown). *antenna pattern correction method: Inverse Beam Pattern, 1 look (plain Line); Inverse Beam Pattern, 2 look (dotted line); Constant SNR Method, 2 look (dashed line).*

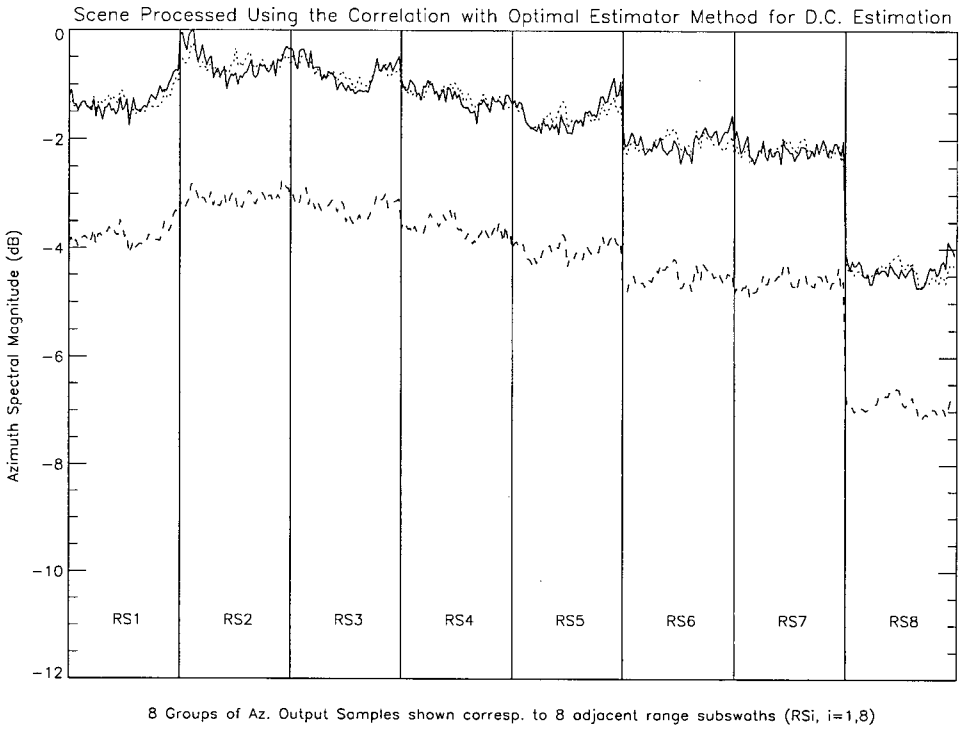

Figure I.2 Averaged Azimuth Spectral Scalloping Measure per Subswath (8 adjacent subswaths shown). *antenna pattern correction method: Inverse Beam Pattern, 1 look ('x'); Inverse Beam Pattern, 2 look (triangle); Constant SNR Method, 2 look ('*').*

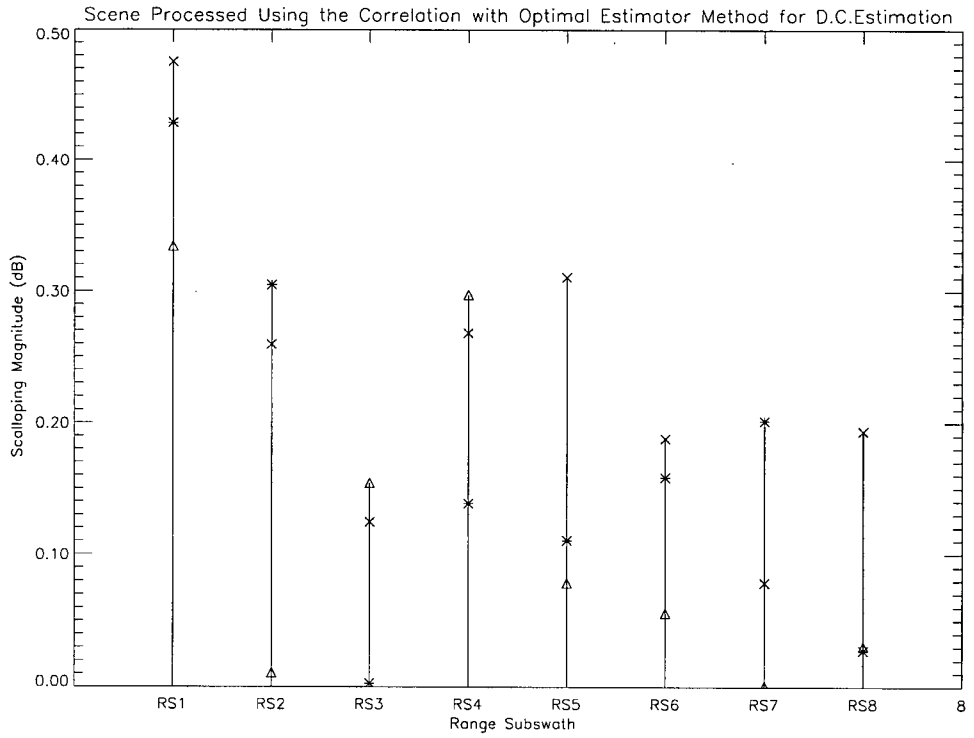

Figure I.3 Magnitude of Averaged Output Azimuth Spectra (8 adjacent subswaths shown). *antenna pattern correction method: Inverse Beam Pattern, 1 look (plain Line); Inverse Beam Pattern, 2 look (dotted line); Constant SNR Method, 2 look (dashed line).*

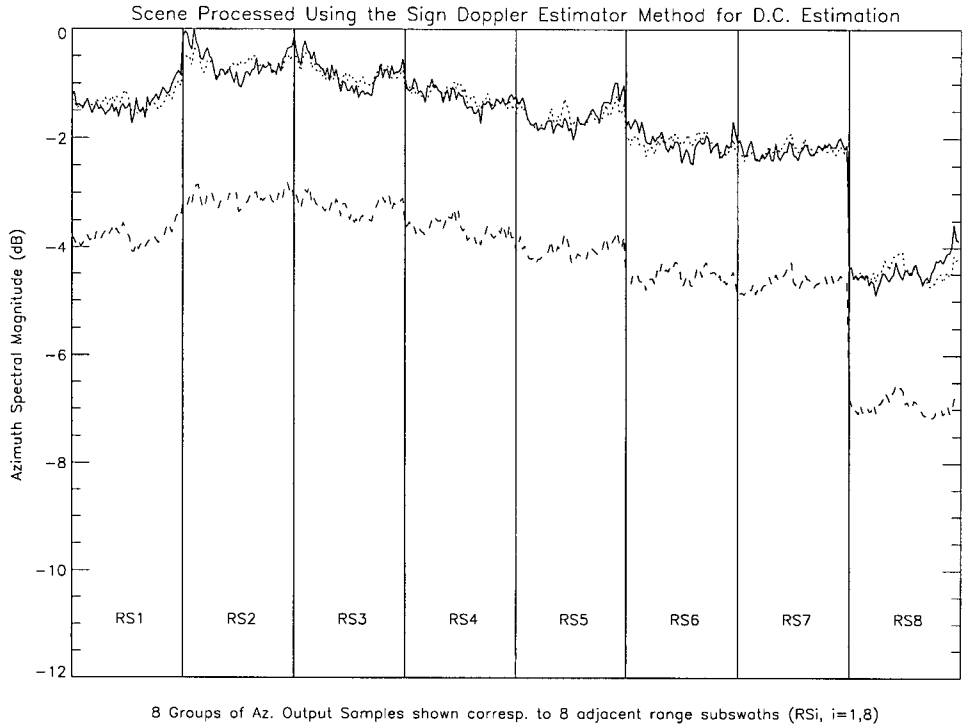

Figure I.4 Averaged Azimuth Spectral Scalloping Measure per Subswath (8 adjacent subswaths shown). *antenna pattern correction method: Inverse Beam Pattern, 1 look ('x'); Inverse Beam Pattern, 2 look (triangle); Constant SNR Method, 2 look ('*').*

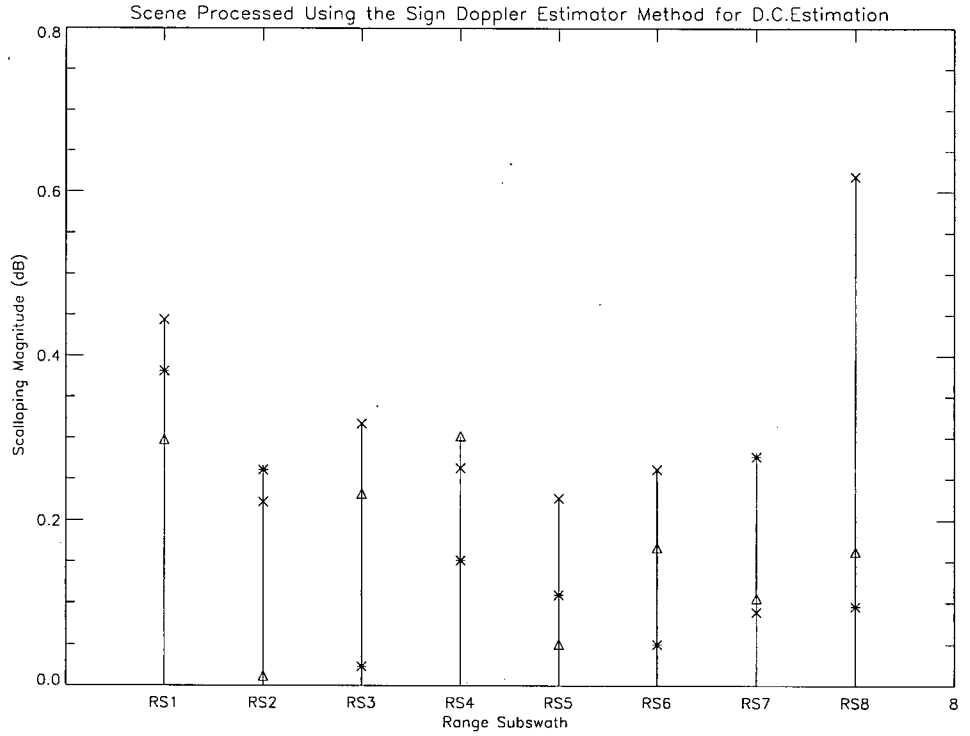

Figure I.5 Magnitude of Averaged Output Azimuth Spectra (8 adjacent subswaths shown). *antenna pattern correction method: Inverse Beam Pattern, 1 look (plain Line); Inverse Beam Pattern, 2 look (dotted line); Constant SNR Method, 2 look (dashed line).*

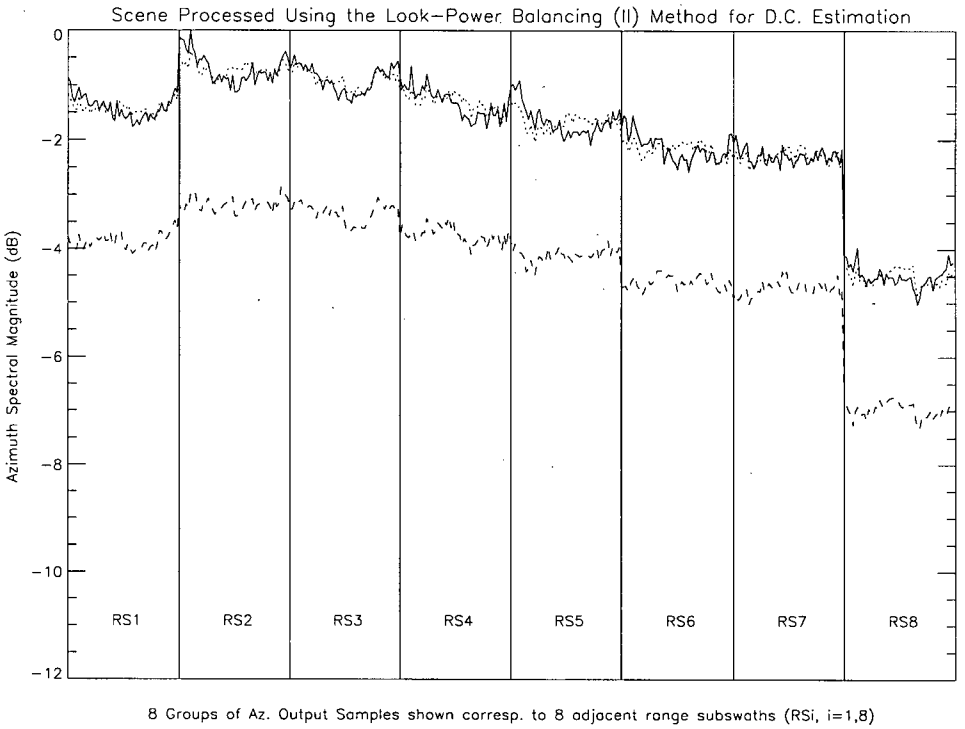

Figure I.6 Averaged Azimuth Spectral Scalloping Measure per Subswath (8 adjacent subswaths shown). *antenna pattern correction method: Inverse Beam Pattern, 1 look ('x'); Inverse Beam Pattern, 2 look (triangle); Constant SNR Method, 2 look ('*').*

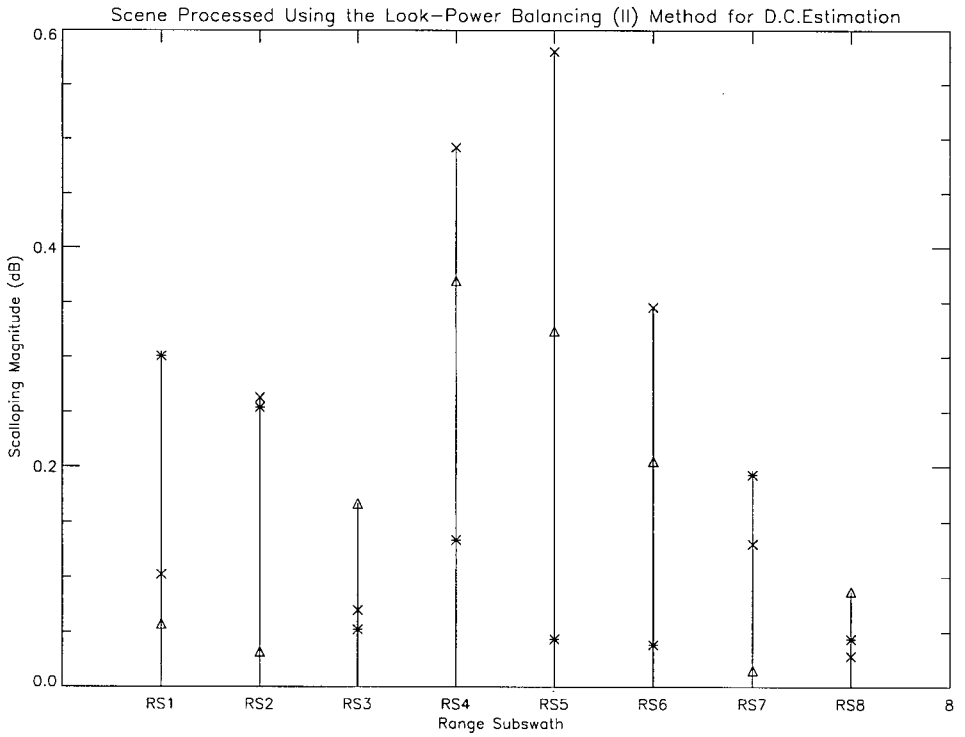

Appendix J: ERS-1 Processed Image Results

This appendix presents images processed using selected Doppler centroid estimation methods and antenna pattern correction methods for both the Netherlands Scene data and the Squamish Scene data.

Figure J.1 Netherlands Scene Processed using the Correlation with Optimal Estimator Method for Doppler Centroid Estimation (antenna pattern correction method: Constant SNR Method, 2 Look). Overall Scalloping Measure: **0.27**.

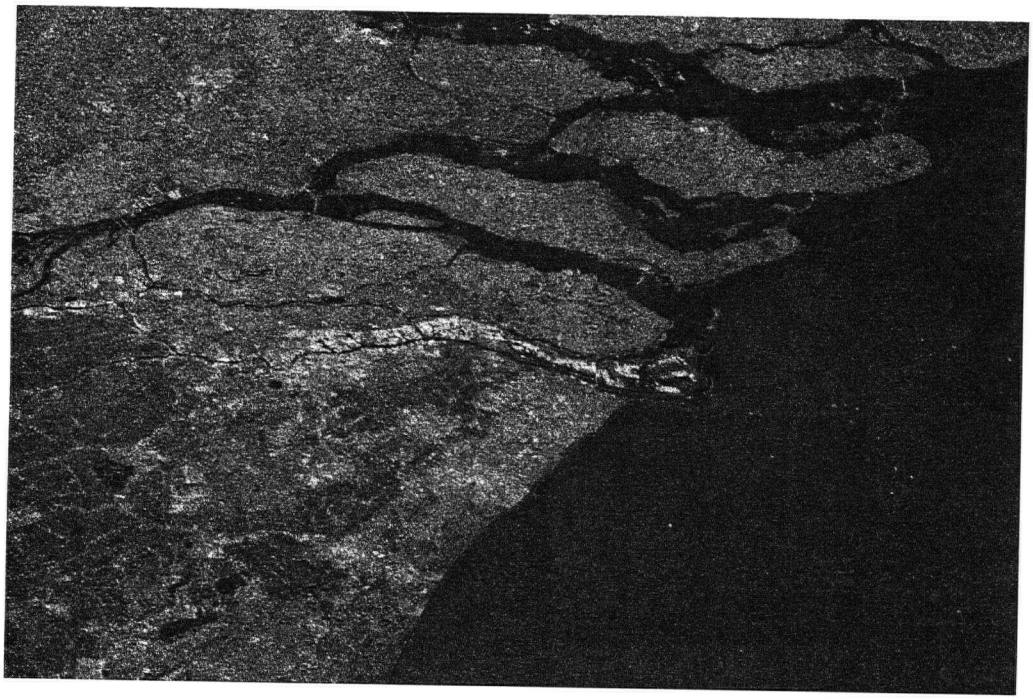

Figure J.2 Netherlands Scene Processed using the Correlation with Optimal Estimator Method for Doppler Centroid Estimation (antenna pattern correction method: Inverse Beam Pattern, 1 Look). Overall Scalloping Measure: **0.65 dB**.

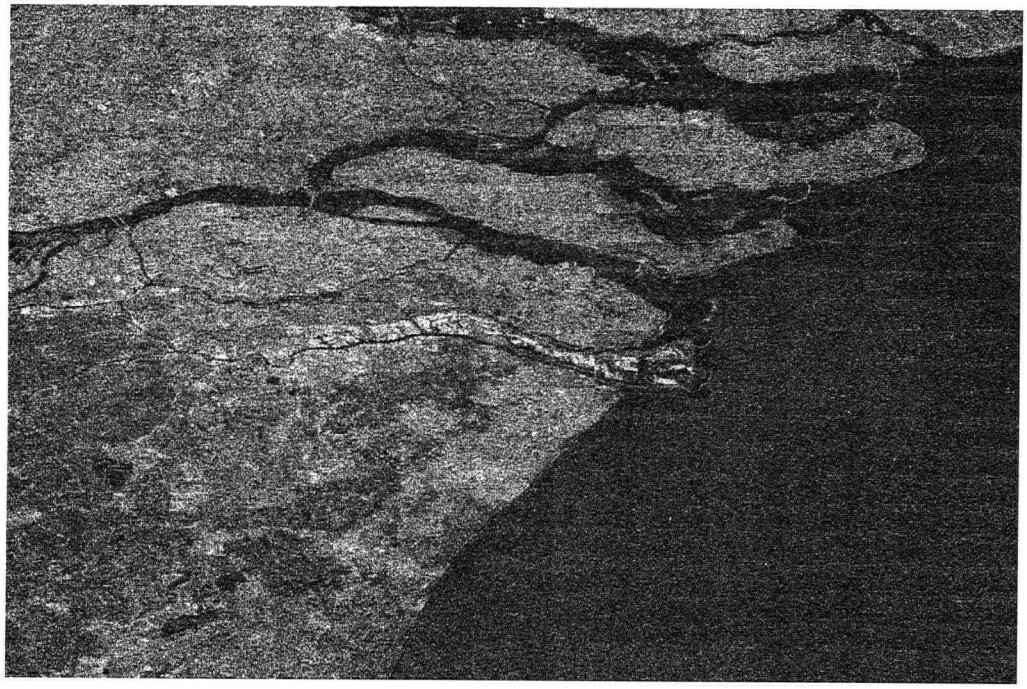

Figure J.3 Squamish Scene Processed using the Correlation with Optimal Estimator Method for Doppler Centroid Estimation (antenna pattern correction method: Inverse Beam Pattern, 2 Look). Overall Scalloping Measure: **0.12 dB**.

Figure J.4 Squamish Scene Processed using the Sign Doppler Estimator Method for Doppler Centroid Estimation (antenna pattern correction method: Inverse Beam Pattern, 1 Look). Overall Scalloping Measure: **0.31 dB**.